



*Dipl.-Ing. Florian Preishuber-Pflügl*

Access to Nanocrystalline F-Ion Conductors  
by Mechanochemistry:  
Insights into Synthesis Conditions and Diffusion Parameters

DISSERTATION

zur Erlangung des akademischen Grades

*Doktor der technischen Wissenschaften (Dr. techn.)*

eingereicht an der

Technischen Universität Graz

Betreuer

*Univ.-Prof. Dr. Martin Wilkening*

Institut für Chemische Technologie von Materialien

Graz, Februar 2016



### **Affidavit**

I declare that I have authored this thesis independently, that I have not used other than the declared sources/resources, and that I have explicitly indicated all material which has been quoted either literally or by content from the sources used. The text document uploaded to TUGRAZonline is identical to the present doctoral dissertation.

### **Eidesstaatliche Erklärung**

Ich erkläre an Eides statt, dass ich die vorliegende Arbeit selbstständig verfasst, andere als die angegebenen Quellen/Hilfsmittel nicht benutzt, und die den benutzten Quellen wörtlich und inhaltlich entnommenen Stellen als solche kenntlich gemacht habe. Das in TUGRAZonline hochgeladene Textdokument ist mit der vorliegenden Dissertation identisch.

16.02.2016

Date / Datum

Florian Freiskuber - Pflügl

Signature / Unterschrift



*to Nicole*



## Abstract

Solid-state ion conductors represent an important class of materials in the field of fundamental and applied research that are still facing a high and a growing interest. Besides sensor applications, there is an increasing demand for solids with a high ionic conductivity as those materials are required for electrochemical energy storage systems. Especially in batteries, a high diffusivity within the processed materials is required to guarantee good conductivity characteristics that enable high charging and discharging rates. Those parameters are especially necessary to fulfill the demand of modern electric devices, *e.g.*, electric cars, which demand a high performance of the electrochemical storage systems. In addition, safety issues demand for novel systems based on solid electrolytes to get rid of the inflammable components of current battery technologies.

A crucial parameter for a proper ion conductivity of solid-state systems is of course their chemical composition. However, the morphology is of great importance too and has attracted researchers to tailor the structural features of a material in order to boost its intrinsic properties and increase the overall diffusivity. An important approach to influence the morphology of solid ion conductors is a mechanical and/or mechanochemical treatment by high energy ball milling. This technique allows a structural modification of known ion conductors as well as it opens new possibilities for the synthesis of materials with yet inaccessible properties. Such solid solutions or metastable phases of two or more compounds with poor conductivity can show drastically improved properties upon the treatment in planetary ball mills.

Within this work, fluorine ion conductors were synthesized by mechanochemical pathways to prepare yet unknown materials such as Rb-doped, tetragonal  $\text{BaSnF}_4$  which shows a high ion conductivity at room temperature that was yet only known for the structurally closely related  $\text{PbSnF}_4$ . In addition, solid solutions of  $\text{Ba}_{0.6}\text{La}_{0.4}\text{F}_{2.4}$  were synthesized and thoroughly investigated by solid state NMR and impedance spectroscopy regarding its diffusion parameters. The synthesis method itself was in the focus of investigations as well, as the yet unpublished mechanochemical synthesis of  $\text{BaMgF}_4$  was studied in detail by  $^{19}\text{F}$  MAS NMR in combination with X-ray spectroscopy.

The results of the investigation were published in peer-reviewed journals and are further discussed in this thesis. In addition, a brief overview and comprehensive insights into the theory of the employed methods is given in the first chapters of this work.



## Kurzfassung

Festkörper-Ionenleiter stellen eine wichtige Klasse von Materialien dar, die sowohl im Bereich der Grundlagenforschung, als auch der angewandten Forschung mit großem und nach wie vor steigendem Interesse konfrontiert sind. Neben Anwendungen in Sensoren besteht eine dringende Nachfrage für Festkörper mit hoher Ionenleitfähigkeit für deren Einsatz in elektrochemischen Energiespeichern. Besonders für Batterien werden Materialien benötigt, die eine hohe Diffusivität aufweisen, um eine gute Leitfähigkeit zu garantieren, welche ein schnelles Laden und Entladen ermöglicht. Letzteres ist vor allem im Anwendungsbereich von modernen elektronischen Geräten wie beispielsweise Elektroautos vonnöten, da diese eine hohe Leistungsfähigkeit der elektrochemischen Energiespeicher erfordern. Zu diesen Anforderungen hinzu kommt das Verlangen nach sicheren Festkörperenergiespeichern, da in aktuellen, wiederaufladbaren Batteriesystemen brennbare Zusätze in den Flüssigelektrolyten zum Einsatz kommen.

Ein wichtiger Parameter für eine hohe Leitfähigkeit eines Festkörpers ist die chemische Zusammensetzung. Zusätzlich kommt jedoch auch der Morphologie der Materialien eine große Bedeutung zu, was in den letzten Jahren sehr stark das Interesse der Forschung geweckt hat. Das Ziel ist die strukturellen Charakteristiken eines Systems maßzuschneidern, um dessen intrinsischen Leitfähigkeitseigenschaften zu verbessern. Hierbei spielen mechanische Beeinflussungen oder auch sogenannte mechanochemische Synthesen eine bedeutende Rolle. Diese Techniken ermöglichen eine strukturelle Modifikation bekannter Stoffe beziehungsweise eröffnen diese völlig neue Synthesewege für die Herstellung von Materialien mit bisher unzugänglichen Eigenschaften. Solche Mischkristalle, sowie auch neue, metastabile Phasen aus zwei oder mehreren Ausgangsmaterialien, zeigen häufig stark verbesserte Eigenschaften, wenn diese mechanochemisch hergestellt werden.

Im Rahmen dieser Arbeit wurden Fluor-Ionenleiter mittels Mechanochemie präpariert. Dabei konnten bisher unerforschte Ionenleiter wie beispielsweise Rubidium-dotiertes, tetragonales  $\text{BaSnF}_4$  hergestellt werden. Dieses zeigt eine sehr hohe Leitfähigkeit bei Raumtemperatur, welche bisher nur vom strukturell verwandten  $\text{PbSnF}_4$  erreicht wurde. Weiters wurde die Mischkristallverbindung  $\text{Ba}_{0,6}\text{La}_{0,4}\text{F}_{2,4}$  hergestellt und umfassend mittels Festkörper-NMR sowie Impedanzspektroskopie hinsichtlich dessen Diffusionseigenschaften untersucht. Die Mechanochemie als Herstellungsmethode selbst wurde anhand der Modellsubstanz  $\text{BaMgF}_4$  studiert, wobei  $^{19}\text{F}$  MAS NMR Spektroskopie sowie Röntgendiffraktometrie zum Einsatz kamen.

Die Ergebnisse wurden in durch Gutachter beurteilten Fachjournalen publiziert. Diese Veröffentlichungen und die Diskussion von zusätzlichen Ergebnissen werden in dieser Dissertation diskutiert. Ein Einstieg in die Thematik sowie Erklärungen zur Theorie von Festkörper-Ionenleitern und deren Charakterisierungsmethoden finden sich in den ersten Kapiteln dieser Arbeit.



## Content

<b>1. Introduction</b> .....	<b>1</b>
<b>2. Theory of diffusion and solid-state ionics</b> .....	<b>5</b>
2.1 Principles of diffusion.....	5
2.2 Diffusion in solids.....	7
2.2.1 Defects in crystal structures.....	8
2.2.2 Mechanisms of diffusion.....	11
<b>3. Measurement of diffusion parameters</b> .....	<b>13</b>
3.1 Impedance spectroscopy.....	14
3.1.1 The concept of complex impedance.....	14
3.1.2 Permittivity, conductivity and modulus.....	17
3.1.3 Data representations.....	19
3.2 Nuclear magnetic resonance spectroscopy.....	22
3.2.1 The vector model.....	22
3.2.2 Relaxation rates.....	25
3.2.3 Interpretation of the relaxation data, BPP model.....	27
3.2.4 Structural characterization – MAS NMR.....	30
<b>4. Mechanochemistry and nanomaterials</b> .....	<b>31</b>
4.1 Mechanochemical synthesis.....	31
4.2 Nanocrystalline materials.....	33
<b>5. Results and discussion</b> .....	<b>35</b>
5.1 Layer-structured BaSnF <sub>4</sub> .....	37
5.2 F-ion conducting solid solution Ba <sub>0.6</sub> La <sub>0.4</sub> F <sub>2.4</sub> .....	53
5.3 Mechanochemical synthesis of BaMgF <sub>4</sub> .....	69
5.4 A review on mechanochemically synthesized F-ion conductors.....	81
<b>6. Conclusion and Outlook</b> .....	<b>99</b>
<b>A. Experimental</b> .....	<b>101</b>
<b>B. Bibliography</b> .....	<b>105</b>
<b>C. Publications</b> .....	<b>111</b>
C. 1. Publications in peer reviewed journals.....	111
C. 2. Oral Presentations.....	112
C. 3. Posters.....	112
<b>D. Acknowledgment</b> .....	<b>113</b>



## 1. Introduction

The migration of charge carriers in solid materials is a phenomenon that is understood and well-known. It is common knowledge that *electrons* start to flow in a metal wire, as soon as the light is turned on or the electric cooker is started for making coffee in the morning. But, there is probably less common knowledge about the migration of *ions* in solid materials.

The phenomenon of ion conduction in solids was discovered by Michael Faraday in the 19<sup>th</sup> century and was described by A. Chadwick as follows:<sup>1</sup>

---

*“As in many areas of physical science the start of the research field can be traced back to Michael Faraday. His diary revealed that he measured the electrical conductivity of a range of materials during the early 1830’s.<sup>2,3</sup> The experiments he performed on ionic solids were remarkable in terms of laying the foundations for a new range of materials and a research field, namely fast-ion conductors (often referred to as superionics or solid electrolytes) and providing an insight into his scientific genius. On 21<sup>st</sup> February 1833 Faraday noted the “very extraordinary behaviour” of  $\text{Ag}_2\text{S}$ , which conducted electricity in the solid state and showed electrolytic decomposition. Almost exactly two years later, on 19<sup>th</sup> February 1835 he found that solid  $\text{PbF}_2$  at “dull red heat” also conducted electricity.”*

---

In the following years, solid state ionics was established as a separate field of research and the investigations on these materials increased. Today, solid ion conductors are present everywhere in our daily life as they represent the main constituents of the active materials in batteries. (Rechargeable) batteries are found in many devices we use every day. It starts with a battery powered alarm clock, continues with the electrical toothbrush and when we use our smartphone for a first peek on the news in the morning. Notebooks for our daily work routine are powered by batteries, as well as – hopefully soon – our electric vehicle. And, there are high expectations in rechargeable batteries on large scale for the storage of renewable energy from sun, wind or hydro power plants.

A battery is basically built of a negative and a positive electrode separated by an electrolyte that shuttles the charge carriers between these electrodes. The transport of ions in solids occurs in these electrodes or active materials, where the electrochemical reaction takes place. The current that is delivered from a battery originates from the chemical reactions in these active materials. The electrolyte between the electrodes in latest battery systems which use lithium as a charge carrier is a lithium salt dissolved in an organic liquid. Such solutions possess a high ionic conductivity compared to most solid state ion conductors. However, modern preparation methods and improved knowledge about structural parameters allow to tailor materials to improve their conductivity. The replacement of liquid electrolytes would further benefit from improved safety, as organic liquids

are inflammable and solid compounds are thought to improve cycling stability, thus the lifetime of a battery.

Today, lithium ion chemistry based systems are the most advanced secondary batteries. They can be charged and discharged more than 1000 cycles without a big loss of their specific capacity. However, the increasing requirements due to the technological progress ask for further improvements such as higher capacities or higher cell voltage for portable devices, or, as mentioned above, large scale battery packs for storage of energy from renewable resources. Besides the increasing demands, many of the components that are required for manufacturing Li-ion batteries are scarce and thus expensive. This fact prompted researchers to explore other elements based on different chemistries than Li. Sodium and magnesium, which are located right below lithium in the periodic table possess similar properties and came into the focus of interest. Both elements are abundant and rather cheap.

In contrast to these systems that make use of cations as charge carriers, batteries based on fluorine chemistry have also been demonstrated. Fluorine is the lightest atom of the halogens and forms a small, negative charged fluoride ( $F^-$ ) anion. The small size facilitates the diffusion in solids. Fluorine is at the bottom of the electrochemical series and shows a high oxidation potential versus the standard hydrogen reference electrode. This promises high cell voltages and high capacities if metals are used as conversion electrodes.<sup>4</sup> First galvanic cells based on fluoride chemistry were demonstrated at the same time in 1976 by Kennedy/Hunter<sup>5</sup> and Schoonman.<sup>6</sup> Electrochemical cells were mainly built on basis of lead/lead fluoride chemistry of the type  $Pb | \beta\text{-PbF}_2:\text{AgF} | \text{BiO}_x\text{F}_{3-2x} | \text{Bi}$  (Schoonman) operating at temperatures ranging from 295 K to 375 K. The elevated operating temperatures were necessary to ensure a good conductivity of the solid materials. Kennedy and Hunter tried to build rechargeable cells of  $Pb | \text{PbF}_2 | \text{PbF}_2, \text{CuF}_2 | \text{Cu}$  which were tested at 298 and 348 K, respectively. However, the discharging of the cells turned out to be irreversible with the available techniques at that time. The idea of a F-ion battery was picked up again by the work group of Fichtner in 2011, where they have demonstrated a first study of a rechargeable cell.<sup>4</sup> The lack of good solid ion conductors at low temperatures or suitable liquid  $F^-$  electrolytes still represented a big drawback and prevents applications of F-ion batteries at room temperature. This issue was addressed in the last years and fast solid fluoride conductors were investigated and new compositions were explored.<sup>7-9</sup>

Next to the chemical composition, structural features and grain size play a big role in terms of ion conductivity. Many materials show an increased conductivity when the grain size is decreased down to the nanoscale, as this yields an increased surface or interfacial area. Such nanocrystalline materials often show a higher concentration of structural defects which can be beneficial for the conductivity. Defects or vacancies in a crystal structure are necessary for ion conduction, as ions hop from occupied to empty sites to migrate

---

in a material. A modern approach for the preparation of inorganic ion conducting materials is mechanochemistry. With this method, the chemical reaction of the precursors is triggered by mechanical action like, *e.g.*, the treatment of powders in a planetary ball mill. Mechanochemical preparations combine a direct synthesis of nanocrystalline powders and influence the structural parameters such as the defect concentration, the morphology of the crystallites and the grain size of the powder.

The characterization of ionic conductors involves the investigation of structural parameters as well as the diffusion parameters such as the conductivity. The structure of crystalline materials can be analyzed by diffraction methods like X-ray or neutron diffraction that provide information about the orientation of crystallographic planes in the material or distances between the individual atoms. These parameters are important to determine possible preferred conduction pathways in the material such as channels or layers. Diffusion parameters are investigated by spectroscopic methods. Broadband impedance spectroscopy is used to determine the conductivity of the material by the application of a frequency dependent electric field across a sample pellet. It further allows to distinguish different transport processes like bulk vs grain boundary processes. In addition, the average hopping energies for the individual processes can be determined from the conductivity plots and it can give indications about the dimensionality of the conduction process. This information can be correlated with structural data from the diffraction methods. As a complementary technique, nuclear magnetic resonance spectroscopy (NMR) can be used. Temperature dependent solid state NMR measurements give information about short- and long-range ion dynamics, as well as activation energies for the hopping processes. The advantage of NMR methods in contrast to impedance spectroscopy is the selective measurement of the diffusion parameters of distinct nuclei such as  $^{19}\text{F}$  in the present case.

The aim of this thesis was the preparation and modification of fast solid state F-ion conductors by mechanochemistry and a detailed characterization of the obtained materials. Solid solutions of  $\text{BaF}_2$  and  $\text{LaF}_3$  were prepared which have shown an increased conductivity compared to the pure precursors.  $\text{BaMgF}_4$  was studied as a model compound to study low dimensional transport parameters, but also to shed light on the mechanochemical synthesis of F-ion conductors.  $^{19}\text{F}$  MAS NMR was used in combination with X-ray spectroscopy to investigate the transformations of the materials during the milling process. A similar approach was chosen for  $\text{BaSnF}_4$ , which is the fastest solid F-ion conductor among the studied systems. The layered, tetragonal form reached a conductivity of about 1 mS/cm at room temperature. This positions the material among the fastest solid fluoride conductors known today.<sup>10</sup> The diffusivity of the material could even be slightly improved by substitution of  $\text{Ba}^{2+}$  with monovalent  $\text{Rb}^+$  ions.



## 2. Theory of diffusion and solid-state ionics

### 2.1 Principles of diffusion

Diffusion is deviated from the latin word *diffundere*, which means to spread or to disperse. Diffusion can be observed in gases, in liquids and in solids. It describes the phenomenon of the migration of particles which is induced by a concentration gradient. The driving force is the entropy, as it increases with the dispersion of the particles.<sup>11</sup> A very comprehensible demonstration to understand diffusion is when a drop of colored liquid is added to a beaker with the same, colorless solvent, as it is shown in Figure 1.<sup>a</sup> The drop immerses into the solvent and starts to spread, which is initially induced by the turbulences that results from the dripping. When the drop finally stops to move, the color molecules will proceed to spread in the surrounding colorless liquid, as it is seen in the second and the third beaker of Figure 1. The driving force of this process is the high concentration of the colorant in the initial drop that will equalize in the entire available volume. This final state, when the molecules have equally spread across the entire solvent, is seen in the last beaker.

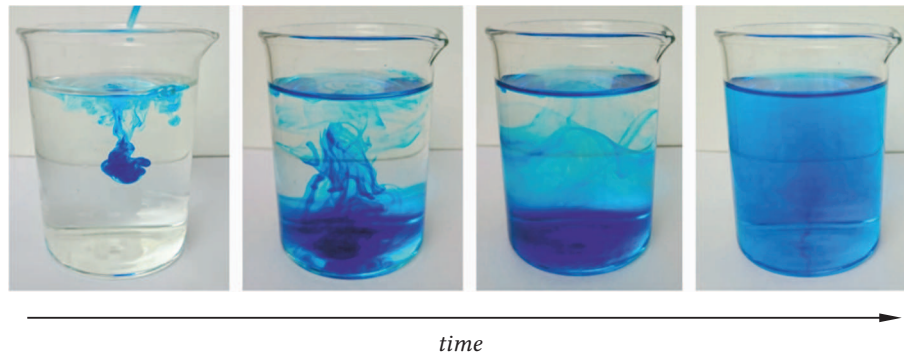


**Figure 1** – Diffusion of color molecules in a liquid as a function of time.<sup>a</sup>

The relationship between the flux of such color molecules or generally particles and the concentration in is given by Fick's laws.<sup>12</sup> *Fick's first law* describes the flux of particles in one dimension in isotropic media:

$$j_x = -D_i \frac{\partial c}{\partial x} \quad (0.1)$$

The quantity  $j_x$  is the flux of particles and  $c$  their number density or concentration;  $D_i$  defines the *diffusion coefficient* or *diffusivity* and has the dimension  $[\text{m}^2 \text{s}^{-1}]$ . The minus sign denotes the opposite direction of the flux of particles to the concentration gradient.

---

<sup>a</sup> Images provided by Nicole Pabi.

As the experiment in the beaker above describes the spreading of molecules in a solvent in all directions, we can generalize the above equation using a vector notation:

$$j = -D_i \nabla c \quad (0.2)$$

Here,  $j$  is the vector of diffusion flux in the  $x, y, z$ -coordinates and  $\nabla C$  the concentration gradient vector. If the diffusion is anisotropic,  $D_i$  is a tensor and expressed as  $D^{tr}$ , the *macroscopic diffusion coefficient* or *tracer diffusion coefficient*. The nabla symbol  $\nabla$  represents the vector differential operator  $\nabla = (\partial/\partial x, \partial/\partial y, \partial/\partial z)$  in all three coordinates. As a flux of particles or atoms is impossible to measure until steady state is reached,<sup>13</sup> Fick's first law is usually combined with the equation of continuity  $\partial c/\partial t + \nabla j = 0$  to give *Fick's second law*, which is also known as the *diffusion equation*:

$$\frac{\partial c}{\partial t} = \nabla \cdot (D^{tr} \nabla c) \quad (0.3)$$

If the diffusion is independent of concentration, eq. (0.3) can be written as:

$$\frac{\partial c}{\partial t} = D^{tr} \Delta c \quad (0.4)$$

The delta denotes the Laplace operator, here:  $\Delta = \nabla^2$ .

The temperature dependence of the diffusion coefficient usually follows an Arrhenius-law according to:

$$D^{tr} = D_0^{tr} \exp\left(-\frac{E_A}{k_B T}\right) \quad (0.5)$$

$E_A$  is the activation energy that is necessary for the transport of the observed particle,  $k_B$  represents the Boltzmann constant,  $T$  the temperature and  $D_0^{tr}$  the pre-exponential factor.

## 2.2 Diffusion in solids

In the example above, the dye molecules migrate in the liquid solvent by moving between the water molecules which are not fixed in their positions. A macroscopic analogy might be if one jumps in the water and dives under the surface where he can move around freely. Obviously this must be different in solid materials.

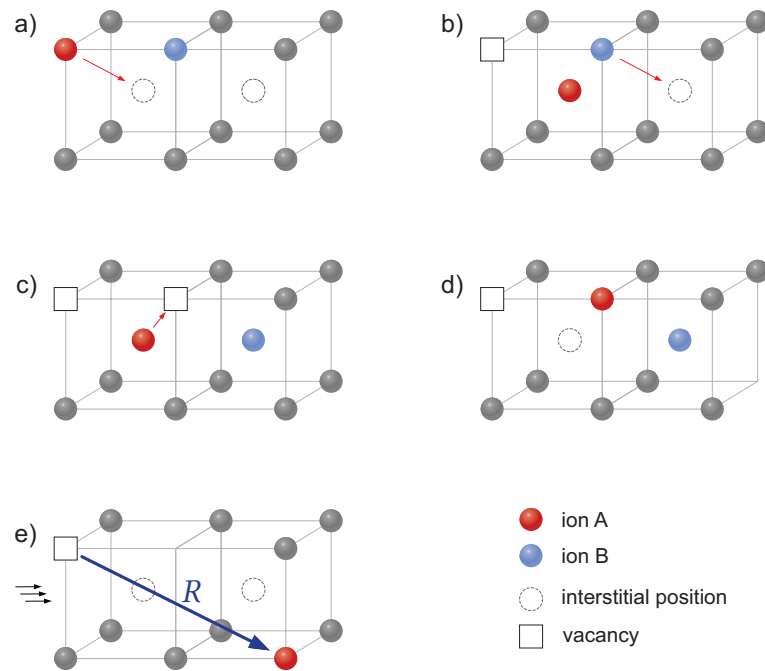
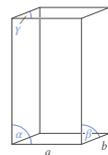


**Figure 2** –Illustration of the migration mechanism of an ion in a solid material crystallized in the *pcc* structure. *R* denotes the total displacement of the ion.

Solids, or more precisely *crystalline solids*, are dense, concrete substances that exhibit a well-defined, distinct arrangement which is described by the different *Bravais-lattices*.<sup>b</sup> These Bravais lattices define a distinct position for each atom and thus restrict a free migration of the diffusing atoms in the solid material. As a result, the atoms or ions can only jump between these given positions.

Such a *microscopic diffusion mechanism* is described in Figure 2, where the ‘red’ ion A is observed on its way through the solid material. The illustrated crystal structure represents a Bravais lattice of a *primitive cubic cell* (*pcc*). In such a *pcc* lattice, it is possible for

<sup>b</sup> The Bravais lattice describes the geometry of the elemental cell of a crystal lattice by the length of the cell edges ( $a/b/c$ ) and the angles between them ( $\alpha/\beta/\gamma$ ).<sup>15</sup>



small ions to move between the regular lattice positions at the edges of the cubic cell, and to jump to interstitial positions that are available in the center of the cubic cells. It is also possible for atoms from a regular lattice position to jump to such an *interstitial site* and leave a *vacancy*, which is an empty site on a regular lattice position. Interstitials and vacancies are of major importance for diffusion in solids and will be explained in detail in the following chapter. If now the ‘blue’ ion fulfills a similar hop, then A can move further on to the available vacancy of B. After a few hops, A has moved from the upper left corner of the left cubic elemental cell to the lower right corner of the right elemental cell.

The motion of such a particle in the crystal lattice is described by the *random walk theory*.<sup>12-14</sup> The *Einstein-Smoluchowski relation* links the total displacement  $R$  (cp. Figure 2e) of the observed particle to the *uncorrelated diffusion coefficient*:

$$D^{uc} = \frac{\langle R^2 \rangle}{2d\tau} \quad (0.6)$$

$d$  is the dimensionality factor for the diffusion process and  $\tau$  the residence time of the particle on a distinct site. The relation between the *uncorrelated* and the *tracer diffusion coefficient* introduced in chapter 2.1 is given by:

$$D^{tr} = f \cdot D^{uc} \quad (0.7)$$

For the correlation factor  $f$  applies:  $0 \leq f \leq 1$ . For a completely uncorrelated motion  $f$  equals 1.

### 2.2.1 Defects in crystal structures

In the chapter above, a crystal structure was described as a periodic, three dimensional arrangement of atoms and that small particles like ions can migrate in such a structure by hopping between available empty sites. Now one can ask the question, where these empty sites in a lattice might originate from? On the one hand, there are so called defects in a real crystal, that can be seen as one characteristic that distinguish an ideal system from a real system. On the other hand, there are interstitial positions that simply result from the geometry of the various Bravais lattices. In Figure 3, the most abundant interstices are presented. A tetrahedral coordination, as it is for example typical in a *pcc* lattice, is illustrated in Figure 3a). An interstice coordinated by an octahedron is displayed in Figure 3b). These coordination spheres also play an important role in crystal structures of binary or multicomponent phases, as smaller ions often sit in the ‘interstices’ of the counter-ions that span the lattice structure. Defects in crystalline compounds result from construction faults of the real lattice and are classified as *point defects*, *dislocations* and *grain boundaries* or *stacking faults*.<sup>15</sup>

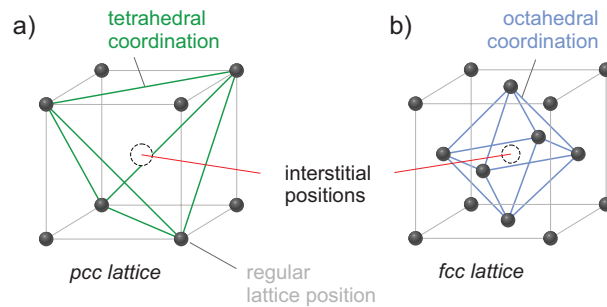


**Figure 3** – Interstice in a tetrahedral (a) and in an octahedral (b) coordination site as a result of the corresponding lattice structure.

### Point-defects

Point defects are zero-dimensional defects that concern individual ions. The simplest case is, when an ion does not sit on its usual position in the lattice, and thus leaves a so called vacancy. If a cation and an anion are missing and the stoichiometry is balanced, it is called a so *Schottky-defect*. A *Frenkel-defect* denotes ions that move from their regular position to interstitial positions in the lattice. Schottky- and Frenkel-defects are shown in Figure 4. They are named after Walter Hans Schottky and Jakow Iljitsch Frenkel which were the first ones that investigated and described these defects. Anions and cations can also switch their positions to form *anti-structure-defects*. If a cation substitutes an anion or vice versa it is an *anti-site defect* that would influence the stoichiometry of the material.

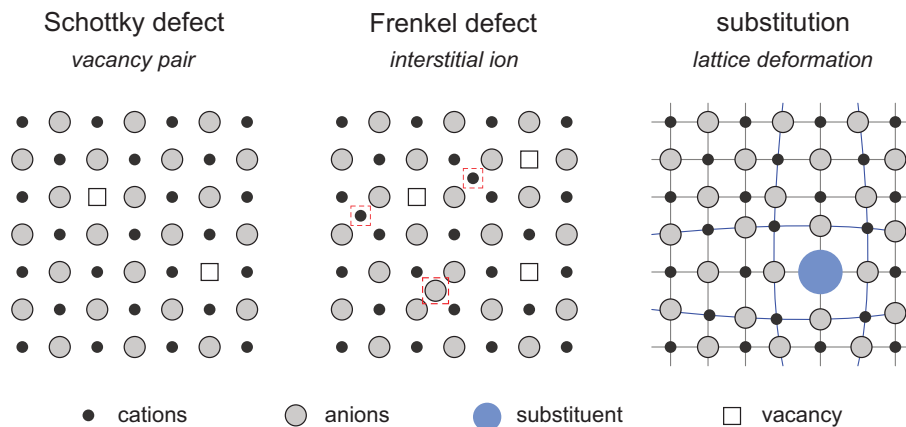


**Figure 4** – Illustration of point defects in crystals, see text for further details.

If foreign atoms are present in the lattice it can be called a chemical defect. Such defects occur very frequent in conventionally prepared as well as natural materials as even in 99.999% pure materials, we can find about  $10^{18}$  foreign atoms in a volume of  $1 \text{ cm}^3$  that is built of about  $10^{23}$  atoms.<sup>15</sup> Such defects can have many influences on the properties of the material such as conductivity. The size of the substituent leads to an expansion or a

contraction of the lattice. If the charge of the substituting ion is different from the host ions it may form vacancies or yield ions on interstitial positions to balance this charge. In that way, this type of defects represents a powerful ‘tool’ to tune the transport parameters of an ion conductor.

### Dislocations

Dislocations or one-dimensional defects have a great influence on the internal structure of a crystal as they can extend across the entire lattice. Dislocations result from the misaligning of the lattice planes in a crystal. Two different types can be distinguished: edge and screw dislocations which are schematically described in Figure 5.

Dislocations can form due to changes in the lattice parameters induced by chemical substitution or can grow due to the expansion of already existing ones. Another important source is the influence of plastic deformation. This is of high importance for the materials discussed in this thesis, as the mechanochemical preparation causes high mechanical stress to the treated materials.

### Grain boundaries and stacking faults

Two dimensional defects such as grain boundaries and stacking faults are present in polycrystalline materials where two or more grains contact each other. They can be classified in small and high angle grain boundaries depending on the angle between the adjacent lattices. Crystal twinning is also possible. Stacking faults are characterized by an error in the sequence of the lattices. This frequently happens in hexagonal close packing (hcp) when the usual ...ABCABCABD... sequence is broken and forms for example ...ABCABABCABD...

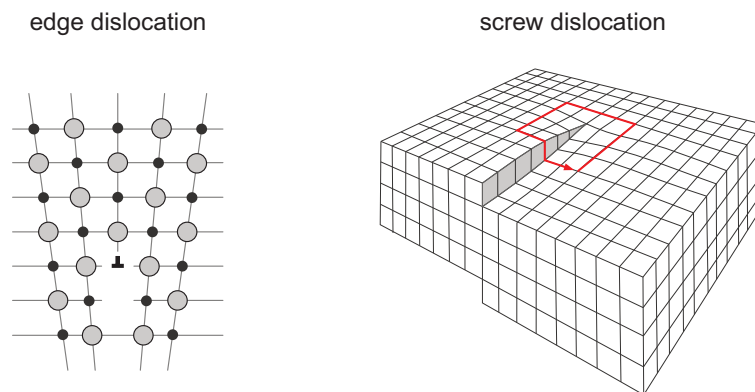


**Figure 5** – Schematic description of two dimensional defects in crystals.

Grain boundaries, surfaces of crystallites and interphase regions can represent important diffusion pathways for ions, as the structure on such surfaces is poorly defined

compared to bulk crystal structures. This can have a significant influence on the bonding and the resulting activation energies for the migration of the ions.

### 2.2.2 Mechanisms of diffusion

The structure of solids resulting from the dense arrangement of atoms or ions restricts the possibilities for ions to migrate in a crystal lattice. In Figure 2, a brief example was given to demonstrate the mechanisms of diffusion in crystalline materials. By the introduction of typical defects in solids in the chapter above, more possibilities for ions to hop between occupied and empty sites or even in-between are given. Detailed information can be found in the books of H. Mehrer<sup>12</sup> and E. Murch<sup>13</sup>.

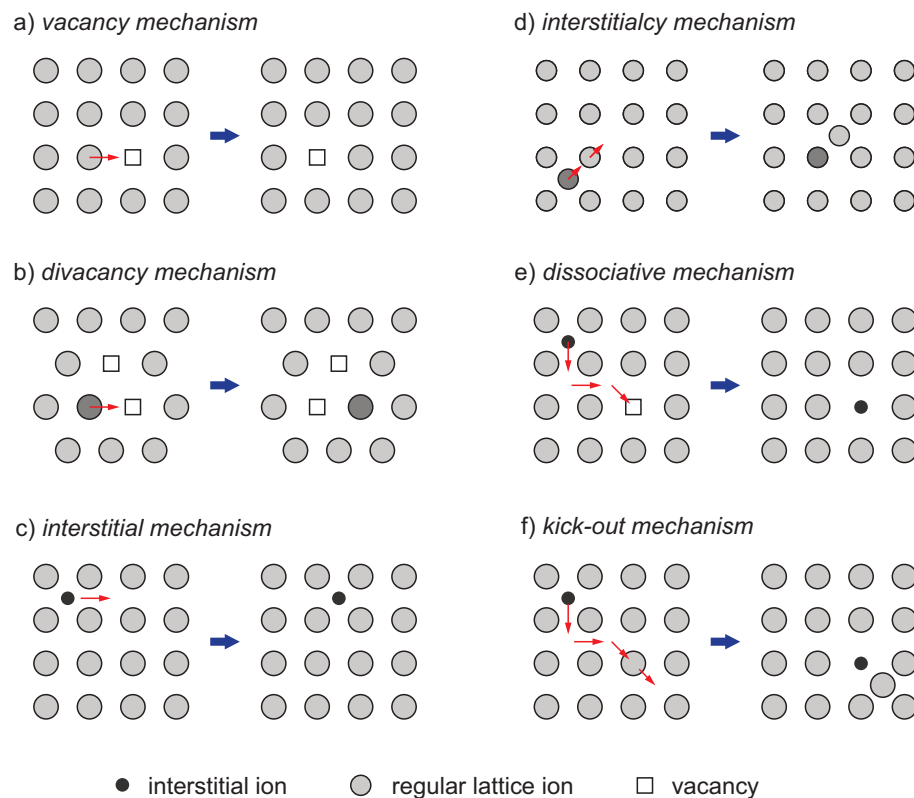


**Figure 6** – Illustration of the different diffusion mechanisms in solids according to reference 12 and 13.

### **Vacancy mechanism**

As Schottky-defects are present in all solid materials, the *vacancy mechanism* is of major importance. It involves a simple jump of an ion to an adjacent vacancy as it is illustrated in Figure 6a). It is the main diffusion mechanism in metals and alloys, but also plays an important role in other materials.<sup>13</sup>

### **Divacancy mechanism**

The *divacancy mechanism* (Figure 6b) is very similar to the vacancy mechanism and arises if a certain binding energy exists between the vacancies. Such agglomerates of vacancies form especially at higher temperatures and can show higher diffusivities as monovacancies, *e.g.*, in fcc metals.<sup>12</sup>

### **Interstitial mechanism**

For the *interstitial mechanism*, hopping ions do not depend on the existence on vacancies, so that they can always jump to the next available site (Figure 6c). Diffusion coefficients for this mechanism are very high.<sup>13</sup> Such interstitial sites are often found in tetra- or octahedral coordination in *bcc* and *fcc* lattices.

### **Interstitialcy mechanism**

In the *interstitialcy mechanism*, two atoms move in unison; an interstitial atom jumps on the site of a lattice atom which hops on an interstitial position, see Figure 6d. The mechanism occurs frequently in ionic materials, especially in those with fluorite structure or in highly defective materials.<sup>13</sup>

### **Interstitial-substitutional mechanism**

The *interstitial-substitutional mechanism* describes two possibilities for solute atoms to migrate in the lattice: the *dissociative* and the *kickout mechanism* (*cp.*, Figure 6e) and f), respectively). Both describe the fast movement of interstitials, but in the dissociative mechanism, the solute jumps on a vacancy and fills a lattice position with a substituent. In the kickout mechanism, the solute atom also fills a regular position after some interstitial hops, but then kicks out a regular solvent atom to form the substituent.

### 3. Measurement of diffusion parameters

The determination of diffusion parameters can be carried out by numerous available methods; some of them are presented in Figure 7.<sup>16</sup> Depending on the interaction with the investigated species, they can be classified by nuclear or non-nuclear methods or macroscopic and microscopic methods. Nuclear methods make use of radioactive ( $\beta$ -NMR) or stable (NMR relaxation spectroscopy) nuclei and other elementary particles.

Tracer diffusion studies, dc-conductivity methods, magnetic field gradient NMR and mechanical relaxation spectroscopy represent macroscopic techniques that trace long-range ion transport. Microscopic methods are also sensitive to localized motions, such as NMR relaxation spectroscopy or  $\beta$ -NMR studies. Quasielastic neutron scattering (QENS) or Mössbauer-spectroscopy (MS) also belong to this set of techniques. Considering impedance spectroscopy (ac-conductivity spectroscopy), I would rather see the method in-between these two categories, as it is yet possible to obtain information about localized diffusion at high measurement frequencies.

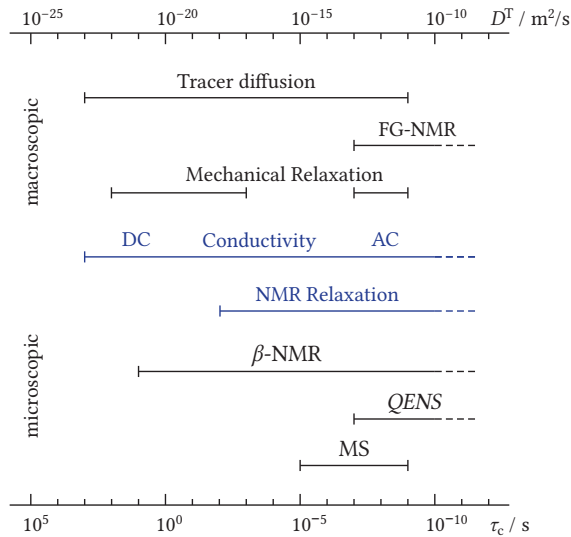


**Figure 7** – Overview on different measurement methods for the determination of diffusion parameters in solids according to reference 16. The scales above and below provide an estimation for the magnitude of the diffusivity  $D^{(T)}$  and the correlation time  $\tau_c$  that are covered by the investigation methods.

In the framework of this thesis,  $^{19}\text{F}$  NMR relaxation spectroscopy was used in conjunction with impedance spectroscopy to investigate the diffusion parameters of the synthesized compounds. Generally speaking, a comparison of diffusion coefficients that are obtained from different methods is recommended in order to get profound knowledge about the diffusion mechanisms in the materials. In the following section I will briefly explain the basics and fundamental characteristics of both methods.

### 3.1 Impedance spectroscopy

Impedance spectroscopy is one of the most frequently used methods for the investigation of solid ionic conductors. It is used to determine the ionic conductivity ( $\sigma$ ) or the dielectric permittivity ( $\epsilon$ ) as a function of the applied measurement frequency. In modern spectrometer setups, the measurement frequency ranges from a few mHz up to several GHz and can additionally be recorded as a function of temperature. The recorded data contains information about the short- and long-range transport mechanisms, activation energies for the hopping processes and the different contributions to the overall conductivity, such as bulk or grain boundary diffusion.

For an impedance measurement, an alternating voltage is applied to an investigated material which is placed between two electrodes, and the resulting current is measured. The ratio of these two quantities  $U/I$  yields the so called impedance  $Z$ , which will be explained in detail in the following section. For further reading I strongly recommend the concise reference book of V. F. Lvovich that clearly outlines the fundamentals of this method and presents useful case studies.<sup>17</sup> More detailed insights into this topic can be found in references 18 and 19.

#### 3.1.1 The concept of complex impedance

A resistor is an electrical circuit element that shows the ability to resist to a flow of current. The resistance  $R$  is defined in *Ohm's law* as the ratio between the applied voltage  $U$  and the output current  $I$ :

$$R = \frac{U}{I} \quad (0.8)$$

For an ideal resistor,  $R$  follows *Ohm's law* at all current, voltage and AC frequency levels.  $R$  [ $\Omega$ ] is independent of the AC frequency and the current and voltage signals are *in phase* with each other. If a material is placed between two conducting electrodes with a certain area  $A$  at a distance  $d$ , the resistance is defined as

$$R = \rho \frac{d}{A} \quad (0.9)$$

with  $\rho$  [ $\Omega$  cm] as the characteristic electrical resistivity of the material. The inverse resistivity is the conductivity  $\sigma$  [ $1/(\text{ohm cm}) = \text{S/cm}$ ] and describes the ability of the material to conduct the electrical current.

If a material that does not conduct the electrical current is placed between the two electrodes, the electrical circuit element is called a capacitor. Such a capacitor can store

electrical energy on the electrodes, if a dielectric material is placed in-between. In this case, the AC current and the AC voltage are *out of phase*. The current ‘follows’ the voltage with a certain *phase shift* ( $\varphi$ ); whether positive or negative depends on the systems characteristics. The capacitance [F] of the element is given by:

$$C = \epsilon_0 \epsilon \frac{A}{d} \quad (0.10)$$

The value of the permittivity of vacuum  $\epsilon_0$  is  $8.85 \cdot 10^{-14}$  F/m.  $A$  is again the area of the electrodes and  $d$  the distance between them. The permittivity  $\epsilon$  can be interpreted as a multiplier for  $\epsilon_0$  and each material possesses its characteristic value.

The complex impedance  $\tilde{Z}$  takes the characteristics of both circuit elements into account and consists of a real and an imaginary impedance term. The real impedance term determines the resistance to the flow of current and the imaginary impedance term gives information about the ability to store electrical energy.

For the measurements of the electrical impedance, a sinusoidal voltage with a small amplitude and a frequency  $\nu = \omega / 2\pi$  is applied:

$$U(t) = U_0 \sin(\omega t) \quad (0.11)$$

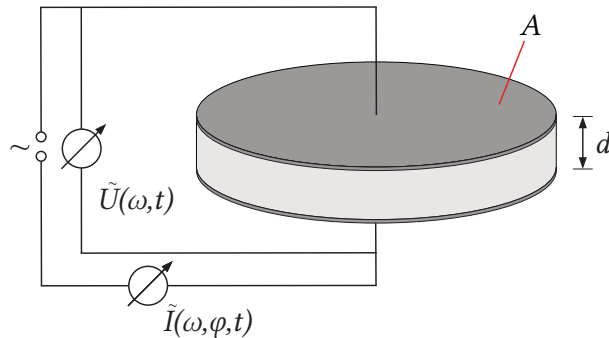


**Figure 8** – Schematic description of the a complex impedance measurement. An AC voltage is applied and the resulting current is measured. The material is placed between two electrically conducting electrodes with area  $A$  separated by the distance  $d$ .

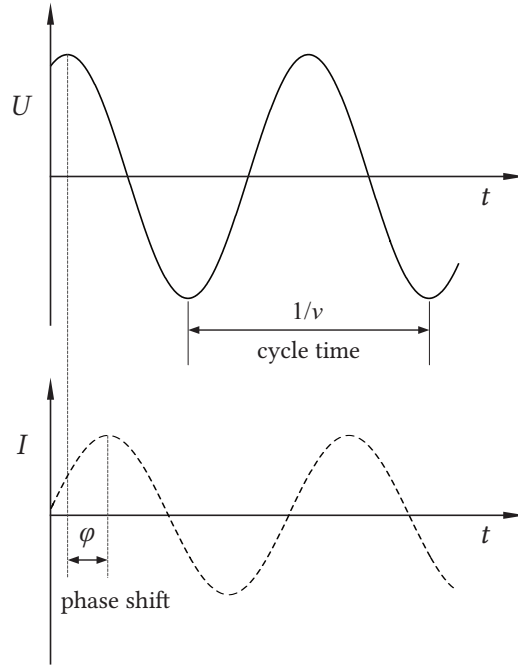


**Figure 9** – Sinusoidal voltage ( $U$ ) and current ( $I$ ) signal as a function of time. The signals are out of phase showing a phase shift  $\varphi$ , when a dielectric material is placed between the electrodes.

The resulting current response is also a sinusoid with the same frequency but has a different amplitude ( $I_0$ ) and is phase shifted ( $\varphi$ ):

$$I(t) = I_0 \sin(\omega t + \varphi) \quad (0.12)$$

The impedance can now be calculated analogous to Ohm's law:

$$Z(\omega, t) = \frac{V(t)}{I(t)} = \frac{U_0 \sin(\omega t)}{I_0 \sin(\omega t + \varphi)} = |Z| \frac{\sin(\omega t)}{\sin(\omega t + \varphi)} \quad (0.13)$$

The impedance can be expressed as a complex function using Euler's relationship:

$$e^{i\varphi} = \cos(\varphi) + i \sin(\varphi) \quad (0.14)$$

Now the expressions (0.11), (0.12) can be written as :

$$\tilde{U}(t) = U_0 e^{i\omega t} \quad (0.15)$$

$$\tilde{I}(t) = I_0 e^{i\omega t - i\varphi} \quad (0.16)$$

The complex impedance follows as:

$$\tilde{Z} = \frac{\tilde{U}(t)}{\tilde{I}(t)} = |\tilde{Z}| e^{i\varphi} = |\tilde{Z}| \cdot (\cos \varphi + i \sin \varphi) = Z' + iZ'' \quad (0.17)$$

The phase angle  $\varphi$  at a certain radial frequency  $\omega$  is the ratio of the imaginary and the real part of the impedance:

$$\tan \varphi = \frac{Z''}{Z'} \quad \text{or} \quad \varphi = \arctan\left(\frac{Z''}{Z'}\right) \quad (0.18)$$

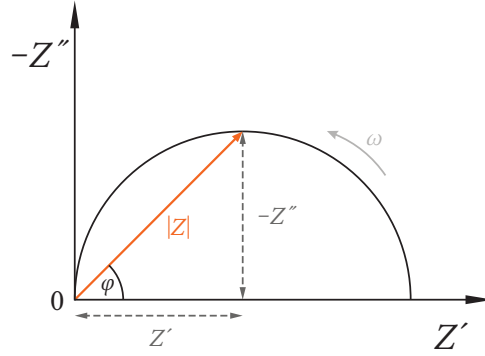


**Figure 10** – Complex impedance plot that shows  $\tilde{Z}$  as a function of rectangular ( $Z', Z''$ ) and polar ( $|\tilde{Z}|, \varphi$ ) coordinates.

### 3.1.2 Permittivity, conductivity and modulus

Dielectric permittivity measurements are carried out as a function of time, temperature and radial frequency. The obtained parameters  $\varepsilon$  and  $\sigma$  can be related to molecular activity. The dielectric permittivity can be interpreted as a material polarization density by the Debye-equation: <sup>17</sup>

$$P = (\varepsilon - 1) \varepsilon_0 V \quad (0.19)$$

At high frequencies (THz) there is a small translational displacement of the electrons in the orbitals. In the kHz-MHz frequency range, a orientational or dipolar polarization occurs, and ionic displacement is observed at frequencies from Hz to kHz.

For an analysis of the dielectric permittivity, it can be written analogous to the complex representation of the complex impedance:

$$\tilde{\varepsilon} = \varepsilon' - i\varepsilon'' \quad (0.20)$$

The real term  $\varepsilon'$  represents the energy storage term and is equivalent to  $1/Z''$ . The imaginary term  $\varepsilon''$  is an inverse equivalent to  $1/Z'$  and represents the ionic conduction

term. Both quantities can be calculated from the capacity  $C$ , the sample resistance  $R$ , the conductivity  $\sigma$  and the resistivity  $\rho$  which are measured in a simple experimental setup:

$$\varepsilon' = \frac{Cd}{\varepsilon_0 A} \quad \text{and} \quad \varepsilon'' = \frac{d}{RA\omega\varepsilon_0} = \frac{\sigma}{\omega\varepsilon_0} = \frac{1}{\rho\omega\varepsilon_0} \quad (0.21)$$

The complex conductivity can be written as the inverse specific complex impedance  $Z_s$ :

$$\tilde{Z}_s = \tilde{Z} \cdot \frac{A}{d} \quad (0.22)$$

$$\tilde{Z}_s = Z'_s - iZ''_s = \frac{1}{\tilde{\sigma}} \quad (0.23)$$

Hence, the real and the imaginary conductivity can be calculated as follows:

$$\sigma' = \frac{Z'_s}{Z'^2_s + Z''^2_s} \quad (0.24)$$

$$\sigma'' = \frac{Z''_s}{Z'^2_s + Z''^2_s} \quad (0.25)$$

At last, the modulus is presented, which can also be defined in relation to the complex permittivity and the complex impedance:

$$\tilde{M} = \frac{1}{\tilde{\varepsilon}} = M' - iM'' = i\omega\varepsilon_0\tilde{Z} = -\omega\varepsilon_0 Z'' + i\omega\varepsilon_0 Z' \quad (0.26)$$

### 3.1.3 Data representations

The dielectric permittivity and the ionic conductivity are usually plotted *versus* the measurement frequency as the shape of the isotherms contains information about the hopping characteristics of the ions. A typical representation of such data, according to Sidebottom,<sup>20</sup> is given in Figure 11.

At the lowest frequencies on the left side, one can see a huge increase of the dielectric permittivity and a small decrease of the ionic conductivity towards lower frequencies. This phenomenon is called *electrode polarization*, which results from the blocking metal electrodes that permit the transfer of the charge carriers to the external measurement circuit. The ‘piling up’ of the ions results in the formation of a space charge at the electrode interface and a drop of the conductivity. The permittivity drastically increases due to a large bulk polarization.<sup>21</sup> In the real part of the conductivity, the polarization regime is followed by a large plateau, the *dc-conductivity plateau*. This plateau represents the long range transport of the ions across the material.<sup>20</sup> It is usually Arrhenius-activated according to  $\sigma_{dc}T \propto \exp(-E_A/k_B T)$  and allows one to determine the average activation energy for the long range transport of the ions. The shoulder in the permittivity isotherm at similar frequencies reflects changes in the dipole moment during the hopping of the ions. At higher frequencies, the conductivity increases following a power law according to  $\sigma' = \sigma_{dc} + Av^\kappa$ , which was described in detail by Jonscher as the *universal dielectric response*.<sup>22</sup> Moving further, the conductivity often shows a linear frequency-dependence.<sup>23</sup> This region is usually called the *nearly constant loss (NCL) regime*. The NCL is still

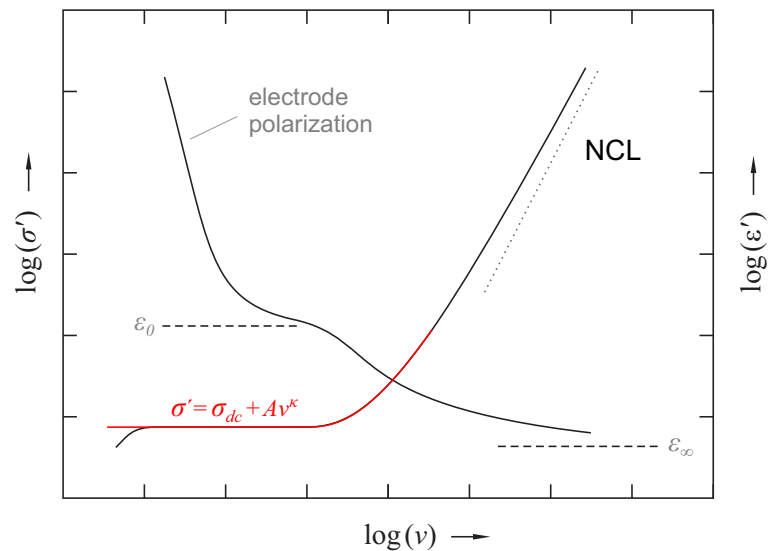


**Figure 11** – Typical shape of conductivity ( $\sigma$ ) and permittivity ( $\epsilon'$ ) isotherms for solid ion conductors according to Sidebottom.<sup>20</sup> The image shows the different characteristics of the material as a function of frequency ( $\nu$ ).

not clearly understood and much debated, but is in general considered to represent localized motion and to be related to the relaxation behavior of unsuccessful forward-backward jumps.<sup>23</sup> The decrease in the dielectric permittivity results from the elastic polarization of the matrix atoms.

A common representation for the complex impedance is the called *Nyquist-plot*. The imaginary part of the impedance is plotted as a function of the real part and the resulting graph usually appears as a semicircle as it is described in the section above. If other processes such as electrode polarization or different diffusion dynamics are present, a series of semicircles or similar elements appear as it is schematically illustrated in Figure 12. The image shows contributions of bulk and grain boundary diffusion and an electrode polarization process. The latter one usually shows up as a spike if blocking electrodes are applied or as another semicircle, which indicates that the charge carriers can pass the sample/electrode interface. Those different regions are usually represented by an *RC* element that contains the resistive and the capacitive circuit element placed in parallel, as it is illustrated in the top section of Figure 12. On the basis of this representation, the different regions can be identified by means of their characteristic *relaxation time*  $\tau$ :

$$\tau = RC \tag{0.27}$$

$$\omega_{max}RC = 1 \tag{0.28}$$

$\omega_{max}$ , the frequency of maximum loss, is indicated by the red circles at the top of the semicircles in Figure 12. It is calculated from the applied frequency  $\nu = \omega/2\pi$ . The re-

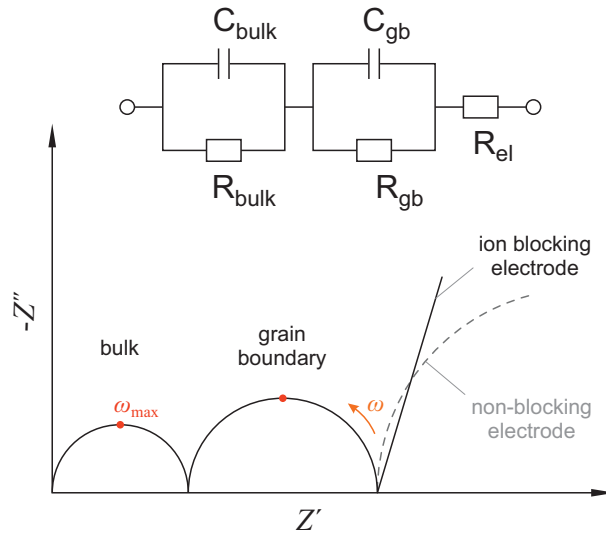


**Figure 12** – Schematic illustration of the complex permittivity of a polycrystalline ion conductor and the corresponding electrical circuit diagram (top).

sistance  $R$  is given by the real part of the impedance  $Z'$  as the section between the intercepts of each semicircle. Now the capacitance of the corresponding process can be calculated. The magnitude of this capacitance provides information about the underlying process as described by West *et al.*<sup>24</sup> Grain boundaries usually exhibit a capacitance that is some orders of magnitude larger than those for bulk processes, which is described by the brick-layer model, see references<sup>24,25</sup> for comparison. As the grains are usually larger in diameter than their corresponding grain boundaries, one can assume  $C_{\text{gb}} \gg C_{\text{bulk}}$  according to  $C = \epsilon_0 \epsilon \cdot A/d$ , cp. eq. (0.10).

### The link between conductivity and diffusion

The conductivity, as one of the most important parameters in the study of solid state ionics by impedance spectroscopy, is linked with a diffusion coefficient via the *Nernst-Einstein relation*:<sup>12</sup>

$$D^\sigma = \frac{\sigma_{\text{dc}} \cdot k_{\text{B}} T}{N \cdot q^2} \quad (0.29)$$

$D^\sigma$  denotes the so called *charge diffusion coefficient*.  $N$  is the charge carrier density and  $q$  the charge of the ions. It must be said that  $D^\sigma$  must not be interpreted similar to the diffusion coefficient of Fick's first law, although it has the same dimensions.

However, it is common in the field of solid state conductors to relate the *charge diffusion coefficient* with the *tracer diffusion coefficient* by the *Haven ratio*  $H_R$ :

$$H_R = \frac{D^{\text{tr}}}{D^\sigma} \quad (0.30)$$

The Haven ratio is discussed controversially and does not have a straightforward physical interpretation.<sup>12</sup> It is thought of as a correlation factor and, *e.g.*, if collective correlation is neglected, it can be related to diffusion mechanisms as discussed in section 2.2.2. A detailed discussion of  $H_R$  can be found in ref<sup>12</sup> and references therein.

## 3.2 Nuclear magnetic resonance spectroscopy

### 3.2.1 The vector model

In contrast to impedance spectroscopy, which is based on the measurement of the dielectric response of a material, nuclear magnetic resonance spectroscopy measures the magnetization  $\mathbf{M}$  of a sample (bold letters outline a vector). The magnetization can be seen as the sum of the magnetic moment  $\boldsymbol{\mu}$  of each atomic nucleus that builds up, when a material with a distinct volume  $V$  is placed in an external magnetic field  $\mathbf{B}$ .

$$\mathbf{M} = \frac{1}{V} \sum_{i=1}^N \boldsymbol{\mu}_i \quad (0.31)$$

The magnetic moment  $\boldsymbol{\mu}$  is derived from an important ‘intrinsic’ property of each atom nucleus, its *spin*. The spin of a nucleus is a quantity that is described by M. Levitt as “difficult to grasp”.<sup>26</sup> The spin of an atomic nucleus is explained in quantum mechanics and in turn results from the spin of the small particles that constitute the protons and the neutrons. For more profound insights into the basics and fundamentals of NMR I refer to the literature, especially the books of M. Levitt<sup>26</sup> and J. Keeler<sup>27</sup> that provide suitable introductory explanations for NMR spectroscopy.

Spin, however, can be interpreted as a sort of inner rotation, which is described by the vector  $\mathbf{I}$ , the *nuclear spin angular momentum*. The magnetic moment  $\boldsymbol{\mu}$  is given by the product of  $\mathbf{I}$  and the *gyromagnetic ratio*  $\gamma$ :

$$\boldsymbol{\mu} = \gamma \cdot \mathbf{I} \quad (0.32)$$

Each nucleus has its own gyromagnetic ratio. The absolute value of  $\mathbf{I}$  is calculated from the *spin quantum number*  $I$  according to:

$$|\mathbf{I}| = \sqrt{I(I+1)}\hbar \quad (0.33)$$

$I$  can take half or integer numbers:  $I = 0, 1/2, 1, 3/2, \dots$  and  $\hbar$  denotes the reduced Planck constant  $\hbar = h / 2\pi$ .

When an external magnetic field  $\mathbf{B}_0$  is applied to the magnetic moment  $\boldsymbol{\mu}$  it experiences a torque  $\mathbf{T}$ , as the field tries to align  $\boldsymbol{\mu}$ .

$$\mathbf{T} = \boldsymbol{\mu} \times \mathbf{B}_0 = \frac{d\mathbf{I}}{dt} \quad (0.34)$$

With  $\boldsymbol{\mu} = \gamma \cdot \mathbf{I}$ , it can be written as:

$$\boldsymbol{\mu} \times \mathbf{B}_0 = \frac{1}{\gamma} \frac{d\boldsymbol{\mu}}{dt} \quad (0.35)$$

As a consequence,  $\boldsymbol{\mu}$  precesses in  $\mathbf{B}_0$  around the  $z$ -axis with a distinct frequency  $\omega_0$  which is known as the Larmor frequency. It shows a characteristic value for each nucleus according to  $\omega_0 = \gamma \mathbf{B}_0$ . At this point, it should be mentioned that the orientation of  $\mathbf{B}_0$  along the  $z$ -axis is defined by convention.

The measurable quantity of  $I_z$  in the field  $\mathbf{B}_0 = (0, 0, B_0)$  is given by

$$I_z = m_I \hbar \quad \text{with } m_I = -I, -I+1, \dots, +I \quad (0.36)$$

$m_I$  is the *magnetic quantum number*. Now eq. (0.32) follows as:

$$\mu_z = \gamma m_I \hbar \quad (0.37)$$

$\mathbf{B}_0$  leads to a splitting of the degenerated energy levels, which is known as *Zeeman splitting*. The energy levels of the magnetic dipoles are calculated according to

$$E_m = -\boldsymbol{\mu}_z \cdot \mathbf{B}_0 = -\gamma \hbar m_I B_0. \quad (0.38)$$

The number of sublevels is given by  $(2I+1)$ . A nucleus such as  $^{19}\text{F}$  with a spin quantum number of  $I = 1/2$  shows two energy sublevels, see Figure 13. The crossing between these energy sublevels upon irradiation with an electromagnetic wave is allowed if the condition  $\Delta m_I = \pm 1$  is fulfilled. The required energy  $\Delta E = h\nu$  is given by the relation  $\gamma \mathbf{B}_0 = \omega_0$ :

$$\Delta E = \hbar |\gamma| B_0 = \hbar \omega_0 = h\nu \quad (0.39)$$

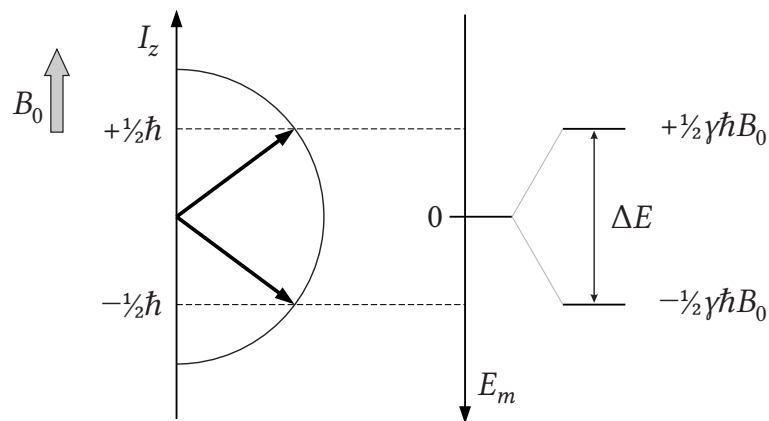


**Figure 13** – Zeeman splitting for a nucleus with spin  $I = 1/2$  if placed in an external magnetic field  $\mathbf{B}_0$ .

The occupancy of these *Zeeman levels* ( $N_m, N_{m-1}$ ) depends on the temperature and follows a Boltzmann-distribution according to

$$\frac{N_{m-1}}{N_m} = \exp\left[\frac{-(E_{m-1} - E_m)}{k_B T}\right] = \exp\left[\frac{-\gamma\hbar B_0}{k_B T}\right]. \quad (0.40)$$

As mentioned at the beginning of this chapter, the net magnetization  $\mathbf{M}$  is the sum  $N$  of all magnetic moments  $\boldsymbol{\mu}$  in a distinct volume  $V$ :

$$\mathbf{M} = \frac{1}{V} \sum_{i=1}^N \boldsymbol{\mu}_i \quad (0.41)$$

Hence, eq. (0.35) can be expressed as follows:

$$\frac{d\mathbf{M}}{dt} = \gamma[\mathbf{M} \times \mathbf{B}_0] \quad (0.42)$$

At thermal equilibrium, the magnetic moments precess in the field  $\mathbf{B}_0$  around the  $z$ -axis so that  $M_z = M_0$  and  $M_x = M_y = 0$ .

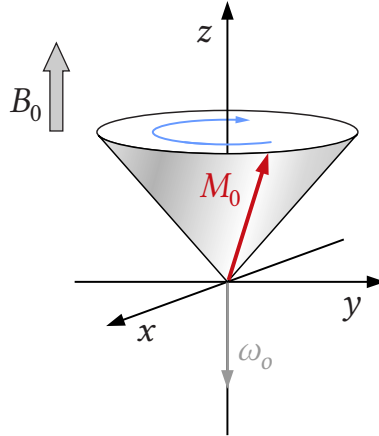


**Figure 14** – Precession of the magnetization  $\mathbf{M}_0$  at thermal equilibrium in the external magnetic field  $\mathbf{B}_0$ .

During an NMR experiment, the thermal equilibrium is distorted with a high-frequency rf-pulse from a small coil that is placed perpendicular to the field  $\mathbf{B}_0$ . The linear polarized high frequency field  $\mathbf{B}_{HF}$  can be expressed by two counter rotating circular polarized magnetic fields  $\mathbf{B}_1$ :

$$\mathbf{B}_{HF} = \mathbf{B}_1 [\cos(\omega t) \mathbf{e}_x - \sin(\omega t) \mathbf{e}_y] + \mathbf{B}_1 [\cos(\omega t) \mathbf{e}_x + \sin(\omega t) \mathbf{e}_y] \quad (0.43)$$

$\mathbf{e}_{x,y}$  is the unit vector pointing in the corresponding direction in the laboratory coordinate system. To simplify the description, the visualization is changed from the stationary laboratory coordinate system to a rotating coordinate system that rotates around  $\mathbf{B}_0$  with  $\omega_0$ . Considering eq. (0.43), one term rotates in the opposite direction of the rotating coordinate system with  $2\omega_0$ , and thus can be ignored, as it is out of resonance. The other term appears stationary along the rotating  $x'$ -axis. The resulting magnetic field  $\mathbf{B}_{\text{eff}}$  is now given by:

$$\mathbf{B}_{\text{eff}} = \mathbf{B}_0 + \frac{\omega}{\gamma} + \mathbf{B}_1 \quad (0.44)$$

The Coriolis-term  $\gamma/\omega$  results from the transformation of the stationary to the rotating coordinate system. If the frequency of  $\mathbf{B}_1$  is equal to  $\omega_0$ , then  $\mathbf{M}$  rotates around  $\mathbf{B}_1$  perpendicular to  $\mathbf{B}_0$ . The angle  $\vartheta$  between fields  $\mathbf{B}_{\text{eff}}$  and  $\mathbf{B}_0$  is dependent on the pulse length  $t_p$ :

$$\vartheta = \omega_1 t_p = |\gamma| \mathbf{B}_1 t_p \quad (0.45)$$

If  $\vartheta$  is  $90^\circ = \pi/2$ , the magnetization  $\mathbf{M}$  is deflected to the  $x,y$ -plane and  $M_z = 0$ . At this point, the Zeeman levels show an equal population of spins. After the  $\pi/2$ -pulse the magnetization undergoes a relaxation process to return to the thermal equilibrium. This relaxation and the time constants that describe these process provide information about the diffusion dynamics of the observed charge carriers in the investigated material and are described in the following section.

### 3.2.2 Relaxation rates

The relaxation of the magnetization towards the thermal equilibrium starts immediately after the irradiation of the rf-pulse that deflects the magnetization into the  $x,y$ -plane. It is characterized by two relaxation time constants  $T_1$  and  $T_2$ .  $T_1$  is the *longitudinal* or *spin-lattice relaxation time* and  $T_2$  denotes the *transversal* or *spin-spin relaxation time*. The change of the magnetization  $\mathbf{M}$  in dependence of  $T_1$  and  $T_2$  is described by the equations of F. Bloch: <sup>28,29</sup>

$$\frac{dM_{z=z'}}{dt} = \frac{M_0 - M_{z=z'}}{T_1} \quad (0.46)$$

$$\frac{dM_{x'}}{dt} = -\frac{M_{x'}}{T_2} \quad \text{and} \quad \frac{dM_{y'}}{dt} = -\frac{M_{y'}}{T_2} \quad (0.47)$$

The spin-spin relaxation time  $T_2$  describes the relaxation of  $\mathbf{M}$  in the  $x',y'$ -plane. It is related to exchange processes in the spin-spin-system. The energy of the system remains

constant while the entropy increases. In addition, the relaxation is induced by inhomogeneities of the magnetic field as well as local environments of other nuclei. The latter enables the powerful structural investigation methods of nuclear magnetic resonance. Diffusion and motion of atoms or ions in the local dipolar fields of the nuclei further contributes to the transversal relaxation rate.

For the determination of  $T_2$ , the decay of the magnetization in the  $y'$ -direction is measured as a function of time:

$$M_{y'}(t) = M_0 \exp\left(-\frac{t}{T_2^*}\right) \quad (0.48)$$

The notation  $T_2^*$  indicates that all of the above mentioned relaxation processes contribute to the time constant. As the magnetization decays, it induces an alternating potential in the rf-coil that is positioned in the  $x,y$ -plane of the magnetic field:

$$U(t) = U_0 \exp\left(-\frac{t}{T_2^*}\right) \quad (0.49)$$

The resulting signal  $U(t)$  is called the free induction decay (FID) and is transformed from a time-dependent signal to a frequency dependent signal via a *Fourier-Transformation* (FT) which yields a Lorentz-shaped function:

$$U(\omega) = \frac{1}{2\pi} \int_{-\infty}^{+\infty} U(t) \exp(-i\omega t) d\omega \quad (0.50)$$

$T_1$  is the spin-relaxation time in which the spin system transfers the energy that was absorbed from the rf-pulse to the lattice via a depopulation of the Zeeman levels with higher energy. As a result, the magnetization again builds up along the  $z$ -axis towards the thermal equilibrium  $M_z = M_0$ . The relaxation is mainly induced by the motion of atoms or ions that induce fluctuations in the field of the nuclei. The magnetization as a function of time is given by:

$$M_z(t) = M_0 \left(1 - \exp\left(-\frac{t}{T_1}\right)\right) \quad (0.51)$$

### 3.2.3 Interpretation of the relaxation data, BPP model

The relaxation rates that are obtained by NMR are usually interpreted in terms of different models such as the one from Bloembergen, Purcell and Pound.<sup>30</sup> The *BPP model* describes three-dimensional, isotropic motion of the nuclei by an autocorrelation function  $G(t)$ :<sup>31</sup>

$$G(t) = G(0) \exp\left(-\frac{|t|}{\tau_c}\right) \quad (0.52)$$

The correlation time  $\tau_c$  is directly linked with the mean residence time  $\tau$  for an atom/ion on its lattice site between two hops. The motion of a nucleus close to another influences the local field around these nuclei and can induce a relaxation process if the resonance condition  $\hbar\omega_0$  is fulfilled.<sup>32</sup> The relaxation rate is connected to a spectral density function  $\mathcal{J}(\omega)$ , which is obtained via Fourier-transformation of  $G(t)$ :

$$\mathcal{J}(\omega) = \int_{-\infty}^{+\infty} G(t) \exp(-i\omega t) dt \approx G(0) \frac{\tau_c}{1 + \omega^2 \tau_c^2} \quad (0.53)$$

$\mathcal{J}(\omega) \propto 1/T_1 = R_1$  links the spectral density function with the relaxation rate  $R_1$ .<sup>33</sup>

The temperature dependence of the correlation time  $\tau_c$  can be expressed by an Arrhenius-law following:

$$\tau_c^{-1} = \tau_{c,0}^{-1} \exp\left(-\frac{E_A}{k_B T}\right) \quad (0.54)$$

$\tau_{c,0}$  is the correlation time at infinite temperature,  $E_A$  again denotes the activation energy for the diffusion/hopping process,  $k_B$  Boltzmann's constant and  $T$  the temperature.

Figure 15 shows an illustration of the temperature dependence of  $R_1$ , respectively  $1/\tau_c$ , in an Arrhenius-diagram.<sup>14,34</sup> The solid curve represents a three-dimensional, isotropic diffusion process described by the BPP model. It shows a symmetric shape with a given maximum and two distinct flanks. At the maximum eq. (0.55) holds: <sup>32</sup>

$$\omega_0 \tau_c \approx 1 \quad (0.55)$$

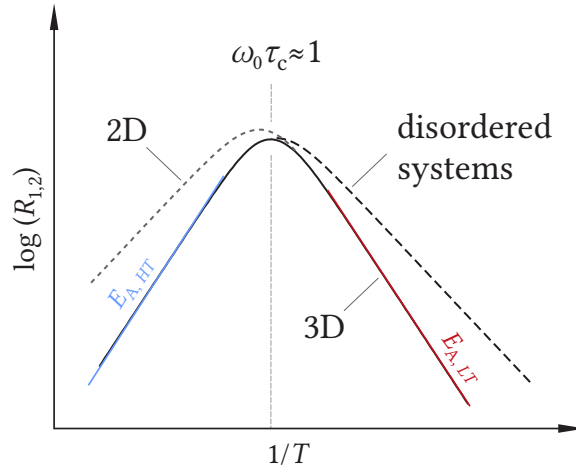


**Figure 15** – Illustration of the temperature dependence of the relaxation rate  $R_1$  for different models based on reference 14 and 34. The slope for a 3D diffusion equals the BPP model and is characterized by symmetrical high- and low-temperature flanks. 2D-diffusion shows a deviation at high temperatures, while disordered systems exhibit a smaller slope at low temperatures.

This signifies, that the average jump rate  $\tau$  of a moving ion equals the Larmor frequency  $\omega_0$ . At higher temperatures  $\tau$  becomes independent of the frequency. The high-temperature flank represents the long range transport in the material. With  $\omega_0 \tau_c \ll 1$  one can write:

$$\frac{1}{T_1} \propto \tau_c \quad \text{with} \quad \tau_c = \tau_{c,0} \exp\left(\frac{E_A}{k_B T}\right) \quad (0.56)$$

At low temperatures  $\omega_0 \tau_c \gg 1$  holds and  $1/T_1$  depends on the jump rate  $1/\tau_c$  and  $\omega_0$ . The low temperature flank contains information about local diffusion parameters, *i.e.*, short range diffusion.

$$\frac{1}{T_1} \propto \frac{1}{\tau_c \omega_0^2} \quad \text{with} \quad \frac{1}{\tau_c} = \frac{1}{\tau_{c,0}} \exp\left(-\frac{E_A}{k_B T}\right) \quad (0.57)$$

The activation energy  $E_A$  can be determined by the slope of the high- and low-temperature flanks.

### Diffusion coefficient by NMR

To compare the obtained diffusion parameters with other methods such as impedance spectroscopy, eq. (0.6) can be applied. A diffusion coefficient can be determined if the crystallographic parameters are known to calculate an average hopping distance  $a$  for the material and if  $\tau_c$  is inserted as the average residence time  $\tau$ .

$$D^{uc} = \frac{a^2}{2d \cdot \tau}$$

The above assumptions and calculations are only valid for isotropic diffusion in homogeneous solids. However, real materials usually show anisotropic diffusion parameters, *e.g.*, due to preferred crystallographic orientations such as layers or channels. Disordered systems such as ball-milled or mechanochemically prepared compounds also show different diffusion characteristics. This anisotropy leads to a different shape of the relaxation rate curves as it is displayed by the dotted lines in Figure 15. Layered compounds usually show a shallower high-temperature slope, while local disorder is expressed at the low-temperature side. Several models have been developed in order to describe these anisotropy-effects. A suitable model that describes the deviations of layered compounds with preferred 2D-diffusion characteristics is found in the work of P. Richards.<sup>35</sup> Non-BPP behavior of structurally disordered compounds is described by Meyer, Maass and Bunde.<sup>36</sup> An overview and discussions of various models was not the primary goal of this thesis and can be found elsewhere in the literature.<sup>31,32</sup>

### 3.2.4 Structural characterization – MAS NMR

Besides the characterization of diffusion processes in solids, NMR enables the structural characterization of chemical compounds. It is an enormously widespread technique in the exploration of molecular structures of organics and inorganics, where it is applied for  $^1\text{H}$  and  $^{13}\text{C}$  nuclei, as well as  $^{31}\text{P}$  or  $^{19}\text{F}$ . However, these substances are usually measured when dissolved in organic solvents where they perform rapid translational and rotational motion so that anisotropic spin-spin interactions between the nuclei are usually underpart. In solids, interactions such as the chemical shift anisotropy or dipolar as well as quadrupolar coupling leads to broad signals.<sup>37</sup> This permits an interpretation of the chemical shift of the individual signals that provide information about the crystallographic positions due to their chemical environment.

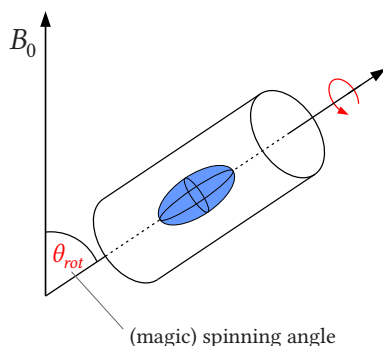


**Figure 16** – The rotor containing the powdered sample is spinning in the external magnetic field  $\mathbf{B}_0$  with a distinct *magic angle*  $\theta_{\text{rot}}$ .

Magic angle spinning (MAS) NMR makes use of a magic trick to narrow the signals: The sample is spun in a rotor in the external magnetic field  $\mathbf{B}_0$ . The angle  $\theta_{\text{rot}}$  between the rotation axis of the rotor and  $\mathbf{B}_0$  is set to  $54.74^\circ$  which is known as the *magic angle*. This leads to the mathematical cancellations in the *internal Hamilton operators* that contain the term  $(1 - 3\cos^2\theta)$  as it equals zero with  $\theta = 54.74^\circ$ . As a consequence, these Hamilton operators are reduced to the terms that describe quadrupolar interactions and chemical shift anisotropy.<sup>38</sup> However, a total simulation of the liquid state is not possible with conventional technical equipment, as the spinning speed of the rotation cannot simulate the conditions of molecular motion in liquids. As a result, so called spinning sidebands appear symmetrically on the left and the right side of the isotropic line in the spectra. But these sidebands can be easily identified by their separation in the chemical shift that depends on the frequency of the rotation speed.

## 4. Mechanochemistry and nanomaterials

### 4.1 Mechanochemical synthesis

Every chemical reaction requires a certain amount of energy to proceed, which is known as the activation energy.<sup>39</sup> For most reactions, this energy is provided by heat, light or an electrochemical potential. In a mechanochemical reaction, the energy is provided by mechanical activation. Over the last years, this type of reaction has found numerous applications across all areas of chemistry. An overview is given by some very

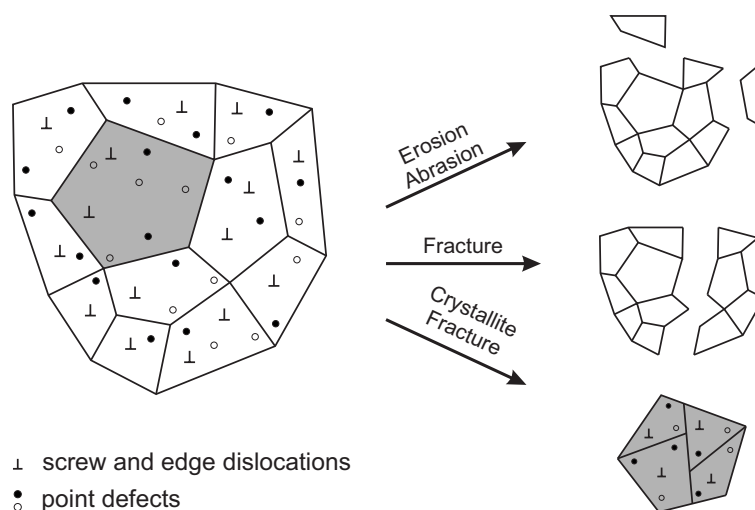


**Figure 17** – Mechanical degradation mechanisms of crystalline material according. Illustration according to reference 43.

comprehensive reviews that were published in the literature lately.<sup>40–42</sup> In terms of solid state chemistry, these mechanochemical reactions mainly show two characteristic aspects. The mechanical treatment of solids leads to a size reduction of the particles and can, under certain conditions, initiate a chemical reaction and induce the conversion to a material with different properties. Figure 17 shows the typical degradation mechanisms and morphological changes that occur during the milling process. The shear and friction forces between the milling tools and the particles lead to abrasion and fracture of the grains and the continuous size reduction yields an increased surface. Moreover, many of the defects that are discussed in chapter 2.2.1 are formed due to the impact of the grinding media on the crystallites. Both processes may have a significant influence on the properties of the treated material such as, *e.g.*, the diffusion parameters.

For the mechanical treatment, many techniques are available that are described elsewhere in the literature.<sup>41,43,44</sup> The materials that were synthesized within the framework of this thesis were prepared by *planetary* or *high-energy ball milling*.

The active parts of a planetary ball mill consist of a rotating disk that carries two beakers that rotate contrary to the disk, as it is shown in Figure 18. The milling tools are made of materials like hardened, corrosion resistant steel, zirconium dioxide or tungsten carbide that resist the harsh synthesis conditions. The use of such material minimizes the degradation of the tools and possible contamination of the synthesized compounds.

During the milling process, shear and friction forces grind and erode the particles when the balls move along the walls due to the centrifugal force.<sup>43</sup> The arrangement and the contrary rotation of the beakers and the supporting disk further lead to an acceleration of the milling balls at a certain point of the rotation so that they move across the beaker and impact on the opposite side, see Figure 18. At this point, the high impact forces of the balls can further crush the particles or induce deformations of the crystal which creates structural defects as they are described in the corresponding section above. Beside the size reduction and structural modifications, the mechanical treatment can trigger chemical reactions. The required energy for the initialization of such reactions originates from the evolution of heat at the contact spots of the particles. First theories from Bowden, Tabor and Yoffe predict temperatures of about 1000 K upon friction at surfaces of about  $1 \mu\text{m}^2$  for  $10^{-3}$ - $10^{-4}$  s.<sup>45-47</sup> Other theories like the Magma-Plasma Model proposes even higher temperatures of up to 10,000 K.<sup>48</sup> A detailed summary of various models and theories describing the effects in mechanochemistry can be found in the book of P. Baláz.<sup>49</sup> The common sense in most of the theories is a very localized evolution of heat that initiates the chemical reaction. In some cases, this enables the synthesis of new compounds that are not accessible by conventional methods. This involves for example amorphous phases that would crystallize upon heating,<sup>50,51</sup> and metastable, or non-equilibrium phases that show crystal structures which differ from a thermodynamically more stable phase.<sup>42,52-55</sup>

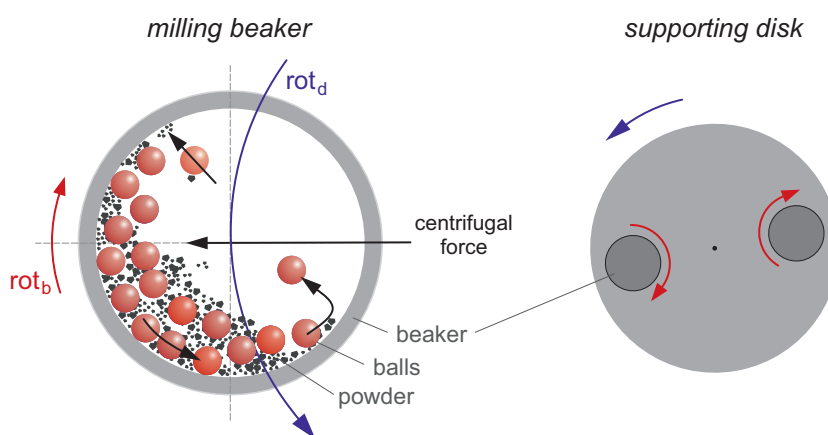


**Figure 18** – Illustration of the milling tools and the principle of operation of a planetary mill. The colored arrows indicate the counter-rotation of the supporting disk ( $rot_d$ ) and the milling beakers ( $rot_b$ ).

## 4.2 Nanocrystalline materials

Nanomaterials can be defined as a ‘separate’ or a ‘special’ branch in materials chemistry, as their small dimensions often account for properties that are different to those of their commonly used, larger-sized counterparts. The definition for nanomaterials is that at least one dimension of the individual particles is less than 100 nm. In terms of crystalline solids or ion conductors with such small dimensions, an important characteristic is the distribution of ions considering their location in a crystallite. In general, boundaries of grains or crystallites diverge in their behavior from bulk material. The short- and long-range order is different, as the boundary atoms are facing different bonding- and energetic environments. Nanocrystalline solids possess much larger surface areas due to their small size. As a consequence, the increased area of grain boundaries or interfacial regions can result in different properties. The relationship between grain size and the percentage of atoms, which are located in such boundaries is described in Figure 19a). The solid line assumes a boundary layer thickness of 1 nm and the dotted line for 0.5 nm.<sup>56</sup> Figure 19b) gives an illustration of such nanocrystalline materials and shows the high amount of surface located atoms.<sup>16</sup>

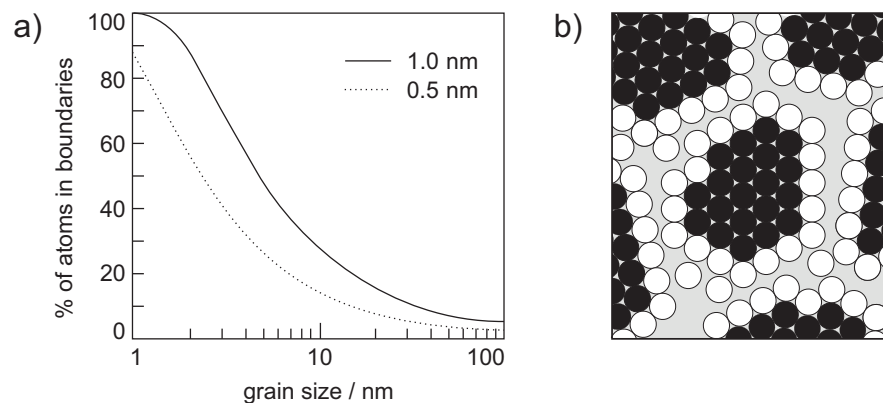


**Figure 19** — a) Graphical description of the relationship between grain size and the percentage of atoms in boundaries and interfaces. Reprinted from reference 56. b) Illustration of nanocrystalline solids on the basis of reference 16.

Nanomaterials have found numerous applications in solid state ionics, especially in energy-related research of batteries and solid electrolytes. The short diffusion length scales for example have opened new possibilities for materials with generally poor bulk properties. Nano-sized electrode materials can now be employed due to their improved properties.<sup>57,58</sup>  $\text{LiFePO}_4$ , which is common in cathodes of lithium ion batteries, is a poor conductor that exhibits low  $\text{Li}^+$  insertion rates if used as a coarse grained compound, but shows good rates as a defect-rich as a nanocrystalline material.<sup>59</sup> Many other materials were also tested and nano-sizing became a major trend in energy-related materials chemistry.<sup>60–64</sup>

In this context, nanocrystalline solid fluoride ion conductors were also investigated towards improved diffusion parameters. As an example, the diffusivity of  $\text{CaF}_2$  can be improved by several orders of magnitude, if it is used as a nanocrystalline powder.<sup>65,66</sup> Sata and co-workers have studied heterostructured nano-layers of  $\text{BaF}_2$  and  $\text{CaF}_2$  which have also shown improved diffusivity compared to the pure substances.<sup>67,68</sup> The mixing of cations is expected to induce a redistribution of the fluorides due to the chemical potential so that some F-ions migrate from the interface region to the  $\text{CaF}_2$  layer. The resulting depletion in the  $\text{BaF}_2$  layer forms vacancies therein and yields interstitials in the  $\text{CaF}_2$  layer. This scenario could explain the enhanced conductivity of such hetero-nanolayers.

An easy access to nanocrystalline ion conductors is enabled by mechanochemistry. On the one hand it can be used as a simple method to obtain nano-sized powders from coarse-grained starting materials or on the other hand to access new materials by mechanochemical reactions. In recent years, mechanochemical milling was employed for the synthesis of many different solid fluoride ion conductors. Mechanochemistry was chosen to synthesize materials that have already been prepared by other methods to investigate the effect of treatment on the properties of the compounds<sup>53,69-73</sup> or for new materials that cannot be accessed by conventional techniques.<sup>52,66,74-77</sup>

However, little is known about the reaction and the proceeding processes during such mechanochemical syntheses of nanocrystalline solids. X-ray diffraction, which is usually employed as a standard method for the characterization of solids, can often not resolve the structural changes that take place as often signals frequently superimpose. The synthesis conditions can further lead to the amorphization of compounds during the milling. Such amorphous compounds are 'invisible' for X-ray diffractometers due to the lack of reflection planes in the material being necessary for the interference of the incident beam. For that purpose,  $^{19}\text{F}$  MAS NMR was used to investigate the syntheses as it allowed to trace the signals of the  $^{19}\text{F}$  nuclei regardless of their state of crystallinity. Hence, it was possible to follow the change of the starting materials during the synthesis and to gather in-depth information about the solid state reactions taking place inside the mill.

## 5. Results and discussion

In the framework of this thesis, several solid state fluoride ion conductors were prepared and thoroughly investigated for their diffusion parameters. All of the materials were prepared by mechanochemical pathways. The practical work began with the synthesis of  $\text{BaSnF}_4$  in order to gather experience about the novel synthesis method as well as the main characterization technique – impedance spectroscopy.  $\text{BaSnF}_4$  was also used as a model compound to study the influence of substitution of  $\text{Ba}^{2+}$  by iso- as well as aliovalent doping. Due to the complexity of the system and the various possibilities for a ‘fine tuning’ of the system, the compound can be considered as partly still under investigation. As a second material, a solid solution of  $\text{BaF}_2$  and  $\text{LaF}_3$  was prepared and also investigated by impedance spectroscopy but on a much broader frequency range up to the GHz-regime. This enabled the exploration of local dynamics that can be accessed at such high frequencies. The findings were additionally supported by NMR relaxation studies, which was the second technique that was used in this thesis to investigate diffusion parameters.  $\text{BaMgF}_4$  was the third F-ion conductor that was synthesized and served as an interesting model substance to study the reaction characteristics of mechanochemical synthesis processes. For that purpose,  $^{19}\text{F}$  MAS NMR was employed in conjunction with X-ray diffraction methods.

In terms of anisotropy, all of the above substances exhibit different characteristics.  $\text{BaMgF}_4$  shows preferred conduction-pathways along its crystallographic *c*-axis.  $\text{BaSnF}_4$  represents a 2D ion conductor due to its double-layer structure.  $\text{Ba}_{0.6}\text{La}_{0.4}\text{F}_{2.4}$  does not show distinct crystallographic orientation, thus can be seen as an isotropic 3D conductor.

In the following chapters, each substance will be explained and discussed in detail. Many of the results that were obtained for the different compounds were published in peer-reviewed journals and are presented in each chapter with an introduction and, if available, additional information to the individual materials.

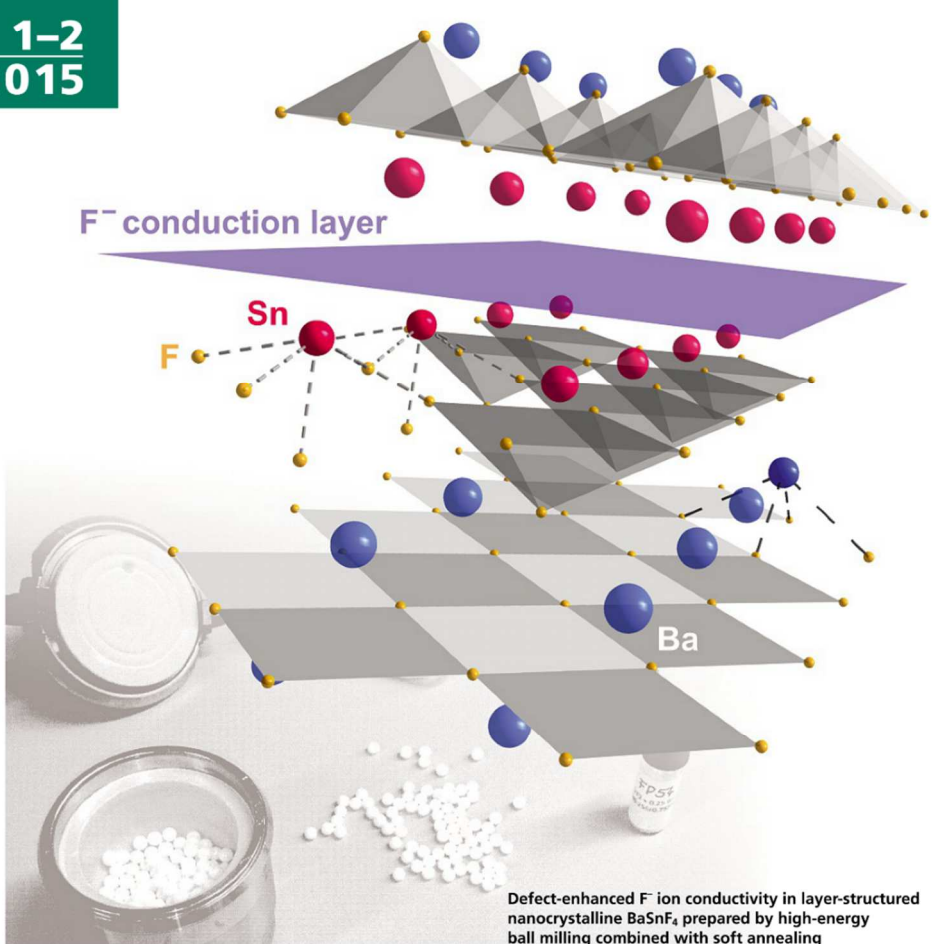


## 5.1 Layer-structured BaSnF<sub>4</sub>

ISSN 1610-1642  
Phys. Status Solidi C  
12 · No. 1–2 January  
1–250 (2015)

physica **p** status **s** solidi **s**<sup>c</sup>  
www.pss-c.com  
current topics in solid state physics

1–2  
2015



**F<sup>-</sup> conduction layer**

**Sn**

**F**

**Ba**

Defect-enhanced F<sup>-</sup> ion conductivity in layer-structured nanocrystalline BaSnF<sub>4</sub> prepared by high-energy ball milling combined with soft annealing  
F. Preishuber-Pflügl, V. Epp, S. Nakhal, M. Lerch, and M. Wilkening

WILEY-VCH

cover-article — *Phys. Status Solidi C*, 2015, 1:

BaSnF<sub>4</sub> is among the fastest F-ion conductors known in the literature.<sup>10</sup> It is a member of the MSnF<sub>4</sub> (M = Ba, Pb) family that crystallizes in a double-layered, tetragonal structure (*P4/nmm*).<sup>78,79</sup> The ordering of the cations follows a sequence of ...-Ba-Ba-Sn-Sn-Ba-Ba-... along the *c*-axis of the unit cell (Figure 20a). This special sequence results from the Sn<sup>2+</sup>-ions that possess an electron lone pair which is sterically demanding.<sup>79</sup> As a consequence, the tin atoms form double layers with their lone pairs pointing towards each

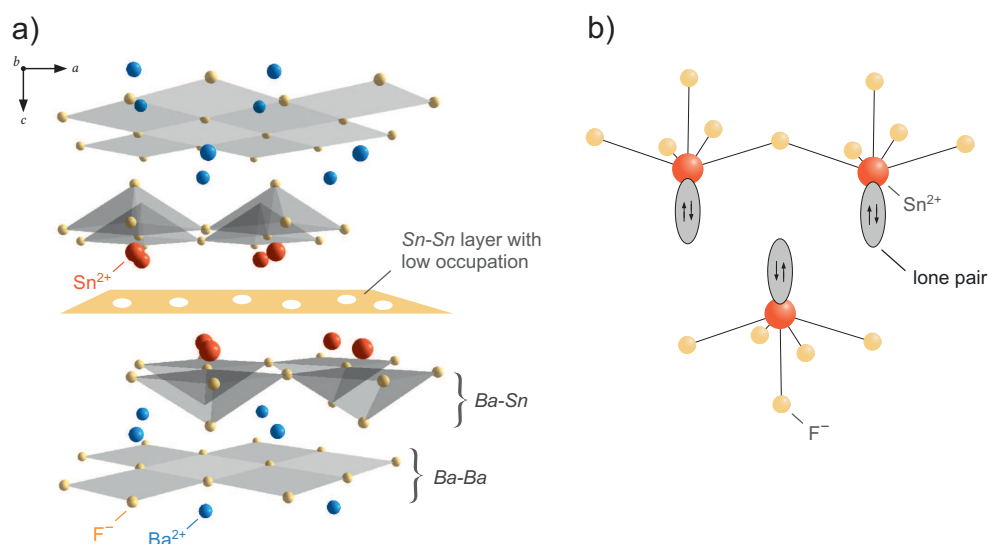


**Figure 20** — a) Modified illustration of the crystal structure of tetragonal BaSnF<sub>4</sub>. The yellow layer with the empty circles was added to highlight the additional *Sn-Sn* conduction layer that shows a low occupation (see text for further details). b) Coordination sphere of the tin(II)-ions illustrating the five-fold coordination by F-ions and the sterically demanding electron lone pair.

other (Figure 20b). In general, the structure of the MSnF<sub>4</sub>-compounds shows a highly disordered character considering the fluoride-ion sublayers as it was determined by Dénès *et al.* by EXAFS, X-ray and <sup>119</sup>Sn Mössbauer studies.<sup>79</sup> These results were later confirmed by Grey and co-workers with <sup>19</sup>F MAS NMR investigations.<sup>78</sup> Dénès found that the *Sn-Sn* layer does not exhibit a strong bonding character which is highlighted by the absence of F-ions in this layer in the crystal structure (ICSD code 166207). However, the occupation with fluoride ions in this layer increases at high temperatures. These results are supported by the temperature-dependent NMR studies that could ‘freeze’ the fast exchange between the *Sn-Sn* and *Ba-Sn* layer. Even at low temperatures such as room temperature, the F-ions are in rapid exchange so that only one line appears in the spectrum due to coalescence of the signals. If the temperature is lowered to about 120 K, other lines become apparent that point occupation of other sites such as those positions in the *Sn-Sn* layer. An exchange with the fluorides in the rigid *Ba-Ba* layer was found to be much slower starting at around 570 K.

The observations described above are summarized in the modified illustration of the crystal structure of BaSnF<sub>4</sub> in Figure 20. The grey, flat plane in the *Ba-Ba* layer shows the rigid F-ions. The pyramids coordinating the tin atoms in the *Ba-Sn* layer indicate the high occupation of this region. To highlight the poorly occupied, but very conductive *Sn-Sn* interlayer, a yellow plane was added. The white circles in the plane depict the empty lattice site that are available for the fast diffusing F-ions. Another representation taken from reference 78 is given in Figure 21 and shows the exchange mechanisms between the distinct sub-lattices in BaSnF<sub>4</sub> that was found in the <sup>19</sup>F MAS NMR study. The analysis of the conductivity that was determined for the synthesized samples and relations to the structural findings of this section will be discussed below.

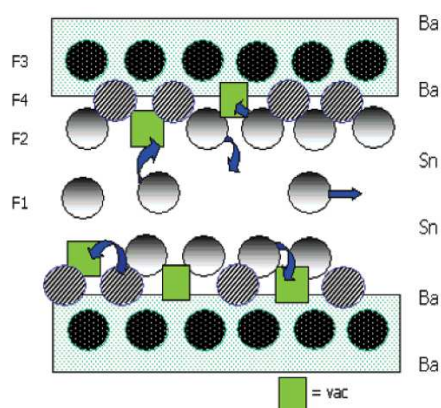


**Figure 21** – Proposed exchange mechanism of F-ions between the different sub-lattices in BaSnF<sub>4</sub> by Grey et. al. Reprinted from reference 78.

Syntheses of tetragonal BaSnF<sub>4</sub> have been demonstrated by various pathways. The first report was a high-temperature synthesis from equimolar mixtures of BaF<sub>2</sub> and SnF<sub>2</sub> by Dénès, Sayer and Bell.<sup>80</sup> In the last couple of years other strategies have been demonstrated including precipitation techniques and mechanochemical syntheses.<sup>70,71,81</sup> The comparison of different preparation methods including a mechanochemical pathway by Patro and Hariharan found a dependence of the conductivity from the particle size of the material.<sup>70</sup> Another conductivity study of BaSnF<sub>4</sub> is available from Ahmad *et al.*<sup>71</sup> Their mechanochemical synthesis is closely related to the approach that was chosen for this thesis (see the publication below for the preparation details). BaF<sub>2</sub> and SnF<sub>2</sub> were milled in the absence of any solvent under air (this work: protective argon atmosphere) for 10 h at room temperature. Subsequently, the obtained sample was annealed for 8 h at 473 K. After milling, they determined a crystal structure for the powder that was closely related to cubic BaF<sub>2</sub> (ICSD code 64717). Thus, the term ‘cubic BaSnF<sub>4</sub>’ will be further used in the discussion to denote the product of the ball milling. Annealing of the ball milled sample at elevated temperatures yielded the above described tetragonal modification. Yet, 7.6%

of the material remained as a cubic impurity. This is not rather surprising as differential scanning calorimetry (DSC) investigations of cubic  $\text{BaSnF}_4$  shows a phase transition at around 475 K (see publication below); their chosen annealing temperature was simply too low. It should, however, be mentioned that a very small cubic phase is also found after annealing at 573 K, as it was done in this work, but higher temperatures often resulted in the decomposition of the sample. The mechanochemical synthesis procedure of this work was further improved by making distinct milling intervals followed by a break to cool down the milling equipment. This enabled the synthesis of a pure, cubic modification as the temperature in the beaker was kept low in order to prevent a partial conversion to the tetragonal modification during the milling procedure. The transformation from cubic to tetragonal has been studied by DSC measurements to determine an appropriate annealing temperature. Detailed results from these measurements can be found in the published data.

Conductivity studies of the as prepared and the annealed material were carried out by impedance spectroscopy at various temperatures from 123 K up to 573 K in a frequency range from 10 mHz to 10 MHz. The Arrhenius representations of the data are found in Figure 22. The corresponding conductivity isotherms are presented in the publication in the following chapter. Figure 22a) shows the values found for the mechanochemically prepared samples. The red symbols represent the data for the as prepared, cubic sample. It was measured at temperatures from 123 K up to 573 K and again down to 123 K. With increasing temperatures, the slope of the curve *viz* the activation energy for the long range ion transport increases. This point is marked by a small grey arrow at a temperature of roughly 410 K. The DSC measurements revealed a small exothermic transition at that temperature which could indicate a structural transformation of the lattice that is accompanied by the observed increase of the activation energy. At around 510 K, another inflection was observed. Above this temperature, the curve collapses with the data points of the tetragonal modification so that the second transition must represent the *in-situ* transformation from cubic to tetragonal. The tetragonal modification shows much lower activation energies and a higher conductivity than the cubic modification. Both tetragonal modifications, regardless if annealed externally or *in-situ* (*cp.* Figure 22 blue symbols, red symbols), show almost identical conductivities and activation energies.

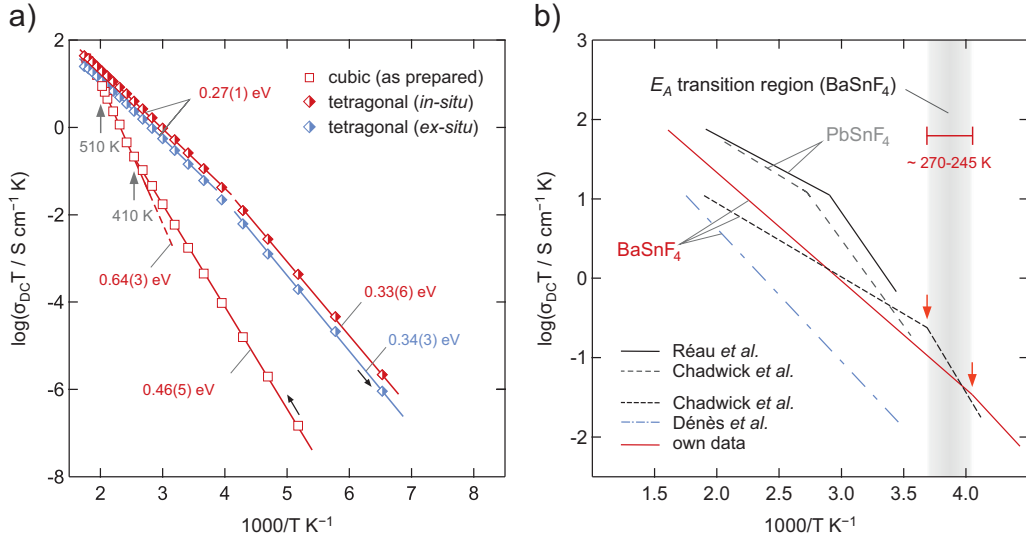


**Figure 22** — Arrhenius plot of the conductivity data ( $\sigma_{DC}T$ ) of various  $\text{BaSnF}_4$ -samples. a) Data of the mechanochemically prepared samples in the framework of this thesis. The red symbols show the data for an as prepared, milled sample that was transformed to the tetragonal modification *in-situ*. For comparison, the values for an externally annealed (2 h, 573 K, Ar atmosphere) sample are also shown. The solid lines represent linear fits of the data. b) Comparison of the data found in this work with literature data from solid state methods. While the group of Dénès and co-workers obtained an activation energy ( $E_A$ ) that does only slightly vary with temperature,<sup>80</sup> Chadwick *et al.* found much lower values for higher temperatures.<sup>82</sup> These findings are in agreement with the data of this work and do agree with the findings of  $^{19}\text{F}$  MAS NMR by Grey *et al.*,<sup>78</sup> see text for details.

At around 245 K the tetragonal modification also shows a change in the conductivity, respectively the activation energy. Above 245 K, the activation energy is about 20% smaller (0.27 eV) than at lower temperatures (0.34 eV). Quite similar results were found by Chadwick *et al.*; they reported even smaller values at high temperatures (0.18 eV) but higher values for low temperatures (0.50 eV).<sup>82</sup> Dénès *et. al* found 0.31 and 0.34 eV (high temp./low temp.) but a much higher temperature for the transition at 400 K.<sup>80</sup> The large deviations between the transition temperatures is unclear yet. The disagreement in the activation energies might be a result of the different preparation techniques or deviations from the 1:1 stoichiometry. It might also originate from a different grain size as a result of the high temperature synthesis. A strong dependence of the synthesis conditions on the structural parameters have been intensively studied and found for  $\text{PbSnF}_4$  in another work of Dénès *et al.* and may show a similar dependence in  $\text{BaSnF}_4$ -systems.<sup>83</sup> However, the observation of the kink in the slope is crucial in particular, as it may indicate a change in the diffusion mechanism of the F-ions that is related to the occupation of the *Sn-Sn* layer, as is described by Dénès<sup>79</sup> and, in particular, the work of Grey.<sup>78</sup>

### Tuning of the conductivity parameters – iso- and aliovalent doping of BaSnF<sub>4</sub>

The disorder in the structure and the high amount of vacancies that are present in the *Ba-Sn* and the *Sn-Sn* sublayers of the tetragonal BaSnF<sub>4</sub> are to some extent responsible for the high conductivity of the sample. The *Ba-Ba* layer, however, permits fast diffusion along the *c*-axis, as the exchange with other F-sites in the local environment, especially at low temperatures, is limited. Thus, this rigid layer was addressed in a follow-up study with the goal to introduce further disorder to these specific sites and increase the exchange with the surrounding mobile ions.

BaF<sub>2</sub> is known as a moderate F-ion conductor, which can be ‘tuned’ by doping with aliovalent ions.<sup>84</sup> Similar results for the structurally related cubic PbF<sub>2</sub> are found in the literature.<sup>85</sup> Substitution of the Ba<sup>2+</sup> ion with monovalent cations is expected to yield anion-vacancies, while trivalent cations bring in additional F-ions that can occupy interstitial sites. Anion-vacancies on regular lattice positions provide pathways for the migration of F-ions and interstitials can increase the total number of charge carriers and in turn enhance the conductivity. Isovalent doping was investigated by the substitution of Ba<sup>2+</sup> with Sr<sup>2+</sup> to influence the lattice parameters due to the difference in the ionic radius. For aliovalent doping, Rb<sup>+</sup> and La<sup>3+</sup> were chosen.

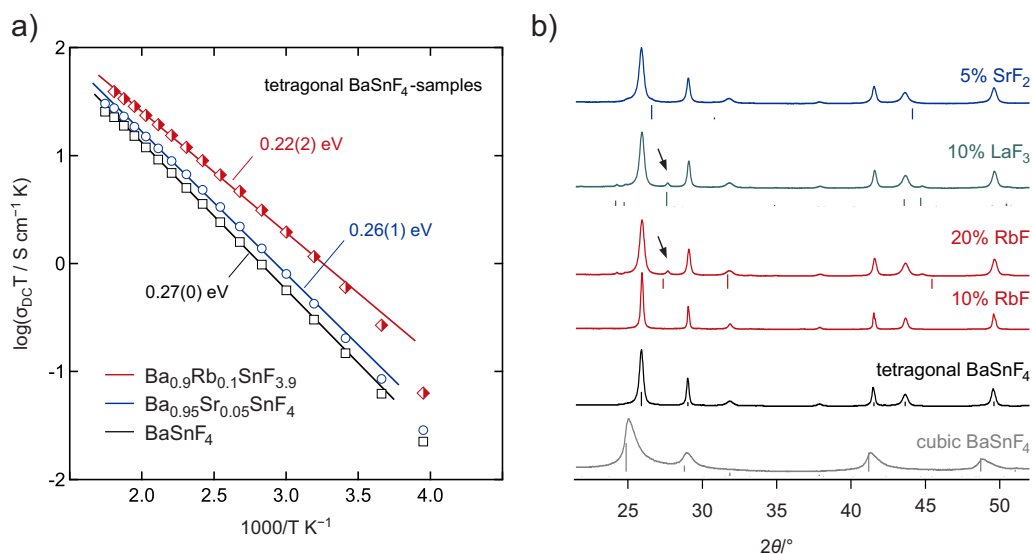


**Figure 23** – a) Arrhenius diagram for tetragonal BaSnF<sub>4</sub>-samples. The samples were milled and subsequently annealed for 2 h at 573 K under protective atmosphere. The black symbols show the conductivity for the pure compound. Higher conductivities are found for the doped samples: the blue circles represent Ba<sub>0.95</sub>Sr<sub>0.05</sub>SnF<sub>4</sub>; red diamonds show Ba<sub>0.9</sub>Rb<sub>0.1</sub>Sn<sub>3.9</sub>. The solid lines are fitted values and are used to calculate the activation energies. b) X-ray powder diffraction pattern of the as prepared, cubic BaSnF<sub>4</sub> and the tetragonal modification including doped samples. The small arrows indicate reflections of the pure dopants that precipitated upon annealing if the concentration exceeded the solubility in the tetragonal lattice. The small vertical bars below the pattern denote the ICSD reference codes of the used dopants (LaF<sub>3</sub>: 89523, RbF: 53828, SrF<sub>2</sub> 41402).

---

The  $(\text{Ba}_{1-x}\text{Sr}_x)\text{SnF}_4$ -system was investigated on the entire composition range from pure  $\text{BaSnF}_4$  to pure  $\text{SrSnF}_4$  with  $x = 0/0.01/0.05/0.10/0.20/0.25/0.50/0.75/1$ .<sup>c</sup> The highest values were found  $\text{Ba}_{0.95}\text{Sr}_{0.05}\text{F}_4$ . In general, the conductivity decreased with increasing amounts of strontium fluoride.  $\text{LaF}_3$  was added with 1, 5, 10 or 20 mol% nominally yielding  $\text{Ba}_{1-x}\text{La}_x\text{SnF}_{4+x}$ . However, if the  $\text{La}^{3+}$ -content exceeded 10%,  $\text{LaF}_3$ -reflections were found in the X-ray pattern due to segregation upon annealing, which points to a low solubility of  $\text{La}^{3+}$  in the  $\text{BaSnF}_4$  structure (see Figure 23). Lower amounts than 10%  $\text{LaF}_3$  did not change the conductivity compared to pure tetragonal  $\text{BaSnF}_4$ . Thus, this system was not further investigated. A significant increase of the conductivity was observed upon doping with 10%  $\text{RbF}$ . This points to an improvement of the F-diffusivity due to a vacancy mechanism.

The values for the different samples are shown in Figure 23. At room temperature, the dc-conductivities for the different tetragonal samples are:  $5.40 \cdot 10^{-4}$  S/cm (unsubstituted  $\text{BaSnF}_4$ ),  $7.07 \cdot 10^{-4}$  S/cm (5%  $\text{SrF}_2$ ) and  $2.05 \cdot 10^{-3}$  S/cm (10%  $\text{RbF}$ ). The activation energy for the long range transport was also found to be lower for the doped samples, *cp.* Figure 23.

In general, it can be stated that the monovalent doping with  $\text{RbF}$  was most successful. However, it is not possible to concretely relate the influence of the substitution of  $\text{Ba}^{2+}$ -cations to a distinct fluoride exchange/diffusion mechanism. Currently, theoretical calculations about the structural parameters of the doped compound as well as EXAFS studies are in progress.

---

<sup>c</sup> The preparation and investigation of the  $(\text{Ba}_{1-x}\text{Sr}_x)\text{SnF}_4$ -system was carried out under supervision by Maria Gombotz in the framework of a Bachelor thesis.



---

P1: (pp. 47-51)

**Defect-enhanced F ion conductivity in layer-structured nanocrystalline BaSnF<sub>4</sub>  
prepared by high-energy ball milling combined with soft annealing**

F. Preishuber-Pflügl, V. Epp, S. Nakhal, M. Lerch, and M. Wilkening,  
*Phys. Status Solidi C*, 2015, **12**, 10.



# Defect-enhanced $F^-$ ion conductivity in layer-structured nanocrystalline $BaSnF_4$ prepared by high-energy ball milling combined with soft annealing

Florian Preishuber-Pflügl<sup>\*1</sup>, Viktor Epp<sup>1</sup>, Suliman Nakhal<sup>2</sup>, Martin Lerch<sup>2</sup>, and Martin Wilkening<sup>1</sup>

<sup>1</sup> Institut für Chemische Technologie von Materialien, TU Graz, Stremayrgasse 9, 8010 Graz, Austria

<sup>2</sup> Institut für Chemie, TU Berlin, Straße des 17. Juni 135, 10623 Berlin, Germany

Received 18 July 2014, accepted 25 September 2014

Published online 19 November 2014

**Keywords**  $BaSnF_4$ , mechanosynthesis, high-energy ball milling, fluorine ion conductor, ionic conductivity

\* Corresponding author: e-mail preishuber-pfluegl@tugraz.at

Fast ion conductors play one of the most important roles in solid state ionics as there is a great demand for their application in safe and powerful electrochemical energy storage systems. For such materials, it is known that the synthesis conditions may have significant impact on the final properties of the materials prepared. In this contribution, we made use of mechanosynthesis, carried out via high-energy ball milling, to influence the ionic transport parameters of tetragonal, *i.e.*, layer-structured,  $BaSnF_4$ . X-ray powder diffraction (XRD) revealed that mechanical treatment of the binary fluorides  $BaF_2$  and  $SnF_2$  leads to a powder pointing to a nanocrystalline fluoride with (distorted) cubic symmetry. Differential scanning calorimetry (DSC) as well as preliminary *in situ* XRD measurements were used to follow the transformation towards

the tetragonal modification with the composition  $BaSnF_4$ . Broadband impedance spectroscopy was used to measure the overall electrical conductivity of the ternary fluoride. Remarkably, the layered form shows a room temperature conductivity of  $7 \times 10^{-4} \text{ S cm}^{-1}$ . Further emphasis was put on the characterization of the dielectric properties of the material, which was investigated by using different electrode materials to distinguish artefacts from intrinsic properties. Since we found a strong dependence of the real part of the permittivity on the electrode materials applied (carbon paste or sputtered Pt), we tend to assign the huge increase in permittivity, which was recently interpreted as giant dielectric constant, to interfacial polarization effects rather than to intrinsic properties.

© 2014 WILEY-VCH Verlag GmbH & Co. KGaA, Weinheim

**1 Introduction** The development of modern energy storage systems other than conventional lithium-ion technologies has revived research activities on all-solid-state batteries. Alternative electrochemical energy storage systems based on fluorine ion conductors, which had already been investigated by Schoonman and co-workers [1,2] in the late 70s, have been put back in the spotlight of research [3]. Besides the choice of proper active materials, an electrochemically stable solid electrolyte with sufficiently high ionic conduction and negligible electronic transport is required to shuttle the ions required for the electrode reactions.

Outstanding room temperature ionic conductivity has been found for tetragonal  $BaSnF_4$ , which makes it a prospecting candidate for its application in both electrochemi-

cal storage systems and sensors. However, comparisons of published literature data points to a strong dependency of the conductivity on the preparation method applied [4–7].

High-energy ball milling provides a versatile synthesis method with many adjustable parameters to prepare functional materials with properties being different with regard to their conventionally synthesized analogues [8]. Mechanical impact during milling is known to introduce large amounts of structural disorder and microscopic strain that can largely influence ionic transport [9, 10]. In addition, the nm-sized crystallites obtained make surface related effects visible and let them govern macroscopic properties. They comprise interfacial regions such as grain boundaries that may provide energetically preferred diffusion pathways for the moving ions [11]. Fine tuning of the milling

conditions applied during mechanosynthesis in combination with subsequent soft annealing allowed us to prepare highly conductive, nanocrystalline  $\text{BaSnF}_4$  with tetragonal symmetry. The sample prepared almost reached electrical conductivity values of isostructural  $\text{PbSnF}_4$ ; so far, the latter still represents the fastest  $\text{F}^-$  conductor at room temperature, see Ref. [12] for an overview.

Differential scanning calorimetry (DSC) and X-ray powder diffraction (XRD) allowed us to collect information on the transformation from the original, ball-milled  $\text{BaF}_2\text{-SnF}_2$  mixture to the tetragonal modification. The dielectric properties of our samples were determined by temperature-dependent broadband impedance spectroscopy. Besides the analysis of conductivity spectra, in particular, permittivities as a function of frequency were analyzed in terms of external electrode polarization effects. Considering  $\text{BaSnF}_4$  the latter is controversially discussed in the literature [4, 13].

## 2 Experimental

**2.1 Sample preparation** The binary fluorides were purchased from commercial sources ( $\text{BaF}_2$ , 99.99%, Sigma-Aldrich;  $\text{SnF}_2$ , 99%, Alfa Aesar); before treatment in a planetary ball mill (Fritsch Pulverisette 7 premium line) they were dried in vacuum. For the mechanochemical reaction we used beakers (45 mL) made of  $\text{ZrO}_2$  in combination with 180 balls of the same material (5 mm in diameter). The ball-to-powder ratio was 17:1; the total milling time was set to 10 h. This time period does not include the cooling intervals in between. Handling of the starting materials as well as the product and the milling tools was strictly carried out in a glovebox filled with dry argon ( $\text{O}_2$  and  $\text{H}_2\text{O} < 0.5$  ppm) to avoid any contamination with water and to prevent oxidation of the reactants during milling.

**2.2 X-ray diffraction** The final mechanosynthesized product was characterized by X-ray powder diffraction, which was carried out under air with a Bruker D8 Advance diffractometer using Bragg Brentano geometry and  $\text{Cu K}_\alpha$  radiation (10 to  $100^\circ 2\theta$ , step size  $0.02^\circ 2\theta$ , step time 1 s). Rietveld refinement was done with X-PertHighScorePlus (PANalytical).

**2.3 Differential scanning calorimetry** DSC measurements were performed with a Netzsch STA 409 differential scanning calorimeter coupled with a QMS 403C mass spectrometer. The sample was heated under a constant helium gas flow in platinum crucibles at a rate of 10 K/min; starting from 293 K measurements were carried out up to 1000 K.

**2.4 Impedance spectroscopy** For the dielectric measurements 200 mg of the polycrystalline powder were pressed in a mould with 10 mm inner diameter applying a uniaxial pressure of 0.13 GPa yielding pellets of about 1 mm in thickness, each time measured with an appropriate caliper. Pt electrodes with a thickness of 100 nm were ap-

plied on both sides of the pellet with a sputter coater (Leica) to ensure good electrical contact; graphite electrodes were applied using a graphite paste.

Impedance spectra were measured with a Novocontrol Concept 80 broadband analyzer equipped with a BDS 1200 cell in combination with an active ZGS cell interface allowing temperature-variable two-electrode (dielectric) measurements. Frequencies covered a range of nine decades, starting from  $10^{-2}$  Hz up to 10 MHz. The temperature was varied from 133 K to 573 K in steps of 10 to 20 K; this is automatically controlled by a QUATRO cryosystem (Novocontrol). During the measurements, a dry nitrogen atmosphere with the appropriate temperature is built up around the sample in the cryostat. This is achieved by a constant flow of  $\text{N}_2$  gas, freshly evaporated from a dewar containing liquid nitrogen.

**3 Results and discussion** As presented by the XRD patterns shown in Fig. 1, ball milling of  $\text{BaF}_2$  and  $\text{SnF}_2$  leads to a fluorite phase with distorted cubic symmetry. Vertical bars show the reflections of pure, Sn-free cubic  $\text{BaF}_2$ . The absence of any XRD peaks of  $\text{SnF}_2$  either points to a complete incorporation of tin fluoride into the fluorite structure or to a partial incorporation while X-ray amorphous  $\text{SnF}_2$  is left over. As estimated by the well-known Scherrer equation, the average crystallite size of the ball milled sample is approximately 10 nm. This rough estimation disregards, of course, strain introduced via mechanical impact as well as the possibility that the broadened peaks observed represent a distributions of XRD reflections. Mean crystallite sizes less than 30 nm, however, are reasonable since such values are found for many oxides and fluorides treated for several hours in high-energy ball mills.

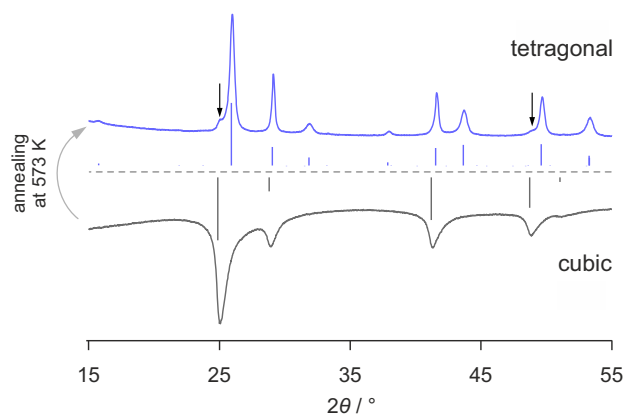


**Figure 1** X-ray powder diffraction pattern of the as-prepared sample (bottom) and after the *in situ* transformation during our impedance measurements (top). Vertical lines show XRD reflections of cubic and tetragonal  $\text{BaSnF}_4$ .

Here, the ball-milled product was transformed into the tetragonal modification *in situ* during the temperature-dependent conductivity measurements inside the imped-

ance cell. Residual amounts of the cubic phase observed in the pattern recorded after the dielectric measurement is presumably due to the relatively short time the sample had been exposed to elevated temperature inside the impedance cell. A complete transformation could be achieved by controlled annealing at 573 K for at least 2 h in a dry, oxygen-free protective gas atmosphere. This treatment, however, leads to non-negligible narrowing of the XRD peaks because of grain growth; the average crystallite size increased from 10 to 22 nm.

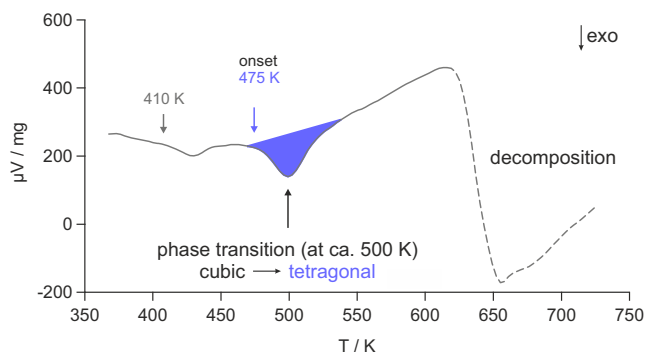


**Figure 2** DSC curve of the as prepared cubic BaF<sub>2</sub>-SnF<sub>2</sub> mixture measured under inert gas atmosphere (He) with a heating rate of 10 K/min.

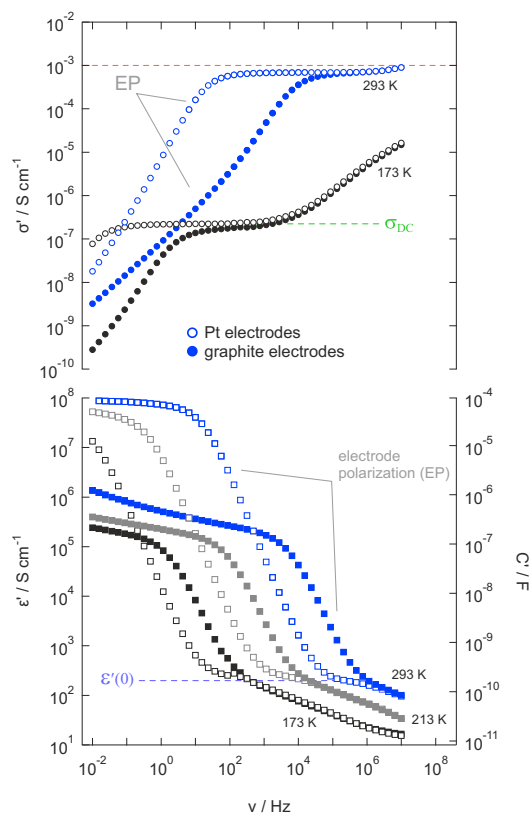
To get further insights into the structural changes and the phase transformation of the initially cubic phase upon heating, DSC and preliminary *in situ* XRD measurements were carried out. DSC measurement (see Fig. 2) reveal two exothermal processes in the temperature range of our impedance measurements. The shallow peak with an onset temperature of 410 K initiates structural changes in the material that could also be detected by first *in situ* XRD measurements; the latter shows some additional, yet unidentified reflections that disappear upon further heating. The main transformation into the tetragonal phase starts at 480 K as is reflected by the intensive signal of the DSC curve. The transformation could be verified by *in situ* XRD. Moreover, it is associated with a change of the DC conductivities probed *in situ*, as will be discussed below.

Figure 3 gives a brief overview of the dielectric properties of the mechano-synthesized BaSnF<sub>4</sub> crystallizing with tetragonal symmetry. The figure shows selected conductivity and permittivity isotherms, that is, the real part of the complex conductivity and permittivity,  $\sigma'$  and  $\epsilon'$ , plotted vs. the frequency  $\nu$ . DC conductivities, reflecting long-range ion transport, can be directly read out from the distinct frequency-independent plateaus which pass over into the dispersive regime reflecting short-range motions of the charge carrier such as (correlated) forward-backward jumps.

Interestingly, at 293 K the layer-structured fluoride prepared exhibits a very high DC conductivity  $\sigma_{DC}$  of  $7 \times 10^{-4} \text{ S cm}^{-1}$ , which is comparable to the results of some of the PbSnF<sub>4</sub> samples analysed so far [7, 12, 14, 15]. In agreement with the study of Chadwick *et al.* [7] this value

represents one of the highest conductivities reported for BaSnF<sub>4</sub> when the mechano-synthesized product studied here is compared with samples prepared via other routes such as high temperature synthesis, wet chemical methods or other mechanochemical approaches including the various types of ball milling [4-7].

The enhanced overall conductivity might be attributed to the large concentration of defects (including strain) introduced during milling. These may largely affect both short- as well as long-range ion transport. In contrast to our approach, other mechano-assisted synthesis routes involved the use of liquids during milling [6]. As a consequence, the mechanical impact on the powder is expected to be less than in our case, hence, leading to a lower degree of (micro-)structural disorder preserved in the layered structure.



**Figure 3** Conductivity and permittivity isotherms of mechano-synthesized, tetragonal BaSnF<sub>4</sub>. Filled symbols represent data acquired with graphite electrodes while non-filled symbols show the results when Pt electrodes were applied.  $\sigma_{DC}$  gives the bulk conductivity of the sample;  $\epsilon'(0)$  is the intrinsic permittivity at low frequencies, which is, as the corresponding value  $\epsilon'(\infty)$ , independent of the electrodes (Pt or C) applied.

As is well known when ion-blocking electrodes are used to measure conductivity spectra of fast ion conductors, at a certain frequency  $\sigma'$  starts to decrease, even stepwise [13], a phenomenon well-known as electrode polarization (EP). The fast movement of the ions towards the blocking electrodes leads to the formation of a space charge zone that

slows down further transport of the charge carriers [13, 16]. As it is demonstrated in Fig. 3, this phenomenon depends on the applied electrode material: graphite electrodes lead to a different polarization effect than it is observed for the same sample but equipped with Pt electrodes. The drop-off in conductivity is associated with an increase in permittivity  $\epsilon'$ ; the corresponding isotherms are displayed in the lower part of Fig. 3. The huge low-frequency permittivity values have recently been interpreted as an intrinsic giant dielectric constant effect [4]. The large difference of almost two orders of magnitude between the values measured for different electrode materials seems to weaken this interpretation. To our opinion the isotherms simply reflect non-intrinsic interface-electrode effects as observed for many different ion conductors and discussed in detail by Loidl and co-workers [13].

Besides these external interface polarization showing up at low frequencies ( $\nu \rightarrow 0$ ) and sufficiently high temperatures, another plateau, labelled with  $\epsilon'(0)$  in the permittivity spectra of Fig. 3, can be seen. When going to higher frequencies both  $\sigma'(\nu)$  and  $\epsilon'(\nu)$  coincide irrespective of the electrode material applied. In contrast to the situation in the EP regime, now the intrinsic properties are probed, which are related to polarization effects of the mobile ions vs. the immobile matrix [16]. The right axis of the  $\epsilon'(\nu)$  plot displays the corresponding capacities calculated from the permittivity values shown on the left side. Compared with typical values found in impedance spectroscopy, see, e.g., Irvine *et al.* [17]  $\epsilon'(0)$  is in the range of the grain boundary response. If we, however, interpret the conductivity values as bulk response, the relatively high value of  $\epsilon'(0) = 2 \times 10^2$  might be associated with results reported for materials with relatively large dielectric constants at inter-grain boundaries or with so far unknown internal effects of  $\text{BaSnF}_4$  [4]. For many materials, however, intrinsic constants  $\epsilon'(\infty)$ , accessible at sufficiently high frequencies only, are expected to be in the order of  $10^2$  or less [18]. In our case we found  $\epsilon'(\infty) < 20$  at 173 K. The aforementioned high permittivity at even lower frequencies, however, is in agreement with values usually reported for sample-electrode interface processes; in such cases depletion layers formed are responsible for Maxwell-Wagner type relaxation processes that are measured by using metallic electrodes and two-point contact standard configurations [18].

The frequency independent DC-plateau, indicated with  $\sigma_{\text{DC}}$  in Fig. 3 and as mentioned above, represents the bulk (overall) conductivity for long-range charge carrier transport of mechano-synthesized  $\text{BaSnF}_4$ . The values found for the bulk conductivity are plotted as  $\sigma_{\text{DC}}T$  versus the inverse temperature in the Arrhenius diagram in Fig. 4.

The Arrhenius plot shows the first heating run of the as prepared cubic sample up to 573 K as well as the  $\sigma_{\text{DC}}T$  values for the tetragonal modification, annealed inside the impedance cell, upon cooling down to 133 K. The dashed lines represent linear fits with an Arrhenius law and enable

the determination of the (average) activation energy ( $E_a$ ) according to  $\sigma_{\text{DC}}T \propto \exp(-E_a/(k_B T))$ ;  $k_B$  denotes the Boltzmann constant. The differences in the slopes of the Arrhenius fits, *i.e.*, the activation energy required for long-range movement of the ions, indicates a change in transport mechanism: Starting with  $E_a = 0.51$  eV the activation energy changes to 0.65 eV at higher temperatures (see Fig. 4). Roughly around 500 K the slope decreases again, which is related to the cubic-tetragonal phase transformation. Layered  $\text{BaSnF}_4$  prepared in this way shows a very high DC conductivity combined with a relatively low activation energy of 0.27 eV.

Upon further cooling, long-range charge carrier transport changes again; the data points recorded below ambient temperature follow an Arrhenius law with an activation energy of 0.34 eV. Interestingly, a break of the Arrhenius line was also observed in the impedance analysis of Chadwick *et al.* [7], but not reported by other groups irrespective of the synthesis method used. Chadwick and co-workers, who investigated a sample prepared by solid-state synthesis, report on a break just below 273 K with activation energies of 0.18 eV and 0.50 eV [7]. To throw light on the microscopic jump processes in  $\text{BaSnF}_4$ ,  $^{19}\text{F}$  nuclear magnetic resonance (NMR) spin-lattice relaxation [7] as well as high-resolution  $^{19}\text{F}$  (exchange) NMR revealed two dynamically different spin systems.  $^{19}\text{F}$  magic angle spinning (MAS) NMR carried out by Chaudhuri *et al.* points to a temperature dependent occupancy of the Sn-Sn layers by the fluoride ions [19]. Most likely this leads to a change in the transport mechanism probed above room temperature and detected also in our study.

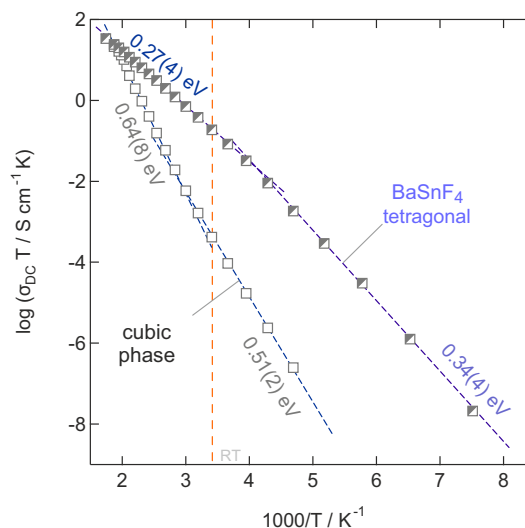


**Figure 4** Arrhenius plot of  $\sigma_{\text{DC}}T$ ; the DC conductivity values were determined from the frequency-independent plateaus of the corresponding isotherms. The dashed lines show Arrhenius fits; the vertical line simply marks room temperature. At around 300 K the DC conductivity is in the order of  $0.7 \text{ mS cm}^{-1}$ .

**4 Conclusion and outlook** Charge carrier transport parameters in layer-structured BaSnF<sub>4</sub>, crystallizing with tetragonal symmetry and prepared via mechanosynthesis with subsequent soft annealing, was investigated by broadband conductivity and permittivity spectroscopy over a large frequency and temperature range exceeding previous studies on this material. Compared to a recent study by Ahmad *et al.* [4] our synthesis route chosen lead to a ternary fluoride with DC conductivities in the order of 0.7 mS cm<sup>-1</sup> at ambient temperature. Most likely, the low annealing temperature used for inducing the phase transformation helped preserve the defect-rich, disordered character of the mechanosynthesized precursor. The latter showed significantly broadened XRD reflections being typical of a nanocrystalline ceramic. Structural changes were followed by DSC and preliminary *in situ* XRD measurements.

The transport properties of the samples prepared is governed by very low activation energies of ca. 0.27 eV above and approximately 0.34 eV below room temperature. We anticipate that the change observed in conduction mechanism is related to the two different reservoirs of mobile F anions in BaSnF<sub>4</sub>, see Refs. [7, 19], as well as to the related fact that F anion site occupation, and thus mobile charge carrier density, changes with temperature as it has been reported by Grey and co-workers [19].

Finally, to our opinion, the large increase in permittivity at low frequencies and sufficiently high temperatures simply reflects interface electrode effects rather than intrinsic dielectric properties [4] of the material. This is shown by the fact that permittivities in the so-called EP region strongly depend on the different electrodes applied.

**Acknowledgements** We thank B. Bitschnau from TU Graz for the XRD measurements and O. Fruhwirth for the DSC results. Financial support by the Deutsche Forschungsgemeinschaft (DFG), Priority Programme SPP 1415, *Crystalline Non-equilibrium Phases* is greatly appreciated. Furthermore, we thank the DFG for access to the impedance spectrometer of the DFG Research Unit 1277, grant no. WI3600/2-1.

## References

- [1] J. Schoonman, *J. Electrochem. Soc.* **123**, 1772 (1976).
- [2] G. J. Schoonman, K. E. D. Wapenaar, G. Oversluizen, and G. J. Dirksen, *J. Electrochem. Soc.* **126**, 709 (1979).
- [3] M. Anji Reddy and M. Fichtner, *J. Mater. Chem.* **21**, 17059 (2011).
- [4] M. M. Ahmad, Y. Yamane, and K. Yamada, *J. Appl. Phys.* **106**, 074106 (2009).
- [5] G. Denes, T. Birchall, M. Sayer, and M. Bell, *Solid State Ion.* **13**, 213 (1984).
- [6] L. N. Patro and K. Hariharan, *Mater. Res. Bull.* **46**, 732 (2011).
- [7] A. V. Chadwick, E. S. Hammam, D. Van der Putten, J. H. Strange, *Cryst. Latt. Def. Amorph. Mater.* **15**, 303 (1987).
- [8] V. Šepelák, A. Düvel, M. Wilkening, K. D. Becker and P. Heitjans, *Chem. Soc. Rev.* **42**, 7507 (2013).
- [9] P. Heitjans, M. Masoud, A. Feldhoff and M. Wilkening, *Faraday Discuss.* **134**, 67 (2007).
- [10] M. Wilkening, V. Epp, A. Feldhoff and P. Heitjans, *J. Phys. Chem. C* **112**, 9291 (2008).
- [11] P. Heitjans and S. Indris, *J. Phys.: Condens. Matter* **15**, R1257 (2003).
- [12] L. N. Patro and K. Hariharan, *Solid State Ion.* **239**, 41 (2013).
- [13] S. Emmert, M. Wolf, R. Gulich, S. Krohns, S. Kastner, P. Lunkenheimer, and A. Loidl, *Eur. Phys. J.* **83**, 157 (2011).
- [14] P. Hagenmuller, J.-M. Réau, C. Lucat, S. Matar, and G. Villeneuve, *Solid State Ion.* **3-4**, 341 (1981).
- [15] N. I. Sorokin, *Inorg. Mater.* **40**, 989 (2004).
- [16] D. Sidebottom, B. Roling, and K. Funke, *Phys. Rev. B* **63**, 024301 (2000).
- [17] J. T. S. Irvine, D. C. Sinclair, and A. R. West, *Adv. Mater.* **2**, 132 (1990).
- [18] P. Lunkenheimer, V. Bobnar, A. V. Pronin, A. I. Ritus, A. A. Volkov, and A. Loidl, *Phys. Rev. B* **66**, 05210 (2002).
- [19] S. Chaudhuri, F. Wang, and C. P. Grey, *J. Am. Chem. Soc.* **124**, 11746 (2002).



## 5.2 F-ion conducting solid solution $\text{Ba}_{0.6}\text{La}_{0.4}\text{F}_{2.4}$

Cubic fluorides such as  $\text{BaF}_2$ ,  $\text{CaF}_2$  or  $\text{PbF}_2$  were found to be capable of hosting excessive F-ions in the crystal lattice if they are doped with trivalent cations. A summary of the findings for various diffraction studies is found in the review on superconductors from S. Hull.<sup>86</sup> Figure 24a) illustrates the additional sites F1 and F2 for interstitials of  $\text{YF}_3$ -doped  $\text{CaF}_2$ . A similar approach was chosen within this work using  $\text{BaF}_2$  that was doped with  $\text{LaF}_3$  (as 40% of the  $\text{BaF}_2$  were replaced by  $\text{LaF}_3$ , it is thus more accurate to speak of *substitution* than of doping).  $\text{BaF}_2$  forms solid solutions with  $\text{LaF}_3$  in almost any molar ratio.<sup>74</sup> Depending on this ratio, the solid solutions crystallize in the cubic  $\text{BaF}_2$  structure or the tysonite structure.<sup>74</sup> The highest conductivities for the mechanochemically prepared compounds were found for  $\text{Ba}_{1-x}\text{La}_x\text{F}_{2+x}$  with  $x=0.4$ .<sup>74,87</sup> In Figure 24b), the values found for the solid solution is shown in comparison to coarse grained and ball-milled  $\text{BaF}_2$ . The conductivity was found to be significantly higher than for the pure compound.

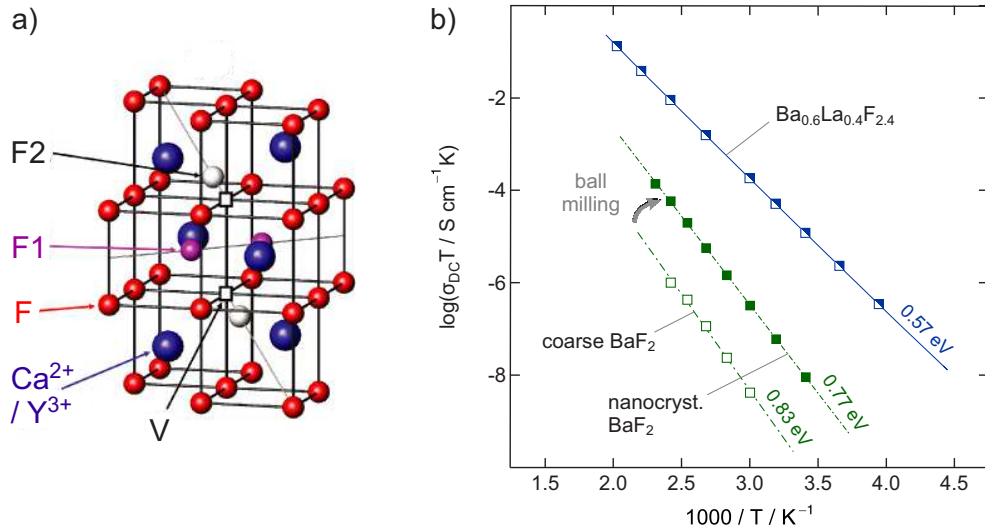


**Figure 24** — a) Illustration of the crystal structure of cubic  $\text{CaF}_2$  showing possible site for interstitials and vacancies upon doping with  $\text{YF}_3$ . Reprinted from ref. 86. b) Arrhenius plot from the conductivities of coarse and ball milled  $\text{BaF}_2$  and the solid solution  $\text{Ba}_{0.6}\text{La}_{0.4}\text{F}_{2.4}$  that shows the increase of more than two orders of magnitude upon doping.

To get detailed insights into the diffusion characteristics of this type of solid solutions, several solid state NMR relaxation spectroscopy techniques were applied in conjunction with (high-frequency) broadband impedance spectroscopy. The impedance measurements up to 3 GHz provided insights into the local hopping dynamics of the solids that could be compared with the findings from solid state NMR. With  $T_{1\rho}$ -measurements in particular, a broad maximum in the relaxation rate was found that points to a range of hopping mechanisms that occur on a similar time scale, see below for detailed explanations.



---

P2: (pp. 57-67)

**Correlated fluorine diffusion and ionic conduction in the nanocrystalline**

**F<sup>-</sup> solid electrolyte Ba<sub>0.6</sub>La<sub>0.4</sub>F<sub>2.4</sub> —**

**<sup>19</sup>F T<sub>1(ρ)</sub> NMR relaxation vs. conductivity measurements**

F. Preishuber-Pflügl, P. Bottke, V. Pregartner, B. Bitschnau, and M. Wilkening,

*Phys. Chem. Chem. Phys.*, 2014, **16**, 9580.



# Correlated fluorine diffusion and ionic conduction in the nanocrystalline $F^-$ solid electrolyte $Ba_{0.6}La_{0.4}F_{2.4}$ — $^{19}F$ $T_{1(\rho)}$ NMR relaxation vs. conductivity measurements

Cite this: *Phys. Chem. Chem. Phys.*, 2014, 16, 9580

F. Preishuber-Pflügl,<sup>\*ab</sup> P. Bottke,<sup>a</sup> V. Pregartner,<sup>a</sup> B. Bitschnau<sup>c</sup> and M. Wilkening<sup>\*ab</sup>

Chemical reactions induced by mechanical treatment may give access to new compounds whose properties are governed by chemical metastability, defects introduced and the size effects present. Their interplay may lead to nanocrystalline ceramics with enhanced transport properties being useful to act as solid electrolytes. Here, the introduction of large amounts of La into the cubic structure of  $BaF_2$  served as such an example. The ion transport properties in terms of dc-conductivity values of the  $F^-$  anion conductor  $Ba_{1-x}La_xF_{2+x}$  (here with  $x = 0.4$ ) considerably exceed those of pure, nanocrystalline  $BaF_2$ . So far, there is only little knowledge about activation energies and jump rates of the elementary hopping processes. Here, we took advantage of both impedance spectroscopy and  $^{19}F$  NMR relaxometry to get to the bottom of ion jump diffusion proceeding on short-range and long-range length scales in  $Ba_{0.6}La_{0.4}F_{2.4}$ . While macroscopic transport is governed by an activation energy of 0.55 to 0.59 eV, the elementary steps of hopping seen by NMR are characterised by much smaller activation energies. Fortunately, we were able to deduce an  $F^-$  self-diffusion coefficient by the application of spin-locking NMR relaxometry.

Received 28th January 2014,  
Accepted 26th March 2014

DOI: 10.1039/c4cp00422a

www.rsc.org/pccp

## 1. Introduction

Studying ion dynamics in solids is one of the most vital topics in modern solid-state chemistry.<sup>1–3</sup> The development of advanced sensors or energy storage systems requires careful examining of the correlation of ion transport over long distances and local ion hopping between neighbouring sites within a rigid lattice structure. Such studies are directly linked with the development of advanced solid electrolytes,<sup>1–5</sup> urgently needed for future all-solid-state rechargeable batteries.

In particular, highly conducting and electrochemically stable fluorides<sup>5–9</sup> are necessary components to bring all-solid-state fluorine-ion batteries<sup>8</sup> alive. Regarding particular applications they might serve as alternatives to those relying on lithium<sup>2</sup> and sodium<sup>4</sup> as ionic charge carriers. Quite recently, solid solutions of nanocrystalline fluorite-type  $Ba_{1-x}La_xF_{2+x}$  prepared by high-energy ball milling have been introduced as a promising solid  $F^-$  electrolyte.<sup>9</sup> First measurements of its electrochemical stability<sup>10</sup> encouraged us to study F dynamics in detail. As presented by

Fichtner and co-workers,<sup>9</sup> ionic transport properties of a series of mechanochemically synthesized nanocrystalline samples with  $x$  ranging from  $x = 0$  to  $x = 0.55$  have been studied by impedance spectroscopy recently, and the data have been analysed with respect to macroscopic ion transport. Overall conductivity is anticipated to be fully governed by F anions, *i.e.*, the transference number is assumed to be close to one and, thus, no electronic contributions play a role practically. The highest ion conductivity was found for samples with  $x = 0.3$  and  $x = 0.4$ .<sup>9</sup>

In the present study, we take advantage of  $^{19}F$  nuclear magnetic resonance (NMR) relaxation measurements,<sup>11,12</sup> carried out under static conditions, to collect information on the elementary steps of ion hopping in structurally disordered  $Ba_{0.6}La_{0.4}F_{2.4}$ . NMR can be a powerful tool and has extensive applications in the field of fast (nanocrystalline) ion conductors, in particular.<sup>13–22</sup> It is worth noting that nanocrystalline  $Ba_{1-x}La_xF_{2+x}$  is not stable in its nanostructured form at high temperatures; this restricts the temperature range, and thus also the number of available methods to probe diffusion parameters from an atomic scale point of view. NMR, however, offers quite a large set of techniques that are sensitive to both slow and fast (translational) ion dynamics. Here, with the use of SLR measurements, carried out in both (i) the rotating frame and (ii) the laboratory frame of reference,<sup>11,23,24</sup> F dynamics with jump rates ranging from the kHz to the MHz range can be probed. Their combination gives access to a quite large dynamic window.<sup>25</sup> Spin-spin relaxation

<sup>a</sup> Institute for Chemistry and Technology of Materials, and Christian Doppler Laboratory for Lithium Batteries, Graz University of Technology, Stremayrgasse 9, 8010 Graz, Austria. E-mail: preishuber-pfluegl@tugraz.at

<sup>b</sup> DFG Priority Program (SPP) 1415, Graz University of Technology, Stremayrgasse 9, 8010 Graz, Austria. E-mail: wilkening@tugraz.at

<sup>c</sup> Institute of Physical and Theoretical Chemistry, Graz University of Technology, Stremayrgasse 9, 8010 Graz, Austria

measurements<sup>20</sup> and line shape studies,<sup>26</sup> which do probe even slower F motions, complement the set of time-domain resonance techniques applied.

Considering fast ion conductors with a large number fraction of highly mobile ions, correlation effects<sup>27–30</sup> are expected to influence the movement of the charge carriers. Besides the possibility of quantifying F anion dynamics, as has been excellently presented by Chadwick and Strange,<sup>31</sup> NMR is also highly useful in distinguishing correlated from independent hopping.<sup>18,26,32–35</sup> In conjunction with conductivity spectroscopy,<sup>28,36,37</sup> complementary information of translational ion dynamics can be collected. Therefore, the present investigation is also aimed at contributing to the question<sup>32,33,38</sup> how results from various time domain NMR methods, *viz.* F migration activation energies and jump rates compare with those obtained from ac impedance spectroscopy, *i.e.*, probed on different length- and time scales. For this reason, impedance data have also been recorded over the whole temperature range covered by NMR, *i.e.*, including also temperatures well below ambient. In particular, the study presents impedance data recorded at frequencies as high as 3 GHz.

One major advantage of NMR is that it can often provide a direct estimate of the  $F^-$  jump rate<sup>25,32</sup> provided diffusion-induced contributions can be well separated from those being largely affected by so-called background relaxation. In the present case, with the spin-lock NMR technique, see, *e.g.*, ref. 39, it was indeed possible to record a diffusion-induced rate peak from which the self-diffusion coefficient  $D$  could be deduced. Our estimation uses the relaxation model of Bloembergen, Purcell and Pound<sup>40</sup> which was developed for three-dimensional (isotropic) motions of spin-1/2 nuclei moving in an uncorrelated manner. Finally, the NMR self-diffusion coefficient can be compared with solid-state diffusion coefficients extracted *via* the Nernst–Einstein equation from dc conductivity data.

## II. Experiment

The  $Ba_{1-x}La_xF_{2+x}$  sample with  $x = 0.4$  has been prepared by high-energy ball milling<sup>41–46</sup> making use of a planetary mill (Fritsch, Pulverisette 7). The starting materials, powders of  $BaF_2$  and  $LaF_3$  with  $\mu\text{m}$ -sized crystallites, were purchased with high purity (99.99%) from Alfa Aesar and Sigma Aldrich, respectively. To synthesize several g of  $Ba_{0.6}La_{0.4}F_{2.4}$ , the binary fluorides were mixed under an Ar atmosphere according to the stoichiometric ratio needed. We used a beaker made of  $ZrO_2$  (Fritsch) or tungsten carbide (Fritsch) equipped with 180 or 140 balls (5 mm in diameter) of the same material to treat the mixtures at 600 rpm under dry conditions. The ball-to-powder ratio was 17 : 1. We carefully avoided any contact with moisture; thus, the beakers were airtight filled with  $BaF_2$ : $LaF_3$  in a glove box with dry Ar atmosphere. Later on, *i.e.*, after milling periods ranging from 6 h to 10 h, they were also opened in the glove box.

Structural analysis of the prepared nanocrystalline powders was carried out using X-ray powder diffraction (XRPD) and magic angle spinning (MAS) NMR spectroscopy. The powder diffraction patterns, shown in Fig. 1, were recorded on a Bruker D8

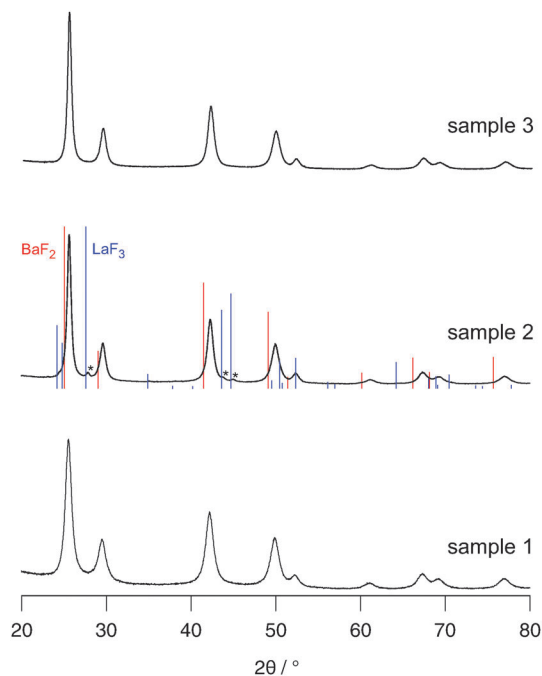


Fig. 1 X-ray powder diffractograms of the samples  $Ba_{0.6}La_{0.4}F_{2.4}$  prepared for this study. For the synthesis of sample 1, a tungsten carbide vial set was used and the milling time was 6 h. Sample 2 was prepared with a  $ZrO_2$  vial set and the mixture was treated for 6 h. Reflexes of residual  $LaF_3$  are marked by asterisks. Sample 3 was also prepared using a  $ZrO_2$  vial, but the milling time was increased to 10 h. As in the case of sample 1, no residual  $BaF_2$  and  $LaF_3$  are left.

Advance diffractometer with Bragg Brentano geometry using  $Cu K_\alpha$  radiation ( $10\text{--}100^\circ 2\theta$ , step size  $0.02^\circ 2\theta$ , step time 1 s). Rietveld refinement was carried out with X-PertHighScorePlus (PANalytical).  $^{19}F$  MAS NMR experiments were recorded on a Bruker Avance III spectrometer operating at 470.5 MHz. We used a 2.5 mm-MAS probe (Bruker) with the ability to reach a spinning frequency of 30 kHz; spectra were recorded by non-selective excitation using a short pulse with a length of approximately 1.6  $\mu\text{s}$ .

To prepare dense pellets for impedance measurements the powder samples were cold-pressed by applying an uniaxial pressure of 0.13 GPa. Our press sets allow the fabrication of pellets with, *e.g.*, diameters of 5 mm, 8 mm and 10 mm (sample 3, see below). Pt electrodes (*ca.* 100 nm in thickness) were applied using a sputter coater (Leica). The thicknesses of the pellet pressed were measured with appropriate gauges. The impedance measurements were carried out using a Novocontrol Concept 80 broadband analyser (Alpha-AN, Novocontrol) being connected to a BDS 1200 cell in combination with an active ZGS cell interface (Novocontrol) allowing temperature-variable 2-electrode (dielectric) measurements. The temperature is automatically controlled by means of a QUATRO cryosystem (Novocontrol) making use of a heating element which builds up a specified pressure in a liquid nitrogen dewar in order to create a highly constant  $N_2$  gas flow. After being heated by a gas jet, the freshly evaporated  $N_2$  flows directly through the sample cell that is mounted in a cryostat. This setup allows very stable system

operation with an accuracy of  $\pm 0.01$  °C. In summary, the whole setup is able to record the complex impedance ( $\hat{Z}$ ) and the permittivity ( $\hat{\epsilon}$ ) at frequencies ranging from few  $\mu\text{Hz}$  up to 20 MHz (110–570 K). For impedance measurements up to 3 GHz we used an Agilent E4991 A high-frequency analyser connected to a high frequency cell (Novocontrol).

For the NMR measurements the fluoride was sealed in glass ampoules, *ca.* 4 cm in length and 5 mm in diameter, to protect the nano-crystalline samples with their large surface area permanently from any influence of humidity. NMR lines and relaxation rates were measured using an Avance III spectrometer connected to a shimmed cryomagnet with nominal magnetic fields of 7 T. This field corresponds to a  $^{19}\text{F}$  Larmor frequency of  $\omega_0/2\pi = 282$  MHz. We used a home-built (high-temperature) NMR probe capable of recording NMR signals under static, *i.e.*, non-rotating conditions up to temperatures as high as 550 K. The  $\pi/2$  pulse length was approximately 1  $\mu\text{s}$  at 200 W. A Eurotherm temperature controller in combination with a type *T* thermocouple was used to control and monitor the temperature in the probe's sample chamber.

$^{19}\text{F}$  NMR spin-lattice relaxation (SLR) rates  $1/T_1$  were acquired with the saturation recovery pulse sequence  $10 \times \pi/2 - t_d - \pi/2 - \text{acq.}$ <sup>47,48</sup> The pulse sequence works as follows: an initial pulse train, consisting of ten  $\pi/2$  pulses separated by 40  $\mu\text{s}$ , was used to destroy any longitudinal magnetization  $M_z$  prior to recording its temperature-dependent recovery as a function of the delay time  $t_d$ . Rotating-frame  $^{19}\text{F}$  NMR SLRQ rates  $1/T_{1Q}$  were recorded with the spin-lock technique,  $\pi/2 p(t_{\text{lock}}) - \text{acq.}$ <sup>39,47,49–53</sup> With our probe we were able to make use of a locking frequency  $\omega_1$  of approximately 62.5 kHz. The corresponding locking pulse  $t_{\text{lock}}$  was varied from 40  $\mu\text{s}$  to 400 ms. Note that the recycle delay for the SLRQ experiments was set to at least  $5 \times T_1$  in order to guarantee full longitudinal relaxation between each scan.  $1/T_{1(2)}$  and  $1/T_{1Q}$  rates were obtained by parameterizing the magnetic transients  $M_z(t_d)$  and  $M_Q(t_{\text{lock}})$ , respectively, by stretched exponentials:  $M_z(t_d) \propto 1 - \exp(-(t/T_1)^\gamma)$  and  $M_Q(t_{\text{lock}}) \propto \exp(-(t_{\text{lock}}/T_{1Q})^\gamma)$ , respectively (*cf.* Fig. 2).

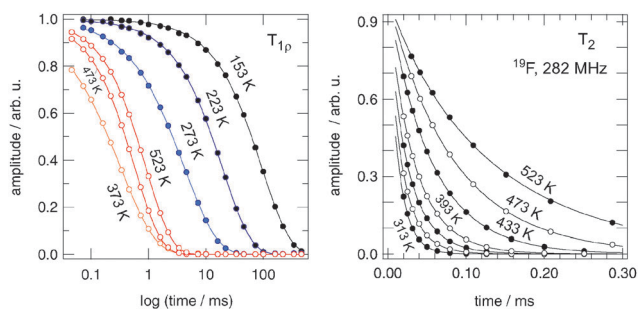


**Fig. 2** Left:  $^{19}\text{F}$  NMR transversal decay of the spin-locked magnetization recorded at the various temperatures indicated. The locking frequency was 62.5 kHz. Note the logarithmic scale of the x-axis. Solid lines represent fits according to stretched exponentials yielding  $T_{1p}^{-1}$  and  $\gamma_{1p}$ . Right:  $^{19}\text{F}$  NMR spin-spin relaxation transients. From the fits (stretched exponentials, solid lines) the rates  $T_2^{-1}$  and stretching factors  $\gamma_2$  shown in the upper part of the Arrhenius plot of Fig. 3 can be obtained. The corresponding  $T_1$ -transients do almost follow an exponential time behaviour.

In addition, temperature-variable  $^{19}\text{F}$  NMR spin-spin relaxation (SSR) rates  $1/T_2$  were recorded by taking advantage of a (two-pulse) solid-echo pulse sequence:<sup>47</sup>  $\pi/2 - t_{\text{echo}} - \pi/2 - \text{acq.}$   $t_{\text{echo}}$  denotes the variable interpulse delay. The transients obtained were fitted with stretched exponentials. Static  $^{19}\text{F}$  NMR spectra were either obtained after Fourier transformation (FT) of the free induction decay, which were recorded by non-selective irradiation with a single  $\pi/2$  pulse, or by FT of the solid echo beginning from the top of the signal.

### III. Results and discussion

#### A. Characterization by X-ray diffraction

Phase purity of the mechanochemical preparation of nanocrystalline  $\text{Ba}_{0.6}\text{La}_{0.4}\text{F}_{2.4}$  was checked by powder X-ray diffraction carried out at room temperature and in air atmosphere. In Fig. 1 the diffractograms of several samples, which have been differently prepared, are shown. While sample 1, which was prepared in a tungsten carbide (WC) vial ( $t_{\text{mill}} = 6$  h), does not reveal any binary fluorides left, sample 2, which was synthesized under slightly different milling conditions ( $\text{ZrO}_2$  vial,  $t_{\text{mill}} = 6$  h), shows residual  $\text{LaF}_3$ . According to Rietveld refinement, phase pure  $\text{Ba}_{0.6}\text{La}_{0.4}\text{F}_{2.4}$  is formed in the  $\text{ZrO}_2$  beaker, when the milling time  $t_{\text{mill}}$  to prepare the ternary fluoride is increased from 6 h to 10 h (sample 3). The vertical bars in Fig. 1 represent positions and intensities of the reflexes of the two starting materials. The systematic shift of the diffraction angle  $2\theta$  towards larger values points to lattice contraction due to the incorporation of the smaller La ions into the fluorite structure of  $\text{BaF}_2$ .<sup>9</sup>

From the broadening of the reflexes we estimated an average crystallite size of approximately 10 nm (Scherrer equation). Such a value is typically found for mechano-synthesized ceramics treated in high-energy ball mills. The X-ray powder patterns show a low and straight-line background and, therefore, no indications for notable amounts of the amorphous material present. Sample 1 has been used for  $^{19}\text{F}$  NMR and impedance measurements up to 20 MHz. From sample 3 a larger pellet with a diameter of 10 mm was pressed for high-frequency impedance measurements carried out up to 3 GHz.

#### B. NMR measurements

Compared to the recently published study of Rongeat *et al.*,<sup>9</sup> which mainly focusses on the investigation of F ion transport in  $\text{Ba}_{1-x}\text{La}_x\text{F}_{2+x}$  by impedance spectroscopy, we emphasized on static  $^{19}\text{F}$  NMR relaxometry to point out the differences between short- and long-range F diffusivity. To that end, the present study centres upon a single mechano-synthesized sample with  $x = 0.4$  which is the composition leading to the highest conductivity observed.<sup>9</sup> In the Arrhenius plot of Fig. 3(a) an overview of the NMR relaxation rates measured is shown. The figure presents the temperature-dependent relaxation rates  $1/T_1$ ,  $1/T_{1p}$ , and  $1/T_2$  together with the stretching exponents  $\gamma_i$  ( $i = 1, 1p, 2$ ) obtained by parameterizing the underlying magnetization transients (see Fig. 2) with appropriate fitting

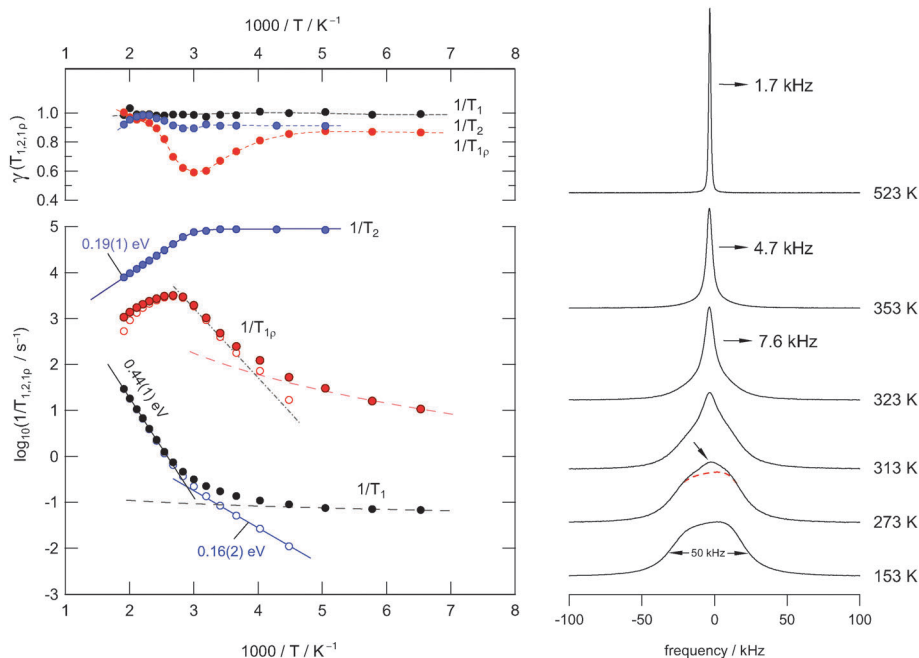


Fig. 3 Left: temperature dependence of the  $^{19}\text{F}$  NMR relaxation rates of nanocrystalline  $\text{Ba}_{0.6}\text{La}_{0.4}\text{F}_{2.4}$  (sample 1) prepared by mechano-synthesis at ambient temperature. The Larmor frequency was 282 MHz. The upper graph shows the dependence of the stretching exponents  $\gamma$  on  $T$ . Right:  $^{19}\text{F}$  NMR line shapes recorded under static conditions at the temperatures  $T$  indicated.

functions;<sup>34</sup> in our case stretched exponentials were used (see above). For comparison, on the right-hand side of Fig. 3 a couple of temperature-variable  $^{19}\text{F}$  NMR spectra of mechano-synthesized  $\text{Ba}_{0.6}\text{La}_{0.4}\text{F}_{2.4}$  are shown.

Starting the discussion with the  $^{19}\text{F}$  NMR spectra, which were recorded under non-rotating conditions, it is evident that at the lowest temperature, being accessible with the probe used here, the overall NMR signal is composed of several components. Owing to both structural disorder and cation mixing introduced during milling, the shape of the low- $T$  spectrum likely reveals a superposition of many NMR intensities that reflect magnetically different F species. These species result from a broad distribution of locally distinct environments. For comparison, it is known for pure nanocrystalline  $\text{BaF}_2$ , even if severely treated in shaker or planetary mills, that the corresponding  $^{19}\text{F}$  NMR signal is much less broadened than it is found in the present case.<sup>43</sup>

Here, the overall shape of the NMR spectra recorded at low  $T$  results from the mixing effect of Ba and La ions; this alters the  $^{19}\text{F}$  chemical shifts. Similarly, this has also been reported by Fichtner and co-workers using magic angle spinning (MAS)  $^{19}\text{F}$  NMR on samples with varying La-content.<sup>9</sup> For comparison, in cation-mixed mechano-synthesized  $(\text{Ba,Ca})\text{F}_2$ , as well as in mixed fluorides with Sr and Ca ions, the individual F environments could be well resolved due to relatively sharp resonance lines and the application of high-speed MAS NMR.<sup>44</sup>

As it becomes obvious from Fig. 3(b), with increasing temperature a narrowed NMR line emerges which is due to both averaging of dipole-dipole<sup>26</sup> and local chemical shift interactions of the various magnetically inequivalent F ions. At sufficiently high temperatures the mean exchange rate

becomes much faster than the spectral width of the NMR line. This slows down spin-spin relaxation and leads to a single NMR line being fully narrowed by motional averaging; see the spectrum recorded at 523 K, which is the upper temperature we used for our study. Compared to the initial situation, the line width (full width at half maximum) has been decreased from *ca.* 50 kHz down to 1.7 kHz; in the regime of *extreme averaging* it is mainly governed by inhomogeneities of the external magnetic field. From motional averaging it is evident that the jump rate  $\tau^{-1}$  (523 K) is much larger than  $50 \text{ kHz} \times 2\pi$ , *i.e.*, the rate should be in the order of  $10^5 \text{ s}^{-1}$  to  $10^6 \text{ s}^{-1}$ .

In Fig. 4 selected  $^{19}\text{F}$  NMR spectra are shown which were deconvoluted by using a Gaussian and a Lorentzian line (see the solid and dashed lines of the spectra recorded at 323 K and 353 K, respectively). At higher temperatures, *i.e.*, in the regime of full averaging, *viz.* at 523 K, the NMR line can be best represented by a single Voigt profile. In general, such heterogeneous motional narrowing can be linked with a distribution of  $\text{F}^-$  jump rates. Cation mixing<sup>44</sup> and local structural disorder in nanocrystalline  $\text{Ba}_{0.6}\text{La}_{0.4}\text{F}_{2.4}$  prepared by mechanical treatment supports this idea. Thus, the rate estimated above should be regarded as a mean value.

According to a mean jump rate in the order of or even larger than  $10^4 \text{ s}^{-1}$ , the  $^{19}\text{F}$  NMR spin-spin and spin-lattice relaxation rates are expected to be greatly, if not solely, influenced by F self-diffusion. F dynamics lead to fluctuations of the local dipolar fields and induce longitudinal magnetization recovery as well as affect transversal NMR relaxation. Starting the analysis with the laboratory-frame SLR rates, we observe a weaker-than-activated temperature dependence below 225 K (see Fig. 3(a)). In this low- $T$  regime, which is characterised by  $\omega_0\tau_c \ll 1$  where  $\tau_c$  is

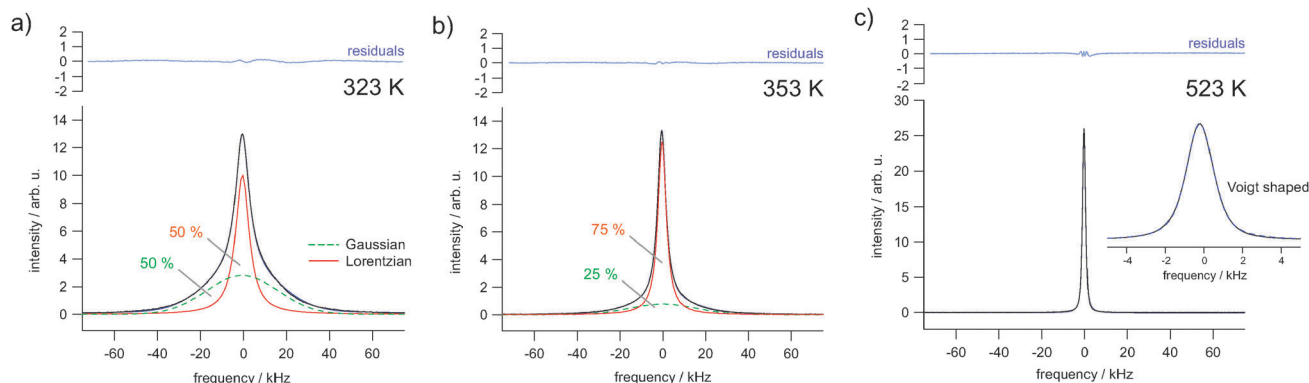


Fig. 4 Selected  $^{19}\text{F}$  NMR lines to highlight the motional averaging of dipole–dipole interactions and coalescence as well. While a combination of a Gaussian and a Lorentzian is appropriate to represent the lines at moderate temperatures, the final shape in the regime of extreme narrowing resembles that of a Voigt function. The values in percentage terms indicate the area fractions of the two different components.

the motional correlation time,  $T_1^{-1}$  is mainly driven by non-diffusive relaxation sources such as lattice vibrations and coupling of the spins with paramagnetic impurities. With increasing temperature, however, the rate  $T_1^{-1}$  increases; at  $T > 370$  K it has already reached the low- $T$  flank ( $\omega_0\tau_c \ll 1$ ) of the diffusion-induced rate peak, which is expected to show up at higher  $T$ . It should be noted that temperatures well above 550 K are not accessible with the NMR setup available in our laboratory. Moreover, the onset of grain growth may represent a natural limit to investigate F diffusion parameters in nanocrystalline (metastable) fluorides.

In order to carefully separate non-diffusive background relaxation from purely diffusion-induced contributions, we parameterized the low- $T$  rates with an appropriate power law  $T_1 \propto T^\beta$  and extrapolated the rates obtained to higher temperatures (see the dashed line in Fig. 3(a)). Subsequent subtraction from the overall rates measured resulted in background-corrected SLR rates which are represented in Fig. 3 by unfilled symbols. As a result, we observe a stepwise increase in the diffusion-induced  $T_1^{-1}$  rates: starting from low  $T$  an activation energy of  $E_a'' = 0.16$  eV can be deduced, while an Arrhenius fit of the flank showing up at higher temperatures yields  $E_{a,\text{low}} = 0.44$  eV.

The first value nicely agrees with the one obtained from spin–spin-relaxation measurements which are also shown in Fig. 3. In the limit  $T \rightarrow 0$  K, which is the rigid lattice,  $T_2^{-1}$  is approximately given by  $10^5 \text{ s}^{-1} \equiv T_{20}^{-1}$ . The rate  $T_2^{-1}$  starts to deviate from  $T_{20}^{-1}$  at 330 K and then follows an Arrhenius law characterised by an activation energy of only  $E_a' = 0.19$  eV. According to the simple behaviour expected from the relaxation model of Bloembergen, Purcell and Pound (BPP), which had been introduced for 3D (isotropic) uncorrelated motion,<sup>40</sup> one would expect the  $T_2^{-1}$  flank to coincide with the high- $T$  flank ( $\omega_0\tau_c \gg 1$ ) of the  $T_1^{-1}$  rate peak leading to  $E_a' = E_{a,\text{high}}$  with  $E_{a,\text{high}}$  being the activation energy in the regime  $\omega_0\tau_c \gg 1$ . It should be noted that  $E_{a,\text{high}}$  cannot be determined *via*  $T_1^{-1}$  measurements in the present case because of temperature restrictions and limitations in our experimental setup (see above).

The various models developed for correlated motions do predict asymmetric NMR rate peaks.<sup>14,17,30</sup> Indeed, such shapes are observed in general; the corresponding peaks are characterised

by  $E_{a,\text{low}}$  being smaller than  $E_{a,\text{high}}$  and  $E_a' = E_{a,\text{high}}$ , respectively.  $E_{a,\text{high}}$  is often compared with the corresponding value from dc conductivity measurements (see Fig. 5 and the following section).<sup>32</sup> In our case, however, these general characteristics for correlated 3D jump diffusion seem to be not fulfilled and an anomaly is observed as will be outlined in detail in the following.

To shed further light on this situation, we recorded  $^{19}\text{F}$   $T_{1\rho}$  NMR SLR rates in the rotating frame of reference at locking frequencies much smaller than the Larmor frequency used for our  $T_1$  measurements. Compared to NMR relaxometry in the lab frame,  $T_{1\rho}^{-1}$  is *per se* sensitive to F motions taking place on a longer length (and time) scale.<sup>17</sup> As expected, we were able to partly reach the high- $T$  flank of the corresponding  $T_{1\rho}^{-1}(1/T)$  peak; compared to  $T_1^{-1}(1/T)$  it is shifted towards lower  $T$ . The peak itself spans a rather broad  $T$  range; even after appropriate background correction, as it was done for  $T_1$ , the high- $T$  flank cannot be clearly separated. The broadened peak might be the result of superimposing rate peaks reflecting the distribution of migration processes in the disordered  $\text{Ba}_{0.6}\text{La}_{0.4}\text{F}_{2.4}$  phase. Irrespective of its overall shape, the activation energy in the limit  $\omega_1\tau_c \ll 1$  lies in the range 0.25–0.35 eV. The resulting value depends on the quality of the correction procedure applied, *i.e.*, the  $\beta$  chosen, and the number of data points taking into account for the Arrhenius fit. Most importantly, these values are even smaller than  $E_{a,\text{low}}$  deduced from  $T_1^{-1}(1/T)$  in the limit  $\omega_0\tau_c \ll 1$ . This points to a second anomaly observed *via* NMR relaxation. Frequency-dependent conductivity measurements might help understand the complex results found by NMR relaxometry.

### C. Impedance and dielectric measurements

Quite recently, impedance spectra, that is the real part  $\sigma'$  of the complex conductivity ( $\hat{\sigma}$ ) plotted *vs.* frequency  $\nu$ , have been reported by Fichtner and co-workers;<sup>9</sup> conductivity data were discussed in terms of contributions from bulk and grain boundaries of mechano-synthesized  $\text{Ba}_{1-x}\text{La}_x\text{F}_{2+x}$ . To compare our results from NMR, recorded at lower temperatures and resonance frequencies in the kHz and MHz range, the samples have been investigated at temperatures down to 173 K and at

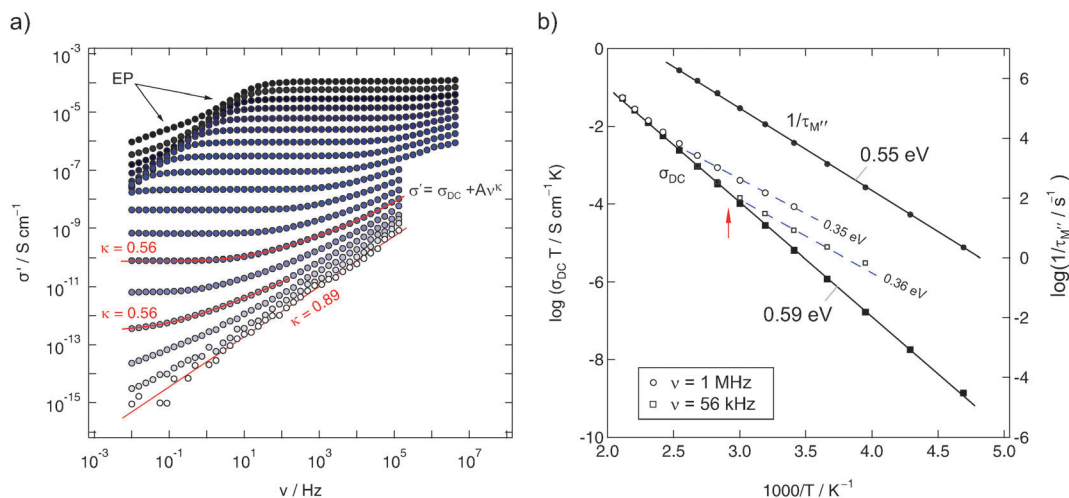


Fig. 5 (a) impedance isotherms of mechano-synthesized  $\text{Ba}_{0.6}\text{La}_{0.4}\text{F}_{2.4}$  (sample 1) recorded at temperatures ranging from 133 K up to 473 K. (b) Arrhenius plot of  $\sigma_{\text{DC}}T$ ; for comparison, the temperature dependencies of  $\sigma' T$ , read out at frequencies  $\nu = 1$  MHz and 56 kHz, respectively, are also shown. Moreover,  $\tau_{\text{M}}^{-1}$ , that is the relaxation rate being determined from modulus spectra  $M''(\nu)$ , is also presented.

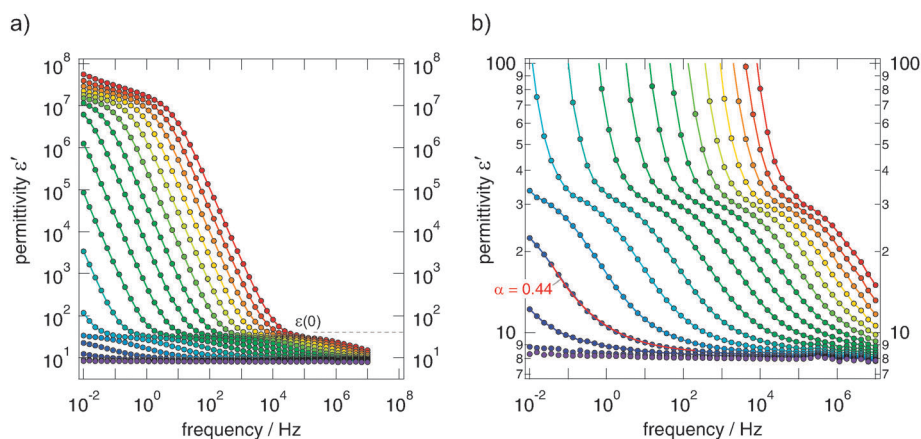


Fig. 6 (a) Real part of the complex permittivity  $\epsilon'$  of nanocrystalline  $\text{Ba}_{0.6}\text{La}_{0.4}\text{F}_{2.4}$  (sample 1) as a function of frequency  $\nu$ . (b) Magnification of the spectra shown left in order to estimate  $\epsilon(0)$ . The bulk process can be mirrored with a power law of the form  $\epsilon'(\nu) = \epsilon(\infty) + A_{\nu}\nu^{-p}$  with  $p \approx f(t) \approx 0.44$ .

frequencies as high as 3 GHz. In Fig. 5–7 selected conductivity as well as permittivity spectra are shown.

The isotherms (sample 1) shown in Fig. 5(a) reveal the typical characteristics of impedance spectra of structurally disordered materials usually showing a distribution of jump rates and activation energies. If not perturbed by electrode polarisation (EP) effects, dominating impedance response at high temperatures and low frequencies, the spectra are composed of a dc-plateau and a Jonscher-type dispersive region, which can be approximated with a power law according to  $\sigma' = \sigma_{\text{DC}} + A_{\nu}\nu^{\kappa}$ . As has been shown by many previous studies on other ion conductors, the exponent  $\kappa$  takes values ranging from 0.5 to 0.8. In our case we found  $\kappa = 0.56$  almost independent of  $T$ .  $\kappa \neq f(T)$  means that the isotherms have the same shape and can be collapsed into a single so-called master curve after appropriate scaling has been carried out. This behaviour indicates that impedance spectroscopy, when carried out at different temperatures ( $>193$  K) and frequencies with

values as high as 1 MHz, is sensitive to the same motional process in  $\text{Ba}_{0.6}\text{La}_{0.4}\text{F}_{2.4}$ .

At the lowest temperatures, that is, at temperatures lower than 173 K, the dc-plateau has been mainly shifted towards lower frequencies and a  $\nu^{0.89}$ -dependence shows up. The increase of  $\kappa$  towards larger values might be related to the presence of strictly localized F motions governing the isotherms at sufficiently low  $T$ .  $\kappa$  being close to 1 would correspond to the (nearly) constant loss (NCL) phenomenon which is frequently related to such caged dynamics, see, e.g., ref. 28 for a brief overview on this topic.

In order to quantify thermal activation of long-range F transport, DC conductivity values ( $\sigma_{\text{DC}}T$ ) have been plotted in Fig. 5(b) vs.  $1000/T$ . The solid line represents a linear fit and yields an activation energy  $E_{\text{a,dc}}$  of 0.59 eV. This result is in very good agreement with the value found by Rongeat *et al.*<sup>9</sup> (0.58 eV) and with those reported for  $\text{F}^{-}$  ion transport in single crystals.<sup>54–56</sup> Moreover, it is comparable with the activation energy when electrical relaxation times  $\tau_{\text{M}}$  are analysed, which

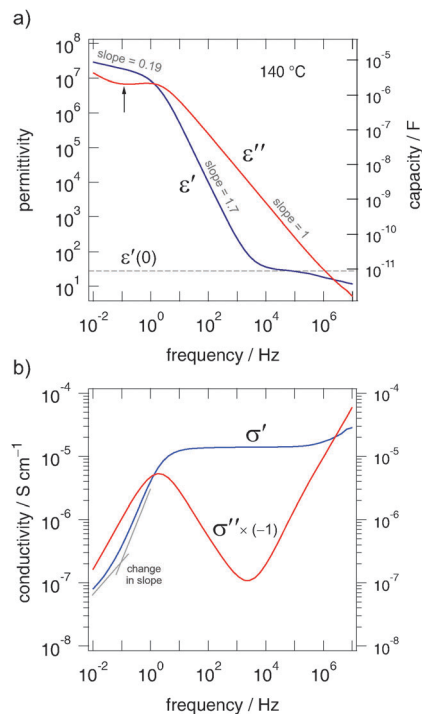


**Fig. 7** (a) The frequency dependence of  $\epsilon'$  and  $\epsilon''$  recorded at 413 K. (b) Frequency dependence of  $\sigma'$  and  $(-1)\cdot\sigma''$  recorded at 413 K. According to the Kramers–Kronig relation and  $\hat{\sigma}(\omega) = i\omega\epsilon_0\hat{\epsilon}(\omega)$  (here, we have  $\omega/2\pi = \nu$ ,  $i^2 = -1$  and  $\epsilon_0$  being the permeability under vacuum) the plateau  $\sigma' \propto A_\sigma\nu^0$  corresponds to  $\epsilon'' \propto A_\epsilon\nu^{-1}$ . The local minimum of  $\epsilon''$  (see arrow) is expressed as a change in slope in the EP region of  $\sigma'$ , see also Fig. 5. The slopes given for  $\epsilon'$  indicate electrode polarisation.

can be deduced from modulus peaks  $M''(\nu)$ . These are less sensitive to an electrical response determined by large capacities such as the response from grain boundaries. Hence, we may assume that  $\sigma_{\text{DC}}$  mainly reflects the bulk response and that grain boundaries seem to play a less prominent role in blocking long-range transport. As has been pointed out by Rongeat *et al.*,<sup>9</sup> the activation energy obtained from  $\sigma_{\text{DC}}T$  vs.  $1/T$  mainly reflects the migration enthalpy rather than contributions from forming F vacancies. The authors already have pointed out that activation energies ranging from 0.5 to 0.6 eV would correspond to those being characteristic for vacancy migration in microcrystalline  $\text{BaF}_2$  (and its single crystals).<sup>31,57</sup> In a structurally disordered material, particularly when prepared by mechanical treatment, also other point defects such as F interstitials have to be considered – especially in the case of La-doped  $\text{BaF}_2$ . In such a case, specifying a primary point defect, if there is any, is very difficult. Most likely, the situation has to be described by a complex interplay of different kinds of defects, including not only point defects.

To judge which capacities and permittivities are associated with the impedance spectra and dc-plateaus obtained, we plotted  $\epsilon'$  as a function of  $\nu$  (see Fig. 6). Starting with  $\epsilon'(\infty) \approx 8$  at low temperatures and high frequencies, at intermediate temperatures a plateau is reached indicating that  $\epsilon'(0)$  is approximately 35 (see the magnification in Fig. 6(b)). The corresponding capacity takes a value of approximately 9 pF (Fig. 7). In our opinion these values corroborate the anticipation

that  $\sigma_{\text{DC}}$  is predominantly determined by the bulk response. The further increase of  $\epsilon'$  observed is due to polarisation effects of the ion blocking electrodes applied. In Fig. 7 the real and imaginary parts of  $\hat{\sigma}$  and  $\hat{\epsilon}$  are compared. The curves reveal the well-known features of impedance spectroscopy and show an almost ‘ideal’ frequency dependence that is expected for a non-Debye impedance response. This is also expressed as follows. If  $\epsilon'$  is given by  $\epsilon'(\nu) = \epsilon'(\infty) + A_\epsilon\nu^{-p}$  an AC storage-to-loss ratio of one is obtained if  $p + \kappa = 1$ . Indeed, our data fulfill this relation; we have  $\kappa = 0.56$  and  $p = 0.44$  (see Fig. 6(b)).

At this stage let us start comparing the results from impedance spectroscopy with those from NMR relaxometry. Even if  $E_{\text{a,dc}}$  represents bulk properties, it cannot be expected to fully match  $E_{\text{a,low}}$  from NMR. The two methods are sensitive to anion motions taking place on quite different time scales and they have to be described by distinct motional correlation functions. If at all,  $E_{\text{a,dc}}$  is expected to coincide with  $E_{\text{a,high}}$ ,<sup>17</sup> the latter is *per se* sensitive to long-range ion motion at least. In contrast to  $E_{\text{a,high}}$ , the low- $T$  flank of a given  $T_1^{-1}$  rate peak is affected by correlation effects such as structural disorder and Coulomb interactions.<sup>27,29</sup> Such interactions lead to the aforementioned asymmetry of an NMR rate peak.

If we, however, readout conductivities at higher frequencies instead of determining dc-values at  $\nu \rightarrow 0$ , lower activation energies should result.<sup>26,32</sup> Indeed, this is the case when the Arrhenius plot of Fig. 5 is considered. The unfilled symbols represent  $\sigma'T$  measured at 56 kHz and 1 MHz. Although, as expected, the values coincide with  $\sigma_{\text{DC}}T$  at sufficiently high temperatures, the deviations at lower  $T$  hint to smaller activation energies being responsible for anion hopping if shorter length scales are regarded. Typically,  $E_{\text{a,ac}} = 0.35$  eV is obtained here, that is, however, smaller than  $E_{\text{a,low}}$  from  $^{19}\text{F}$  NMR. Instead, good agreement has been found between  $E_{\text{a,low}}$  and  $E_{\text{a,ac}}$  in the case of nanocrystalline  $\text{LiTaO}_3$  analysed in a similar manner. Such an agreement is proposed by the coupling concept introduced by Ngai<sup>32</sup> and has been documented for a number of ion dynamics in glassy systems, in particular.

Although  $E_{\text{a,ac}}$ , irrespective of being determined at 56 kHz or 1 MHz, might be interpreted as an activation energy that is comparable with that of the low- $T$  flank of the  $T_{1\rho}^{-1}$ -peak, the discrepancy between  $E_{\text{a,ac}} = 0.35$  eV and  $E_{\text{a,low}} = 0.44$  eV is apparent. To answer the question whether this changes the frequency regime that is identical with the Larmor frequency of 282 MHz, we performed conductivity measurements up to the GHz range. In Fig. 8 some of the impedance data of sample 3 are shown. The conductivities recorded span a dynamic range of eleven decades. The data points recorded in the GHz regime perfectly match those collected with the Alpha-analyser working up to 20 MHz. As a side note, the high-frequency data reveal a change in the slope of the isotherms recorded at low temperatures. This might be an indication of a high-frequency plateau increasingly affecting conductivity data.

At high temperatures, ac conductivities  $\sigma'$  determined at 282 MHz, which equates the NMR Larmor frequency, do also follow an Arrhenius law with an activation energy of 0.35 eV (see Fig. 8). Of course, at lower temperatures the influence of an

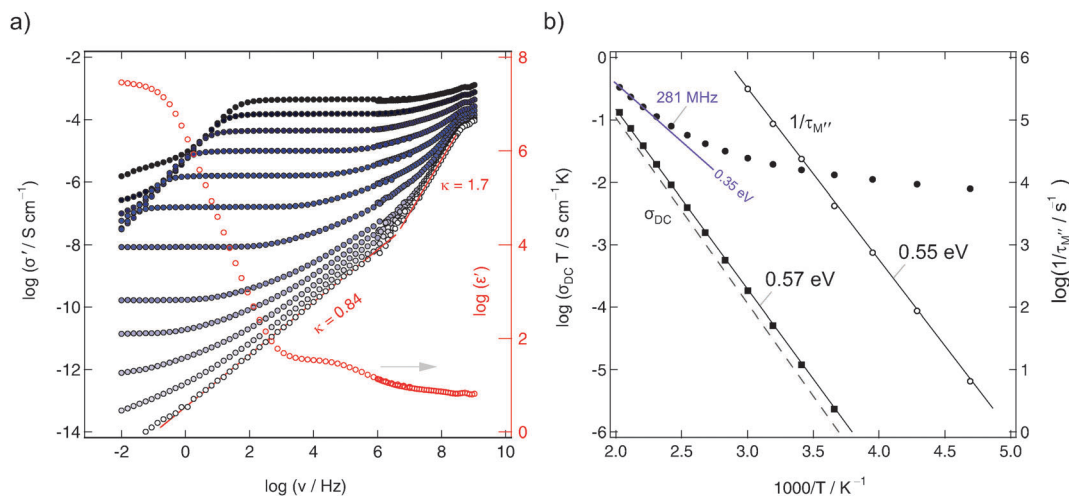


**Fig. 8** (a) Full conductivity (and permittivity, 373 K) isotherms of nanocrystalline  $\text{Ba}_{0.6}\text{La}_{0.4}\text{F}_{2.4}$  (sample 3) covering a frequency range of eleven decades. Temperatures range from 153 K to 513 K in steps of 20 K. (b) Corresponding Arrhenius plot showing the temperature behaviour of  $\sigma_{\text{DC}}T$  of sample 3 (see above) and  $\sigma'(\nu = 282 \text{ MHz})T$ . Note that 282 MHz equates the  $^{19}\text{F}$  NMR Larmor frequency. The lines show linear fits; the activation energies are indicated. For comparison, the dashed line represents  $\sigma_{\text{DC}}T$  of sample 1, which has been prepared in a tungsten carbide vial.

NCL-type contribution increases and  $\sigma'(T)$  reveals only a weak dependence on  $T$ . Let us identify the ac activation energy of 0.35 eV with that of short-range ion motion affected by correlated forward-backward jumps and  $E_{\text{a,dc}}$  with that of long-range translational ion hopping. If we do so, the difference  $E_{\text{a,dc}} - E_{\text{a,ac}} \approx 0.22 \text{ eV}$  could be interpreted in terms of the jump relaxation model as an activation energy needed for the surrounding lattice to relax towards a new equilibrium state accommodating the ion just jumped to a vacant site.<sup>58</sup>

Lastly, in order to compare the response of conductivity spectroscopy with that of NMR, within an extra experiment we recorded  $\sigma'$  (and  $\epsilon'$ ) at a single frequency but varied the temperature. In Fig. 9 the real part of the complex resistivity, which is given by  $\hat{\rho} = 1/\hat{\sigma}$  and related to the complex modulus according

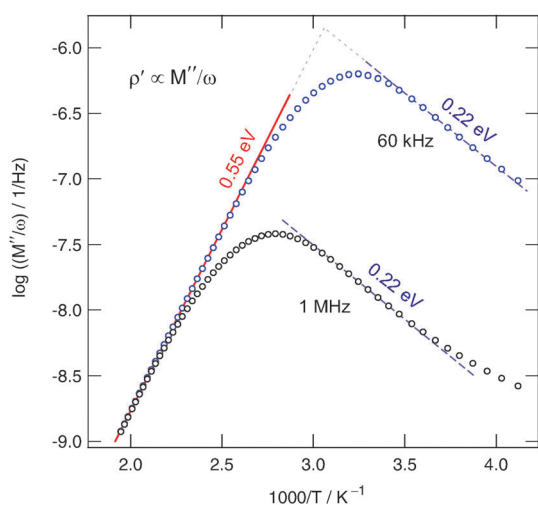


**Fig. 9** Real part of the complex resistivity of nanocrystalline  $\text{Ba}_{0.6}\text{La}_{0.4}\text{F}_{2.4}$  (sample 3) as a function of inverse temperature  $T$ . From the different flanks of asymmetric peaks obtained activation energies for long- and short-range motion can be deduced.

to  $\hat{M} = 1/\hat{\epsilon}$  via  $\hat{\rho} = \hat{M}/(i\omega\epsilon_0)$ , is plotted vs. the inverse temperature.  $\rho'$  passes through distinct maxima. If recorded at 60 kHz the peak shows up at  $T \approx 335 \text{ K}$ ; this result is in good agreement with the position of the corresponding  $1/T_{1\rho}(1/T)$ -peak, see Fig. 3. As expected, the  $\rho'(1/T)$ -peak shifts towards higher  $T$  with increasing frequency. The slope of the high temperature flank yields  $E_{\text{a},\rho} = 0.55 \text{ eV}$  ( $\approx E_{\text{a,dc}}$ ) (see the solid line drawn).

The pronounced asymmetry of the peaks is in agreement with that commonly found for glassy or at least structurally disordered ion conductors, see ref. 59, in particular. Important to note, the rather broad shape of the maximum resembles that of the  $1/T_{1\rho}(1/T)$  peak. It is an indication of a broad distribution of different relaxation mechanisms present. Before we finally compare the various activation energies obtained, we will contrast the self-diffusion coefficient obtained from the  $1/T_{1\rho}(1/T)$  peak with that which can be deduced from  $\sigma_{\text{dc}}$ . According to the NMR maximum conditions in the rotating frame of reference  $\omega_1\tau \approx 0.5$ , the jump rate is in the order of  $7.85 \times 10^5 \text{ s}^{-1}$ . With the Einstein-Smoluchowski equation  $D_{\text{sd}} = \ell^2/(6\tau)$  for 3D diffusion<sup>60</sup> this translates into a self diffusion coefficient  $D_{\text{sd}}$  of  $1.2 \times 10^{-14} \text{ m}^2 \text{ s}^{-1}$  at 380 K if we assume a jump distance  $\ell$  of approximately 3 Å. Reducing  $\ell$  to 2 Å,  $D_{\text{sd}}$  decreases to  $5.2 \times 10^{-15} \text{ m}^2 \text{ s}^{-1}$ .

However, the Nernst-Einstein equation relates  $\sigma_{\text{dc}}$  with a solid-state diffusion coefficient  $D'$ .<sup>60</sup> According to our conductivity values, diffusion coefficients of  $D'(373 \text{ K}) \approx 3.0 \times 10^{-15} \text{ m}^2 \text{ s}^{-1}$  and  $D'(393 \text{ K}) \approx 7.6 \times 10^{-15} \text{ m}^2 \text{ s}^{-1}$  are obtained. While  $D'$  is related to the tracer diffusion coefficient via  $D_{\text{tr}} = H_{\text{R}}D'$  with the Haven ratio  $H_{\text{R}}$ ;  $D_{\text{sd}}$  given by  $D_{\text{tr}} = fD_{\text{sd}}$  and  $f$  denotes the correlation factor ranging from 0 to 1. Altogether this leads to  $D_{\text{sd}} = (H_{\text{R}}/f)D'$ . Assuming that the quotient  $H_{\text{R}}/f$  is in the order of unity, good agreement between  $\sigma_{\text{dc}}$  and the appearance of the  $1/T_{1\rho}(1/T)$  rate peak is obtained. The high-temperature flank of the NMR peak is expected to be governed by an activation energy being similar to that found by dc conductivity measurements.

**Table 1** Activation energies  $E_a$  from the various NMR and conductivity methods applied

Method	$E_a$ (eV)	Type	$T$ -range, frequency
$T_1$	0.16(2)	I	220–330 K, 116 MHz
$T_2$	0.19(1)	I	350–550 K, 116 MHz
$\rho'$	0.22(2)	I	Low- $T$ flank of $(M''/\omega)$ -peaks
$\sigma'$ ac	0.35(3)	II	250–500 K, 56 kHz–282 MHz
$T_{1\rho}$	0.25–0.35	II	250–330 K, 56 kHz
$T_1$	0.44(1) <sup>a</sup>	III	400–530 K, 116 MHz
$\tau_{M''}$	0.55(1)	IV	220–400 K, modulus peaks
$\rho'$	0.55(1)	IV	High- $T$ flank of $(M''/\omega)$ -peaks
$\sigma'$ dc	0.57(1)	IV	200–500 K (sample 3)
$\sigma'$ dc	0.59(1)	IV	200–500 K (sample 1)

<sup>a</sup> Low- $T$  flank of the  $1/T_1(1/T)$ -peak.

#### D. Final discussion and comparison of activation energies

To sum up, in Table 1, the activation energies probed by both impedance and NMR spectroscopy are listed. Disregarding fully NCL-type caged dynamics (see above), the different regimes of activation energies probed illustrate the transition from short-range motions (I and II) to long-range ion transport (IV).

The data clearly illustrate that the final result for the activation energy is determined by the method chosen and its sensitivity to a specific time and length scale. Only in structurally ordered and (macroscopic) homogeneous materials with a perfectly regular energy landscape one might expect a single value for the activation energy  $E_a$ .

While the activation energy of type I might point to localized dynamics, group II could be identified with the (mean) activation energy describing the elementary jump processes in nanocrystalline  $\text{Ba}_{0.6}\text{La}_{0.4}\text{F}_{2.4}$ . The relatively large value probed by  $T_1$  NMR seems to reflect an anomaly coupled with the different jump mechanisms leading to long-range ion transport. It is worth noting that the latter result does not depend on the integration range of the underlying NMR free induction decays. This means that it does not play a role whether parts of the free induction decays or the whole integral over the transient signal is analysed in terms of a saturation recovery experiment to extract the  $T_1$  rates. In all cases the same magnetization recovery curve is obtained which follows a pure exponential containing a single  $T_1^{-1}$  rate. Hence, from the point of view of SLR NMR the spin ensemble appears as a dynamically uniform system. Even if there are any microscopic spin regions acting differentially, fast spin-diffusion, *i.e.*, so-called spin flip-flop processes without mass transfer, results in a homogeneous  $^{19}\text{F}$  NMR spin system characterised by a single spin temperature.

## IV. Conclusions

Up to a certain concentration the mechanochemical introduction of La ions into  $\text{BaF}_2$  leads to solid solutions of  $\text{Ba}_{1-x}\text{La}_x\text{F}_{2+x}$  crystallizing with a fluorite-type structure.<sup>9</sup> Structural disorder and strain owing to the socialization of two cations with largely different radii, see also ref. 44, is anticipated to severely affect

overall ion transport of  $\text{F}^-$ . The relatively high ion conductivity of  $\text{Ba}_{1-x}\text{La}_x\text{F}_{2+x}$  with  $x = 0.4$  at elevated temperatures makes the cation-mixed material a promising solid electrolyte in modern energy storage systems with  $\text{F}^-$  ions as charge carriers. Preliminary solid-state cyclovoltammetry measurements<sup>10</sup> encouragingly show a sufficiently good electrochemical stability over a relatively large potential window.

Here, we could show, by using both atomic-scale NMR relaxation and (high-frequency) broadband impedance spectroscopy, that  $\text{F}^-$  ion transport in the ternary fluoride is governed by multiple hopping processes. Depending on the time scale the particular technique is sensitive to, we could distinguish between short-range and long-range translational dynamics. This manifests in a broad range of activation energies found spanning the range from localized hopping (0.16 eV) to macroscopic ion transport (0.55 eV). Interestingly, an anomaly is found when activation energies obtained from ac conductivity spectroscopy (0.35 eV) are compared with that deduced from diffusion-induced  $T_1^{-1}$   $^{19}\text{F}$  NMR performed at 282 MHz. This might be explained by the fact that the two methods, even if applied in the same frequency window, do probe different motional correlation functions. Structural heterogeneities, such as the formation of  $\text{F}^-$  clusters,<sup>9,54,55,61</sup> or size effects such as the influence of space charge zones<sup>62,63</sup> in materials with a large surface area might also be considered to discuss the results found. To this end, detailed structural information is needed to correlate them with the dynamic properties studied here.

Unfortunately, due to the heat sensitivity of the sample we could not probe the high-temperature flank of the corresponding  $^{19}\text{F}$  NMR peak in the rotating frame of reference. Fortunately, *via* the shallow maximum detected at approximately 380 K the F self-diffusion coefficient  $D_{\text{sd}}$  could be determined. A value of  $7.85 \times 10^5 \text{ s}^{-1}$  is in line with that which can be estimated from dc conductivity results. This is consistent with the agreement between activation energies from ac conductivity and the low- $T$  flank of the  $T_{1\rho}^{-1}$  NMR peak.

## Author contributions

The authors were equally involved in experimental work, data analysis and project planning. All authors have given approval to the final version of the manuscript.

## Acknowledgements

We thank our colleagues at the TU Graz and the University of Hannover, especially A. Düvel, for valuable discussions concerning sample preparation and characterisation. Financial support by the Deutsche Forschungsgemeinschaft (DFG), SPP 1415, the Austrian Federal Ministry of Economy, Family and Youth, and the Austrian National Foundation for Research, Technology and Development is greatly appreciated. Furthermore, we thank the DFG for access to the NMR and impedance spectrometers of the DFG Research Unit 1277, grant no. WI3600/2-1 and 4-1.

## References

- 1 K. Funke, *Sci. Technol. Adv. Mater.*, 2013, **14**, 043502.
- 2 P. Knauth, *Solid State Ionics*, 2009, **180**, 911.
- 3 *Nanocomposites: Ionic Conducting Materials and Structural Spectroscopies*, ed. P. Knauth and J. Schoonman, Springer, Berlin, 2008.
- 4 A. Hayashi, K. Noi, A. Sakuda and M. Tatsumisago, *Nat. Commun.*, 2012, **3**, 856.
- 5 L. N. Patro and K. Hariharan, *Solid State Ionics*, 2013, **239**, 41.
- 6 J. Schoonman, K. Wapenaar, G. Oversluizen and G. Dirksen, *J. Electrochem. Soc.*, 1979, **126**, 709.
- 7 J. Schoonman and A. Wolfert, *J. Electrochem. Soc.*, 1981, **128**, 1522.
- 8 M. A. Reddy and M. Fichtner, *J. Mater. Chem.*, 2011, **21**, 17059.
- 9 C. Rongeat, M. A. Reddy, R. Witter and M. Fichtner, *J. Phys. Chem. C*, 2013, **117**, 4943.
- 10 I. Hanzu, A. Düvel, F. Preishuber-Pflügl, P. Heitjans and M. Wilkening, 2013, to be published.
- 11 V. Epp, z. Gün, H.-J. Deiseroth and M. Wilkening, *J. Phys. Chem. Lett.*, 2013, **4**, 2118.
- 12 A. Kuhn, S. Narayanan, L. Spencer, G. R. Goward, V. Thangadurai and M. Wilkening, *Phys. Rev. B: Condens. Matter Mater. Phys.*, 2011, **83**, 94302.
- 13 P. M. Richards, in *Topics in Current Physics*, ed. M. B. Salamon, Springer, Berlin, 1979, vol. 15.
- 14 P. Heitjans, A. Schirmer and S. Indris, in *Diffusion in Condensed Matter – Methods, Materials, Models*, ed. P. Heitjans and J. Kärger, Springer, Berlin, 2nd edn, 2005, ch. 9, pp. 369–415.
- 15 D. Brinkmann, *Prog. Nucl. Magn. Reson. Spectrosc.*, 1992, **24**, 527.
- 16 R. Böhmer, K. Jeffrey and M. Vogel, *Prog. Nucl. Magn. Reson. Spectrosc.*, 2007, **50**, 87.
- 17 M. Wilkening and P. Heitjans, *ChemPhysChem*, 2012, **13**, 53.
- 18 M. Wilkening and P. Heitjans, *Phys. Rev. B: Condens. Matter Mater. Phys.*, 2008, **77**, 024311.
- 19 H. Buschmann, J. Dölle, S. Berendts, A. Kuhn, P. Bottke, M. Wilkening, P. Heitjans, A. Senyshyn, H. Ehrenberg and A. Lotnyk, *et al.*, *Phys. Chem. Chem. Phys.*, 2011, **13**, 19378.
- 20 J. Langer, V. Epp, P. Heitjans, F. A. Mautner and M. Wilkening, *Phys. Rev. B: Condens. Matter Mater. Phys.*, 2013, **88**, 094304.
- 21 P. Heitjans and M. Wilkening, *Mater. Res. Bull.*, 2009, **34**, 915.
- 22 P. Heitjans, E. Tobschall and M. Wilkening, *Eur. Phys. J.: Spec. Top.*, 2008, **161**, 97.
- 23 A. Kuhn, M. Kunze, P. Sreeraj, H. D. Wiemhöfer, V. Thangadurai, M. Wilkening and P. Heitjans, *Solid State Nucl. Magn. Reson.*, 2012, **42**, 2.
- 24 A. Kuhn, P. Sreeraj, R. Pöttgen, H.-D. Wiemhöfer, M. Wilkening and P. Heitjans, *J. Am. Chem. Soc.*, 2011, **133**, 11018.
- 25 M. Wilkening, W. Küchler and P. Heitjans, *Phys. Rev. Lett.*, 2006, **97**, 065901.
- 26 M. Wilkening, V. Epp, A. Feldhoff and P. Heitjans, *J. Phys. Chem. C*, 2008, **112**, 9291.
- 27 K. Funke, *Prog. Solid State Chem.*, 1993, **22**, 111.
- 28 K. Funke, C. Cramer and D. Wilmer, in *Diffusion in Condensed Matter – Methods, Materials, Models*, ed. P. Heitjans and J. Kärger, Springer, Berlin, 2nd edn, 2005, ch. 21, pp. 857–893.
- 29 M. Meyer, P. Maass and A. Bunde, *Phys. Rev. Lett.*, 1993, **71**, 573.
- 30 A. Bunde, W. Dieterich, P. Maass and M. Meyer, in *Diffusion in Condensed Matter – Methods, Materials, Models*, ed. P. Heitjans and J. Kärger, Springer, Berlin, 2nd edn, 2005, ch. 20, pp. 813–856.
- 31 D. R. Figueroa, A. V. Chadwick and J. H. Strange, *J. Phys. C: Solid State Phys.*, 1978, **11**, 55.
- 32 O. Kanert, R. Küchler, K. L. Ngai and H. Jain, *Phys. Rev. B: Condens. Matter Mater. Phys.*, 1994, **49**, 76.
- 33 K. Ngai, *Phys. Rev. B: Condens. Matter Mater. Phys.*, 1993, **48**, 13481.
- 34 V. Epp, O. Gün, H.-J. Deiseroth and M. Wilkening, *Phys. Chem. Chem. Phys.*, 2013, **15**, 7123.
- 35 K. L. Ngai, *Relaxation and Diffusion in Complex Systems*, Springer, New York, 2011.
- 36 D. L. Sidebottom, *Rev. Mod. Phys.*, 2009, **81**, 999.
- 37 J. R. Macdonald, *J. Appl. Phys.*, 1998, **84**, 812.
- 38 K. Ngai and C. León, *J. Non-Cryst. Solids*, 2003, **315**, 124.
- 39 D. Ailion and C. P. Slichter, *Phys. Rev. Lett.*, 1964, **12**, 168.
- 40 N. Bloembergen, E. M. Purcell and R. V. Pound, *Phys. Rev.*, 1948, **73**, 679.
- 41 V. Šepelák, A. Düvel, M. Wilkening, K.-D. Becker and P. Heitjans, *Chem. Soc. Rev.*, 2013, **42**, 7507.
- 42 B. Ruprecht, M. Wilkening, S. Steuernagel and P. Heitjans, *J. Mater. Chem.*, 2008, **18**, 5412.
- 43 B. Ruprecht, M. Wilkening, A. Feldhoff, S. Steuernagel and P. Heitjans, *Phys. Chem. Chem. Phys.*, 2009, **11**, 3071.
- 44 A. Düvel, B. Ruprecht, P. Heitjans and M. Wilkening, *J. Phys. Chem. C*, 2011, **115**, 23784.
- 45 A. Düvel, M. Wilkening, R. Uecker, S. Wegner, V. Šepelák and P. Heitjans, *Phys. Chem. Chem. Phys.*, 2010, **12**, 11251.
- 46 A. Düvel, S. Wegner, K. Efimov, A. Feldhoff, P. Heitjans and M. Wilkening, *J. Mater. Chem.*, 2011, **21**, 6238.
- 47 E. Fukushima and S. B. W. Roeder, *Experimental Pulse NMR: A Nuts and Bolts Approach*, Addison-Wesley Pub. Co., Advanced Book Program, Reading, Mass., 1981.
- 48 P. Heitjans, A. Schirmer and S. Indris, in *Diffusion in Condensed Matter*, ed. P. Heitjans and J. Kärger, Springer, 2005, ch. 9, p. 367.
- 49 C. P. Slichter and D. Ailion, *Phys. Rev.*, 1964, **135**, A1099.
- 50 D. C. Ailion and C. P. Slichter, *Phys. Rev.*, 1965, **137**, A235.
- 51 D. C. Look and I. J. Lowe, *J. Chem. Phys.*, 1966, **44**, 2995.
- 52 T. J. Rowland and F. Y. Fradin, *Phys. Rev.*, 1969, **182**, 760.
- 53 D. Wolf, *Phys. Rev. B: Solid State*, 1974, **10**, 2724.
- 54 K. E. D. Wapenaar, J. L. Van Koesveld and J. Schoonman, *Solid State Ionics*, 1981, **2**, 145.

- 55 A. K. Ivanov-Shits, N. I. Sorokin, P. P. Fedorov and B. P. Sobolev, *Solid State Ionics*, 1989, **31**, 269.
- 56 N. I. Sorokin and M. W. Breiter, *Solid State Ionics*, 1997, **99**, 241.
- 57 E. Barsis and A. Taylor, *J. Phys. Chem.*, 1968, **48**, 4357.
- 58 K. Funke and R. D. Banhatti, *J. Mater. Sci.*, 2007, **42**, 1942–1947.
- 59 B. Munro, M. Schrader and P. Heitjans, *Ber. Bunsenges. Phys. Chem.*, 1992, **96**, 1718.
- 60 H. Mehrer, *Diffusion in Solids*, Springer, Berlin, 2006.
- 61 F. Wang and C. P. Grey, *Chem. Mater.*, 1998, **10**, 3081.
- 62 J. Maier, *Prog. Solid State Chem.*, 1995, **23**, 171.
- 63 W. Puin, S. Rodewald, R. Ramlau, P. Heitjans and J. Maier, *Solid State Ionics*, 2000, **131**, 159.



### 5.3 Mechanosynthesis of BaMgF<sub>4</sub>

The common application of BaMgF<sub>4</sub> is found in optics, where it is intended to be used as an all solid state laser material.<sup>88–91</sup> However, its anisotropic diffusion characteristics make it an interesting candidate for investigations with impedance spectroscopy. In a study of single-crystalline BaMgF<sub>4</sub> Kannan *et al.* found a strong dependence of the ionic conductivity on the orientation of the crystal lattice.<sup>92</sup> The highest conductivity was found along the *c*-axis. This can be related to the corner-sharing MgF<sub>6</sub>-octahedra that are aligned towards this crystallographic orientation, as it is schematically illustrated in Figure 25b). Diffusion along other orientations is less favored, especially along the *b*-axis, as the Ba<sup>2+</sup>-cations separate the MgF<sub>6</sub>-units in this direction. In the present study, BaMgF<sub>4</sub> was prepared by mechanochemical pathways. Interestingly, the anisotropic characteristics of the conductivity could be found for the nanocrystalline powder as well. It is expressed by the shallow slope of the conductivity isotherms of the material. At high frequencies, the exponent  $\kappa$  of the power law fits exhibits values smaller than 0.5 which points to low dimensional conductivity.<sup>93</sup>

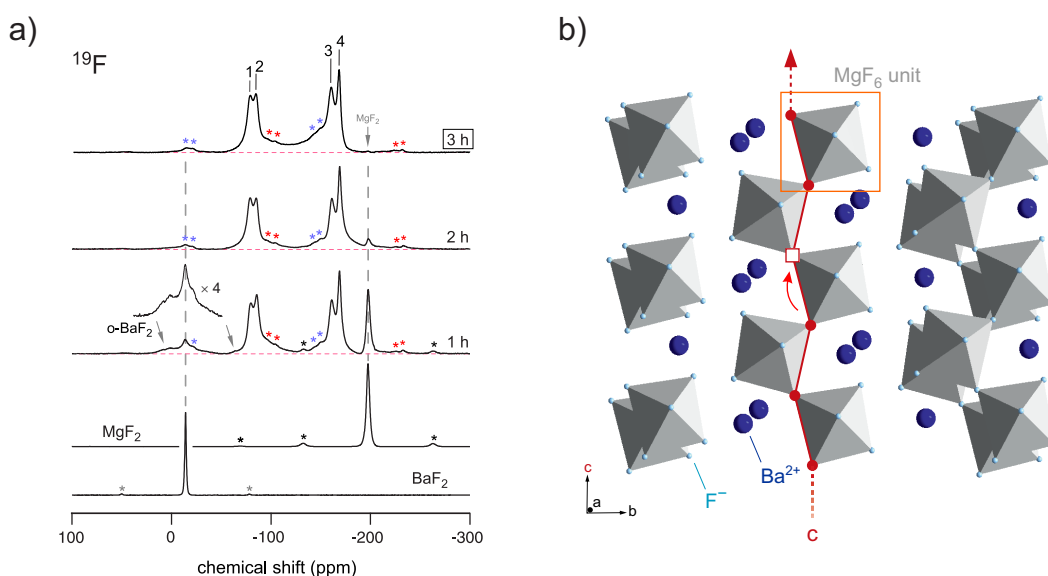


**Figure 25** – a) <sup>19</sup>F MAS NMR spectra of the reaction mixture after  $t=0, 1, 2$  and  $3$  h clearly demonstrate the presence of the starting material after the first milling intervals. b) Illustration of the crystal structure that shows the alignment of the MgF<sub>6</sub>-octahedra along the *c*-axis providing a preferred pathway for the diffusion of F-ions.

The second highlight of the investigations on BaMgF<sub>4</sub> was the study of the synthesis procedure itself by a combination of X-ray diffraction and <sup>19</sup>F MAS NMR spectroscopy. This quasi enabled an *in-situ* monitoring of the conversion of the binary fluorides into the product as the reaction immediately stops when the mill is switched off. While X-ray

spectroscopy was unable to detect the  $\text{MgF}_2$ -signal, it could be well resolved by the help of MAS NMR (see Figure 25a). This might result from an amorphization of the magnesium fluoride due to the treatment in the mill or simply from a superposition of the X-ray signals in the diffraction pattern. However, these findings highlight the suitability of MAS NMR for the structural characterization of inorganic solids.

At the time that the results of these investigations were published, it was the first report of a mechanochemical synthesis of  $\text{BaMgF}_4$ . However, a similar approach was recently published by Scholz and co-workers using acetates as a starting material.<sup>94</sup> Detailed results and further discussion are given in the publication below.

---

P3: (pp. 73-80)

**Evidence of low dimensional ion transport in  
mechanosynthesized nanocrystalline BaMgF<sub>4</sub>**

F. Preishuber-Pflügl and M. Wilkening,

*Dalton Trans.*, 2014, **43**, 9901.



## Evidence of low dimensional ion transport in mechanosynthesized nanocrystalline BaMgF<sub>4</sub>

Cite this: *Dalton Trans.*, 2014, **43**, 9901

F. Preishuber-Pflügl\* and M. Wilkening

Mechanochemical milling provides a versatile method for the preparation of nano-sized, defect rich, polycrystalline materials. If ionic materials are considered, the transport parameters of the mobile ions may greatly differ from those of the microcrystalline counterparts prepared by conventional synthesis routes. Little is known about ionic conduction in nanocrystalline materials having crystal structures that offer spatially confined transport pathways. Here, we focused on mechanosynthesized BaMgF<sub>4</sub> that combines both nanocrystallinity and anisotropic F<sup>-</sup> transport. The preparation of nanocrystalline BaMgF<sub>4</sub> is presented as a facile and rapid one-pot procedure. The reaction was followed by X-ray diffraction and high-resolution <sup>19</sup>F nuclear magnetic resonance (NMR) spectroscopy. NMR helped prove the formation of X-ray amorphous compounds as well as the transformation of the starting materials into the final product BaMgF<sub>4</sub>. Most importantly, besides enhanced conduction properties compared to a single crystal, our broadband impedance spectra reveal characteristics pointing to anisotropic (low dimensional) ion transport processes even in the nanocrystalline form of BaMgF<sub>4</sub>.

Received 26th March 2014,

Accepted 9th May 2014

DOI: 10.1039/c4dt00904e

www.rsc.org/dalton

### Introduction

Adaptable synthesis techniques provide the basis for the development of new functional materials which are crucially needed for, *e.g.*, new sensors, catalysts or powerful energy storage systems taking advantage of solid state ion conductors. High-energy ball-milling has been proven to be a highly versatile method for the preparation of nanocrystalline solids with extraordinary micro- as well as macroscopic properties such as optical, electrical or magnetic behaviour.<sup>1,2</sup>

In many cases, but not in all, nanocrystalline materials prepared in this way show enhanced ion transport properties.<sup>2,3</sup> Increased ion dynamics is directly linked with the great amount of defects introduced during mechanical treatment.<sup>3,4</sup> The different types of defects generated determine both bulk properties as well as those related to the large volume fraction of interfacial regions (or grain boundaries). Compared to their coarse-grained or single crystalline counterparts, the mean crystallite diameter of cluster-assembled nanocrystalline ceramics is smaller than 50 nm. Their various properties are governed by the large number fraction of ions in or near the interfacial regions, that is, the surface-influenced volume. Depending on the thickness of the surface layer, which may range from 0.5 to 2 nm, for a mean crystallite size of approxi-

mately 20 nm up to 20 to 30% of the ions may reside in the interfacial regions. As an example this has been shown for Li-bearing nanocrystalline oxides such as Li<sub>2</sub>O and LiNbO<sub>3</sub>.<sup>2,3</sup> Besides the preparation of thermodynamically stable compounds, in the extreme case mechanochemistry also provides access to metastable and nanocrystalline phases that cannot be prepared *via* conventional synthesis routes requiring high temperatures, see, *e.g.*, ref. 5–8.

Although a huge number of studies can be found focusing on the synthesis and characterization of nanocrystalline ion conducting ceramics,<sup>2</sup> investigations putting emphasis on ion dynamics in nanocrystalline conductors crystallising with structures that offer spatially confined transport pathways are scarce. Little is known how anisotropic transport is altered when such materials have been prepared in a nanocrystalline form *via* mechanosynthesis. Here, ferroelectric BaMgF<sub>4</sub>, crystallising with the orthorhombic BaZnF<sub>4</sub> structure (space group *Cmc*2<sub>1</sub>, see Fig. 1), was chosen as a suitable model system combining these two aspects.

In its single crystalline form, the ternary fluoride reveals highly anisotropic ion conduction. This was shown by Kannan *et al.*<sup>9</sup> who investigated ion transport at high temperatures by means of impedance spectroscopy. The authors report on enhanced conductivity along the *c*-axis of a single crystal, which enables fluorine ions to jump *via* vacant sites along the corner sharing octahedra.<sup>10</sup> In BaMgF<sub>4</sub> the MgF<sub>6</sub> octahedra are linked *via cis* vertices to zigzag chains parallel to the *c*-axis; along the *a*-axis, these chains are connected *via trans* vertices to slabs parallel to the *ac*-plane. The same anisotropy in ion

Graz University of Technology, Institute for Chemistry and Technology of Materials (Member of NAWI Graz), Stremayrgasse 9, 8010 Graz, Austria.  
E-mail: preishuber-pfluegl@tugraz.at

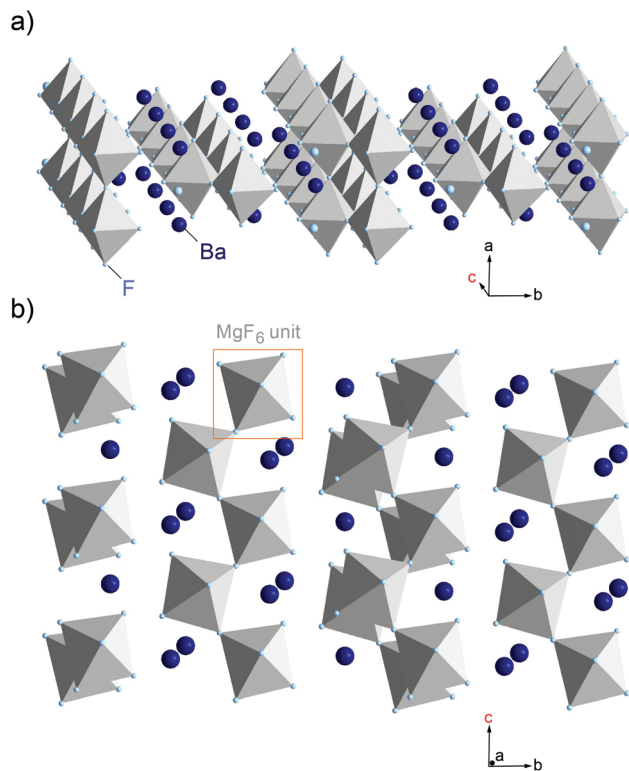


**Fig. 1** Crystal structure of  $\text{BaMgF}_4$  (space group  $\text{Cmc}2_1$ ) illustrating the connectivity of the  $\text{MgF}_6$  octahedra and the anisotropic migration pathway of the F anions along the  $c$ -axis.

conduction has also been found for  $\text{BaMnF}_4$  and other compounds of this isomorphous family. From an application point of view,  $\text{BaMgF}_4$  is known as a promising material for all-solid-state laser applications;<sup>11</sup> moreover, it is a candidate for non-destructive readout ferroelectric random access memory devices using metal-ferroelectric-semiconductor structures.<sup>12</sup>

In the present study, it was synthesized *via* ball-milling directly from the binary fluorides  $\text{BaF}_2$  and  $\text{MgF}_2$ . The reaction was carried out as a one-pot procedure yielding a phase-pure powder already after three hours of milling; no further purification or annealing steps were necessary. The convenience of this versatile synthesis route also highlights the benefits of mechanochemistry compared to other methods such as high temperature solid-state synthesis, including hydrothermal routes, sol-gel reactions or wet chemical methods.<sup>13–17</sup>

Compared to single crystalline  $\text{BaMgF}_4$  we found enhanced ion transport properties for the nanocrystalline form investigated here. Permittivity and conductivity spectra are discussed in terms of electrical responses resulting from bulk and grain boundary regions. Interestingly, even in the case of a nanocrystalline, mechano-synthesized sample, the frequency-dependent conductivity measurements carried out point to low dimensional ionic conduction along the  $c$ -axis. This can be inferred from the shallow frequency dependence in the dispersive regions of the conductivity isotherms. Such features have only

rarely been used to enlighten the effect of dimensionality of a given hopping process on the frequency dependence of conductivity values.<sup>18</sup>

## Experimental section

### Materials and methods

$\text{BaMgF}_4$  was synthesized by mechanical treatment of the binary fluorides in a high-energy ball mill (Fritsch Pulverisette 7 premium line). Stoichiometric amounts of  $\text{BaF}_2$  and  $\text{MgF}_2$  were milled using 180 balls made of zirconium dioxide ( $\text{ZrO}_2$ ) with a diameter of 5 mm in beakers of the same material. The ball-to-powder ratio was set to 14 : 1. To exclude any moisture and the influence of any oxygen during milling, the powders and beakers were strictly handled in a glovebox filled with a dry argon atmosphere ( $\text{O}_2$  and  $\text{H}_2\text{O} < 0.5$  ppm). If not stated otherwise, the total milling time was set to three hours consisting of 36 cycles à five minutes, each one followed by a resting interval of 25 minutes allowing the beakers to cool down. After each hour of milling, *i.e.*, after twelve cycles, the beakers were opened and the powder was completely removed and homogenized in an agate mortar; then, the samples for X-ray diffraction (XRD) and magic angle spinning nuclear magnetic resonance (MAS NMR) analysis were taken, see Fig. 2. It should be mentioned that the amount of the samples taken out was very small in order not to change the ball to powder ratio.

Structural characterisation of the resulting powders was carried out on a Bruker D8 Advance diffractometer with Bragg Brentano geometry using  $\text{Cu K}\alpha$  radiation (10 to  $100^\circ 2\theta$ , step size  $0.02^\circ 2\theta$ , step time 1 s). Rietveld-refinement was done with X-PertHighScorePlus (PANalytical).  $^{19}\text{F}$  MAS NMR experiments were recorded on a Bruker Avance III spectrometer operating at 470.4 MHz employing a 2.5 mm-MAS probe (Bruker) being able to reach a maximum spinning speed of 30 kHz. Spectra were referenced to solid, crystalline  $\text{LiF}$  ( $-204.3$  ppm) serving as a secondary standard (primary reference  $\text{CFCl}_3$ , 0 ppm), see Fig. 2(b). Spectra were recorded after non-selective excitation with a single radio-frequency pulse; the pulse length was 2  $\mu\text{s}$ . After Fourier transformation of the free induction decays, phase correction in first and second order was carried out using TopSpin software and MestreNova.

For our dielectric measurements, 200 mg of the powder were pressed in a mould with 10 mm inner diameter applying a uniaxial pressure of 0.13 GPa yielding pellets of about 1 mm in thickness, each time measured with an appropriate caliper. 100 nm of gold, serving as electrodes, were applied on both sides of the pellet with a sputter coater (Leica) to ensure good electrical contact. Impedance spectra (see Fig. 3) were measured with a Novocontrol Concept 80 broadband analyser (Alpha-AN, Novocontrol) using a BDS 1200 cell in combination with an active ZGS cell interface (Novocontrol) allowing temperature-variable two-electrode (dielectric) measurements. Frequencies covered a range of nine decades, starting from  $10^{-2}$  Hz up to 10 MHz. The temperature was varied between

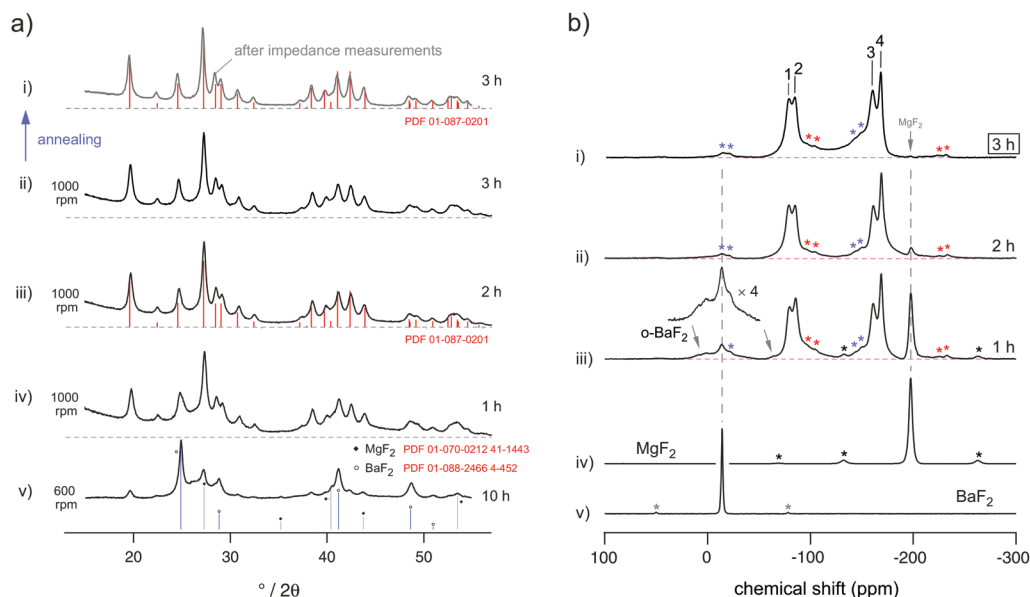


**Fig. 2** (a) X-ray powder diffraction patterns of the ball-milled reaction mixture after 1 h, 2 h, and 3 h of milling at 1000 rpm in  $\text{ZrO}_2$  beakers; reflections of a  $\text{BaMgF}_4$  single crystal are indicated by vertically drawn (red) lines. The patterns are stacked with a constant pitch. For comparison, the powder pattern obtained when the milling conditions are changed to 600 rpm and 10 h, that is lower mechanical impact but longer milling time, is also shown, see (v). The pattern labelled (i) is obtained after impedance measurements. (b)  $^{19}\text{F}$  MAS NMR spectra of the reaction mixture at different stages of milling. Spectra were recorded at a spinning speed of 30 kHz. Asterisks indicate the various spinning side bands of the  $\text{BaMgF}_4$  signal as well as those originating from the starting materials. (iv) and (v) show reference NMR spectra of the non-treated starting materials  $\text{BaF}_2$  and  $\text{MgF}_2$ . Small arrows indicate those NMR lines that can be assigned to orthorhombic  $\text{BaF}_2$ . In (iii) the region from 50 ppm to -50 ppm is enlarged to illustrate additional NMR intensities near the  $^{19}\text{F}$  signal of  $\text{BaF}_2$ .

133 and 573 K in steps of 10 K; it was automatically controlled by a QUATRO cryosystem (Novocontrol). A dry nitrogen atmosphere with the appropriate temperature is built up around the sample in the cryostat by a constant flow of gas, freshly evaporated from a dewar containing liquid nitrogen.

## Results and discussion

### Sample characterisation by X-ray diffraction

Fig. 2(a) shows the X-ray powder diffraction patterns of the resulting nanocrystalline materials after treating the binary fluorides,  $\text{BaF}_2$  and  $\text{MgF}_2$ , over an increasing amount of time in a planetary mill at 1000 rounds per minute (rpm). Already after one hour (see the pattern labelled (iv)), the diffraction pattern solely reveals the formation of only one phase *viz* orthorhombic  $\text{BaMgF}_4$ . Broad background signals, however, show up at small diffraction angles that indicate the presence of a certain amount of amorphous material. This could either result from amorphous  $\text{BaF}_2$  and/or  $\text{MgF}_2$  formed under the harsh milling conditions or from abrasion of zirconium dioxide from the milling tools. The former explanation is supported by our NMR measurements (see below); residues of the starting materials become X-ray amorphous; however, they can be identified by  $^{19}\text{F}$  MAS NMR. It turned out that the isotropic chemical shifts of amorphous  $\text{BaF}_2$  and  $\text{MgF}_2$  are almost identical with those of the crystalline counterparts. The same has been found previously for pure, nanocrystalline  $\text{BaF}_2$ .<sup>6</sup> Of course, XRD reflections with weak intensity belonging to the

binary fluorides could be hidden by the broadened signals of  $\text{BaMgF}_4$  governing the pattern. It is worth mentioning that lowering the mechanical impact, *i.e.*, using 600 rpm instead of 1000 rpm, does not lead to a complete formation of  $\text{BaMgF}_4$  even if the milling time is increased from 1 h to 10 h. This is illustrated by the X-ray powder pattern (v) included in Fig. 2(a).

The mean crystallite size of our samples treated at 1000 rpm ranges from about 10 nm after one hour of milling to about 7 nm to 15 nm after three hours. These values have been estimated using the equation introduced by Scherrer with a shape factor of 0.9 representing spherical crystallites. They do not take into account the influence of strain generated during milling; such an effect, however, does not change the estimated values much as has been shown by previous studies on similar fluorides.<sup>8,19</sup>

In Table 1 the cell parameters obtained from Rietveld refinement are listed. Compared to the results on  $\text{BaMgF}_4$  single crystals,<sup>20</sup> ball milling leads to a slight distortion of the cell geometry; the position of the reflections are marginally shifted towards larger diffraction angles. In spite of that, the decrease of the Bragg factor  $R_{\text{Bragg}}$  with increasing milling time reveals that the resulting structure increasingly resembles that of  $\text{BaMgF}_4$  described in the literature.<sup>20</sup>

### Further characterisation by high-resolution solid-state $^{19}\text{F}$ NMR spectroscopy

Compared to X-ray diffraction, MAS NMR spectroscopy allows more distinct insights into the mechanochemical reaction pro-

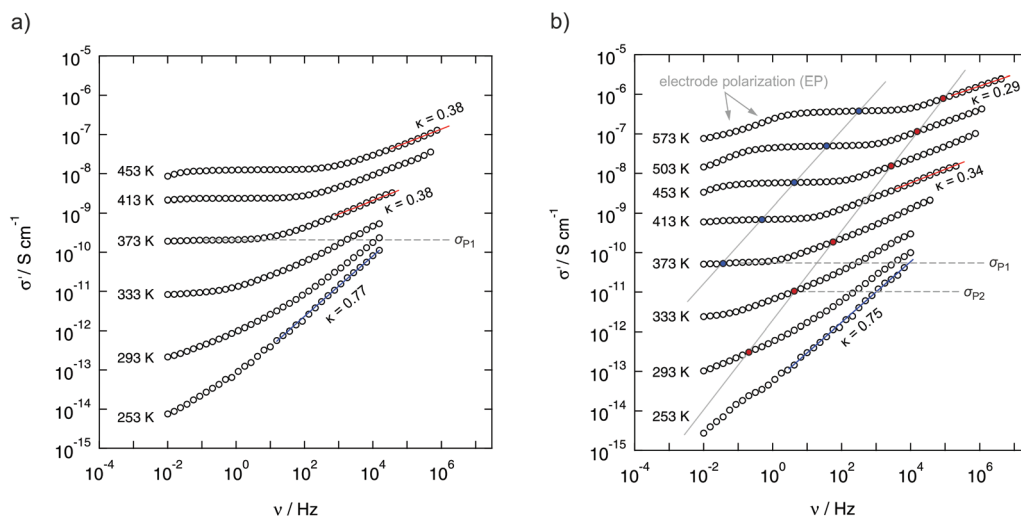


**Fig. 3** Conductivity isotherms (real part of complex conductivity vs. frequency) recorded of the sample obtained after three hours of milling. (a) Data obtained from the second heating run up to 473 K and (b), from the third heating run up to 573 K. All the spectra shown reveal characteristic dc-conductivity plateaus at elevated temperatures. Additional plateaus, however, show up at higher frequencies. They are highlighted in (b) by red circles. Conductivities at the highest frequencies can be approximated with power laws.  $\kappa$  values indicate the corresponding power law exponents. Arrows in (b) mark polarisation effects due to the ion blocking electrodes applied.

**Table 1** Lattice parameters of the mechano-synthesized powders as obtained from Rietveld refinement; data for the  $\text{BaMgF}_4$  single crystal listed were taken from ref. 20

Milling time/h	$a/\text{\AA}$	$b/\text{\AA}$	$c/\text{\AA}$	$R_{\text{Bragg}}$
1	4.146(1)	14.479(1)	5.814(1)	9.2
2	4.141(1)	14.489(1)	5.813(1)	6.4
3	4.139(1)	14.495(1)	5.810(1)	5.5
Single crystal	4.126	14.518	5.821	—

cedure; the evolution of the characteristic  $\text{BaMgF}_4$  NMR signals and the decrease of the corresponding intensities of the starting materials is clearly outlined in the spectra shown in Fig. 2(b).

By using a rotation frequency of 30 kHz, four different fluorine sites, being crystallographically and magnetically inequivalent, can be distinguished *via* MAS NMR:  $-79.5$  ppm (1),  $-85.1$  ppm (2),  $-160.6$  ppm (3) and  $-168.6$  (4) ppm, see Fig. 2(b) (i) to (iii), the NMR lines are indicated by numbers. These values are in good agreement with results from other studies reported in the literature but focusing on, *e.g.*, single crystalline and polycrystalline  $\text{BaMgF}_4$  synthesized *via* solid state pathways.<sup>13</sup> Once again, this comparison shows that  $^{19}\text{F}$  NMR chemical shifts of nanocrystalline mechano-synthesized fluorides do not differ much from those of crystalline materials. In our case, however, the  $^{19}\text{F}$  MAS NMR lines are considerably broadened, pointing at significant structural disorder due to the enormous mechanical impact during milling.

Besides the formation of the desired ternary fluoride, which shows up already after just 1 hour of milling, in the early stages of mechanical treatment NMR lines of orthorhombic  $\text{BaF}_2$  show up. This behaviour was also observed previously for pure  $\text{BaF}_2$  prepared in a similar way.<sup>5,6,8</sup> Orthorhombic  $\text{BaF}_2$  is a high pressure phase of barium fluoride which forms under

the milling conditions chosen here.<sup>5</sup> With increasing milling time, however, it is completely transformed into  $\text{BaMgF}_4$ .

Regarding the ppm region from 20 ppm to  $-50$  ppm in more detail (Fig. 2(b), (iii)), additional NMR lines with low intensity show up after one hour of milling. They cannot be completely assigned to the formation of orthorhombic  $\text{BaF}_2$ . Most likely, these intensities point to  $^{19}\text{F}$  chemical shifts of a small amount of (X-ray amorphous) Mg doped cubic- $\text{BaF}_2$  that might represent the initial reaction product which is then continuously transformed into  $\text{BaMgF}_4$ .

After three hours of milling, the NMR lines of  $\text{BaF}_2$  and  $\text{MgF}_2$  as well as the weak signals of the side products completely disappeared. Compared to our experiments performed at only 600 rpm, the preparation of pure  $\text{BaMgF}_4$ , as it is carried out here, is driven by the higher mechanical impact at 1000 rpm leading to increased grinding and local pressure. Additionally, the effect of hot spots may further support the transformation of  $\text{BaF}_2$  and  $\text{MgF}_2$  into phase pure  $\text{BaMgF}_4$ . For comparison with other synthesis routes, the high rotation speed of 1000 rpm leads to a temperature increase from room temperature to approximately 370 K inside of the beakers. A precise value of temperature and pressure, giving clear insights into the reaction conditions inside the milling beakers cannot be given as our current synthesis equipment does not support a measurement of these values. Here, we roughly estimated the inner temperature from measurement on the outer surface of the beakers.

#### Ion dynamics probed by temperature-variable impedance and dielectric measurements

The dielectric response of mechano-synthesized  $\text{BaMgF}_4$  was investigated at temperatures ranging from 133 K to 573 K over a broad frequency range ( $\nu = 10$  mHz to 10 MHz) covering nine

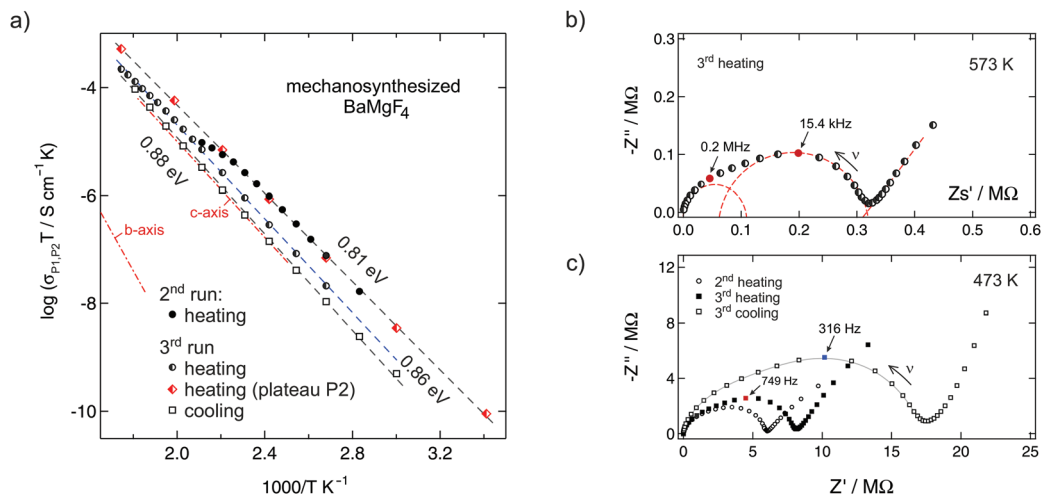


**Fig. 4** (a) Arrhenius diagram showing the temperature dependence of the dc-conductivity and of the additional plateau value of Fig. 3. (b) The dashed lines show Arrhenius fits. For comparison, the dashed-dotted line represents the conductivity of a single crystal along the *b*-axis; the values for conduction along the *c*-axis coincide with our data found for the third cooling cycle. (b, c) Complex plane plots of the real part vs. the imaginary part of the impedance show depressed, overlapping semi-circles for the ball milled, nanocrystalline samples. The coloured symbols (to which the arrows point) represent the frequency at the maximum of the semicircle. (b) The red, dashed semicircles schematically represent two different diffusion processes corresponding to the plateaus P1 and P2 in Fig. 3(b). (c) The grey, solid line serves as a guide to the eye.

decades (see Fig. 3 and 4). This enabled us to get detailed insights into the length-scale dependent ion dynamics in the nanocrystalline ternary fluoride providing a channel-like arrangement for some of the fluorine ions. This constraint of a crystal structure is a prerequisite for low-dimensional diffusion. Quasi 1D ionic transport has been proposed by Kannan *et al.*<sup>9</sup> based on impedance spectroscopy results on BaMgF<sub>4</sub> single crystals; ionic transport along the *c*-axis is reported to be much faster than that along the *b*-axis. Such low-dimensional hopping of the mobile charge carriers should become apparent as a characteristic signature in the dispersive regime of  $\sigma'(\nu)$  of the conductivity isotherms.<sup>18</sup> Here,  $\sigma'$  denotes the real part of the complex conductivity. Specifically, a relatively shallow frequency dependence  $\sigma'(\nu) \approx \nu^\kappa$  is expected for low dimensional ion conduction with the Jonscher exponents  $\kappa$  being (significantly) smaller than approximately 0.5.<sup>18</sup>

The conductivity isotherms shown in Fig. 3 are composed of four regimes. (i) At low frequencies (and sufficiently high temperatures and thus ion mobility) electrode polarisation (EP) effects show up owing to the pile-up of ions near the surface of the blocking Au electrodes applied. In many cases a step-wise decay of  $\sigma'$  is detected (see the two arrows in Fig. 3(b)). (ii) The polarisation regime passes over into a distinct conductivity plateau (P1) governing the isotherms at intermediate temperatures and low frequencies. If this plateau is identified with a bulk response, it reflects long-range ion transport and is called the dc-plateau. Moving to higher frequency a shallow dispersive regime with a weak frequency dependence shows up. It directly merges into a shallow second plateau (iii, P2) passing over in the final dispersive regime (iv) which can be approximated with a Jonscher power law (see above). The second plateau becomes clearer in the third heating run as

can be seen by the isotherms shown in Fig. 3(b). In that figure the temperature-dependent levels of the plateaus P1 and P2 on the ordinate are highlighted by filled circles. The same characteristics do also show up in the corresponding permittivity spectra presented in Fig. 5 and discussed below.

To analyse the conductivity data in terms of dimensionality effects we looked at the Jonscher exponents of the dispersive regime. At low temperatures the exponent  $\kappa$  takes values of approximately 0.75 (see Fig. 3(a) and (b)). Most likely, strongly correlated motion or spatially localized ones already influence  $\sigma'(\nu)$ . The prominent nearly-constant-loss phenomenon, see ref. 21 for an overview, being frequently related to caged dynamics in so-called asymmetric double well potentials, would lead to  $\kappa$  values close to one.

Most importantly, at higher temperatures, that is above 333 K, the exponent  $\kappa$  drops below 0.4 and less. As mentioned above, this gives evidence for a low dimensional transport process. As summarized in ref. 18, such low Jonscher exponents seem to be characteristic for 1D and 2D diffusion as is found in beta-alumina and other low-dimensional ion conductors.

In order to underpin the interpretation of  $\kappa$  as being an indicator of low-dimensional transport in BaMgF<sub>4</sub>, we compared the conductivity values of the two plateaus of our isotherms with the corresponding values of Kannan *et al.*<sup>9</sup> who carried out orientation-dependent measurements on single crystals. In the Arrhenius plot of Fig. 4 the  $\sigma'$  values of the first plateau P1 are shown, which have been read out from the isotherms of different heating runs. Heat treatment at elevated temperatures causes a continuous decrease of ion conductivity, which is presumably due to healing of defects and/or thermal equilibration. At the top of each heating cycle, the conductivity

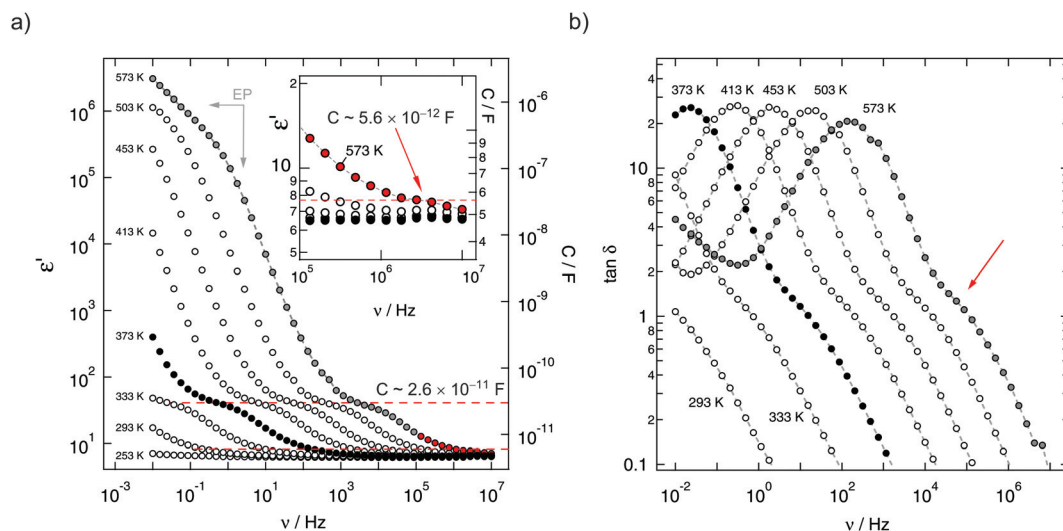


**Fig. 5** (a) Real part of the permittivity as a function of frequency showing two distinct plateaus with characteristic capacities for bulk conduction processes, see the horizontally drawn dashed lines. This is particularly illustrated in the inset; see the isotherm recorded at 573 K. (b) Plot of the dielectric loss,  $\tan \delta$ , versus frequency, likewise showing an additional peak as a shoulder in the spectra as indicated by the arrow. EP denotes contributions from electrode polarisation.

drops slightly, and when going back to lower temperature the slope of the dashed lines in Fig. 4(a) increases reflecting an increase of the corresponding activation energy  $E_A$ .

In order to explore possibly origins of this behaviour we recorded an X-ray powder pattern after heat treatment in the impedance cell, see the pattern at the top of Fig. 2(a). The remaining broad reflections do not indicate any significant grain growth. Therefore, local changes, that is a reduction of the concentration of defects, might be responsible for the change in conductivity rather than macroscopic ones. The amount of amorphous material seems to be somewhat reduced compared to the pattern directly recorded after mechanosynthesis of  $\text{BaMgF}_4$ .

Coming back to Fig. 4(a) the dashed lines represent fits with an Arrhenius law according to  $\sigma T_{P1,P2} \propto \exp(-E_A/(k_B T))$ ;  $k_B$  denoting Boltzmann's constant. Starting from 0.81 eV the activation energy  $E_A$  slightly increases to 0.88 eV after the sample has been exposed to 473 K for about 1 h inside the impedance cell. Interestingly, the values measured for the third run (cooling from 473 K to lower  $T$ ) coincide with those reported for ion conduction along the  $c$ -axis in  $\text{BaMgF}_4$  as reported by Kannan *et al.*<sup>9</sup> Along this axis, the  $\text{MgF}_6$ -octahedra are directly connected forming a low-dimensional diffusion pathway (see also Fig. 1). Ion conduction along the  $b$ -axis is indicated in Fig. 4(a) by a dashed line; in contrast to fast ion movement along the  $c$ -axis, ion transport is much slower.

Besides the conductivity values of the first plateau, those of the second one are also included in Fig. 4. The data points follow an activation energy of approximately 0.81 eV (3<sup>rd</sup> run, heating). Regarding absolute conductivity values, they are by about one order of magnitude larger than those reported for ion conduction along the  $c$ -axis in  $\text{BaMgF}_4$  single crystals.<sup>9</sup>

To illustrate the presence of a second conductivity plateau in another way, we also analysed the corresponding Nyquist plots which can be constructed when the real part of the impedance  $Z'$  is plotted vs. the imaginary part  $Z''$ . Exemplarily, data recorded at 473 K are shown in Fig. 4(c). The Nyquist curves are clearly composed of two overlapping semicircles reflecting the two plateaus (P1 and P2) of the  $\sigma(\nu)$  isotherms. With each heating run the intercepts (with the  $Z'$ -axis) of the two, slightly depressed semicircles shift towards higher impedances  $Z' \propto 1/\sigma'$  (Fig. 4(c)); this is, of course, also represented by the conductivities (see Fig. 4(a)).

The fact that the overall impedance response is composed of three different regions can be best seen in Fig. 4(b) that shows the Nyquist curve recorded at 573 K. While the spike at the lowest frequencies represent electrode polarisation, the two semicircles can be relatively well separated from each other. For comparison, the same two different dielectric responses can also be seen when the real part of the complex permittivity  $\epsilon'$  or the dielectric loss  $\tan \delta$  is plotted vs. frequency (see Fig. 5(a) and (b)). The response of  $\tan \delta$  obviously reveals a shoulder at higher frequencies; it is exemplarily indicated by the arrow in Fig. 5(b) and points to the second relaxation process P2.

In order to judge if and to which extent any grain boundary effects govern the low-frequency response, that is the P1 conductivity plateau, we looked at the corresponding capacities  $C_i$  ( $i = P1, P2$ ). From the  $\epsilon'(\nu)$  isotherms, it can be read out that the capacity  $C_{P2}$  of the high frequency response, corresponding to the second  $\sigma'$  plateau, is about 5.6(5) pF clearly proving bulk ion conduction. The response at lower frequencies, corresponding to the first conductivity plateau, is approximately given by  $C_{P1} = 26(2)$  pF. To our opinion, this value is

in between that for bulk and grain boundary response; we tend to interpret it as a bulk response which is already affected by the surface-influenced volume of our nanocrystalline sample.

Lastly, almost the same values for  $C_i$  can be determined from the Nyquist plots if two RC-circuits connected in series are simply used to analyse the complex plane data. According to the maximum condition  $\omega_{\max}RC = 1$ , with  $\omega_{\max} = 2\pi\nu$ , the capacities are 5(1) pF and 40(5) pF, respectively. Furthermore, the conductivities, calculated from the resistances  $R_{P1}$  and  $R_{P2}$  of the intercepts with the  $Z'$ -axis, confirm the values determined from the  $\sigma(\nu)$  isotherms (see the two lines in Fig. 3 connecting the filled circles of plateau P1 and P2, respectively). Thus, as mentioned above, compared with the results from BaMgF<sub>4</sub> single crystals, even after soft annealing of the freshly prepared sample in the impedance cell *in situ*, ion transport is somewhat enhanced in the nanocrystalline form (see (red) diamonds in Fig. 4(a)).

## Conclusions and outlook

Polycrystalline BaMgF<sub>4</sub> was successfully synthesized *via* a one-pot mechanochemical route. Apart from structural characterization by X-ray diffraction, <sup>19</sup>F MAS NMR spectroscopy was employed to directly track the local magnetic changes around the F spins. NMR indicates a reaction mechanism that initially involves the incorporation of MgF<sub>2</sub> into the cubic structure of BaF<sub>2</sub> which finally transforms into the desired product *viz* orthorhombic BaMgF<sub>4</sub>.

Conductivity spectroscopy and permittivity spectroscopy as well reveal two distinct ion transport processes. The associated capacities as estimated from the corresponding Nyquist plots may be interpreted as electrical responses originating from the bulk and grain boundary affected regions. Absolute conductivities of the two processes differ by a factor of approximately ten; this trend is in line with the corresponding activation energies of the two processes, 0.81 eV *vs.* 0.88 eV. Thus, from a microscopic point of view the underlying ion hopping processes might be very similar. If compared with previous measurements on single crystals of BaMgF<sub>4</sub>, ionic conductivity probed here resembles that being characteristic along the *c*-axis; ion dynamics along the *b*-axis is reported to be much slower.

Most importantly, if analysed in terms of Jonscher exponents, the frequency dependent conductivity measurements point to low-dimensional ionic conduction even in the nanocrystalline form of BaMgF<sub>4</sub>. Relatively small exponents have also been presented in the literature for, *e.g.*, sodium ion conduction in beta-alumina showing 2D diffusion.

In order to investigate the origin of the different conduction processes of our nanocrystalline material, the influence of sintering on both grain growth and ion dynamics will be the subject of further studies. These will also include <sup>19</sup>F NMR relaxometry in both the laboratory and in the rotating frame of reference to throw light on F ion dynamics taking place on different length scales.

## Acknowledgements

We thank B. Bitschnau for the x-ray diffraction measurements and Rietveld refinements as well as for valuable discussions. Moreover, we thank P. Bottke for his help with the NMR measurements and V. Pregartner for the assistance with sample preparation. Financial support by the Deutsche Forschungsgemeinschaft (DFG), Priority Programme SPP 1415, Crystalline Non-equilibrium Phases is greatly appreciated. Furthermore, we thank the DFG for access to the NMR and impedance spectrometers of the DFG Research Unit 1277, grant no. WI3600/2-1 and 4-1.

## Notes and references

- 1 V. Šepelák, A. Düvel, M. Wilkening, K. D. Becker and P. Heitjans, *Chem. Soc. Rev.*, 2013, **42**, 7507.
- 2 P. Heitjans and S. Indris, *J. Phys.: Condens. Matter*, 2003, **15**, R1257.
- 3 P. Heitjans, M. Masoud, A. Feldhoff and M. Wilkening, *Faraday Discuss.*, 2007, **134**, 67.
- 4 M. Wilkening, V. Epp, A. Feldhoff and P. Heitjans, *J. Phys. Chem. C*, 2008, **112**, 9291.
- 5 B. Ruprecht, M. Wilkening, S. Steuernagel and P. Heitjans, *J. Mater. Chem.*, 2008, **18**, 5452.
- 6 B. Ruprecht, M. Wilkening, A. Feldhoff, S. Steuernagel and P. Heitjans, *Phys. Chem. Chem. Phys.*, 2009, **11**, 3071.
- 7 A. Düvel, B. Ruprecht, P. Heitjans and M. Wilkening, *J. Phys. Chem. C*, 2011, **115**, 23784.
- 8 A. Düvel, S. Wegner, K. Efimov, V. Šepelák, P. Heitjans and M. Wilkening, *J. Mater. Chem.*, 2011, **21**, 6238.
- 9 C. V. Kannan, K. Shimamura, H. R. Zeng, H. Kimura, E. G. Villora and K. Kitamura, *J. Appl. Phys.*, 2008, **104**, 114113.
- 10 J. F. Scott, *Rep. Prog. Phys.*, 1979, **42**, 1055.
- 11 E. G. Villora, K. Shimamura, K. Sumiya and H. Ishibashi, *Opt. Express*, 2009, **7**, 12362; K. Shimamura, E. G. Villora, H. R. Zeng, M. Nakamura, S. Takekawa and K. Kitamura, *Appl. Phys. Lett.*, 2006, **89**, 232911; E. G. Villora, P. Molina, S. Álvarez, J. V. García-Santizo, M. O. Ramírez, K. Shimamura and L. E. Bausá, *J. Appl. Phys.*, 2010, **107**, 033106; Y. Ma, J. Chen, Y. Zheng and X. Chen, *Appl. Opt.*, 2012, **51**, 5432; T. E. Littleford, R. A. Jackson and M. S. D. Read, *Phys. Status Solidi C*, 2013, **10**, 153; L. Mateos, M. O. Ramírez, I. Carrasco, P. Molina, J. F. Galisteo-López, E. G. Villora, C. de las Heras, K. Shimamura, C. Lopez and L. E. Bausá, *Adv. Mater.*, 2014, **24**, 1509.
- 12 S. Sinharoy, H. Buhay, M. H. Francombe, W. J. Takei, N. J. Doyle, J. H. Rieger, D. R. Lampe and E. Stepke, *J. Vac. Sci. Technol., A*, 1991, **9**, 409.
- 13 R. M. Kowalczyk, T. F. Kemp, D. Walker, K. J. Pike, P. A. Thomas, J. Kreisel, R. Dupree, M. E. Newton, J. V. Hanna and M. E. Smith, *J. Phys.: Condens. Matter*, 2011, **23**, 315402; M. Body, G. Silly, C. Legein and J.-Y. Buzaré, *J. Phys. Chem. B*, 2005, **109**, 10270.

- 14 U. Groß, S. Rüdiger and E. Kemnitz, *Solid State Sci.*, 2007, **9**, 838.
- 15 S. Fujihara, S. Ono, Y. Kishiki, M. Tada and T. Kimura, *J. Fluorine Chem.*, 2000, **105**, 65.
- 16 P. D. Belsare, C. P. Joshi, S. V. Moharil, S. K. Omanwar, P. L. Muthal and S. M. Dhopte, *J. Alloys Compd.*, 2008, **464**, 296.
- 17 S. W. Kim, H. Y. Chang and P. S. Halasyamani, *J. Am. Chem. Soc.*, 2010, **132**, 17684.
- 18 D. L. Sidebottom, *Phys. Rev. Lett.*, 1999, **83**, 983.
- 19 A. Düvel, M. Wilkening, R. Uecker, A. Feldhoff and P. Heitjans, *Phys. Chem. Chem. Phys.*, 2010, **12**, 11521.
- 20 F. Gintl, *Z. Anorg. Allg. Chem.*, 1997, **623**, 705.
- 21 K. Funke, C. Cramer and D. Wilmer, in *Diffusion in Condensed Matter – Methods, Materials, Models*, ed. P. Heitjans and J. Kärger, Springer, Berlin, 2nd edn, 2005, ch. 21, pp. 857–893.

#### **5.4 A review on mechanochemically synthesized F-ion conductors**

The results and the conclusions that were drawn for the individual materials treated in this work were not only summarized in this thesis, but also in a short review-article that is given as a manuscript below. It is considered as a brief but comprehensive publication that thoroughly compares the obtained results with literature data and thus provides an overview and orientation in the field of mechanochemically synthesized F-ion conductors. The article further contains information about the applications of solid state NMR relaxometry and broadband impedance spectroscopy to characterize diffusion processes in solid ion conductors and outlines the analysis of the acquired data. In addition, MAS NMR spectroscopy is presented as a powerful, complementary technique to X-ray diffraction for the structural investigation of inorganic solids.



---

M1: (pp. 85-98)

**Mechanochemically Synthesized Fluorides:**

**Local Structures and Ion Transport**

F. Preishuber-Pflügl and M. Wilkening,

*Submitted, 2016.*



# Mechanochemically Synthesized Fluorides: Local Structures and Ion Transport

Florian Preishuber-Pflügl and Martin Wilkening

Institute for Chemistry and Technology of Materials, DFG-SPP 1415 ,  
Graz University of Technology, Stremayrgasse 9/Z4, 8010 Graz, Austria.  
preishuber-pfluegl@tugraz.at

The performance of new sensors or advanced electrochemical energy storage devices strongly depends on the active materials chosen to realize such systems. In particular, their morphology may greatly influence overall macroscopic properties. Many times, however, current limitations in classical ways of chemical preparation routes hamper the development of materials with tailored properties. Fortunately, such hurdles can be overcome by mechanochemical synthesis. The versatility of mechanosynthesis allows the provision of compounds that are not available through common synthesis routes. Mechanical treatment of two or three starting materials in high-energy ball mills enables the synthesis not only of new compounds but also of nanocrystalline materials with unusual properties such as enhanced ion dynamics. Fast ion transport is of crucial importance in electrochemical energy storage. Importantly, mechanosynthesis also provides access to metastable phases that cannot be synthesized by conventional solid state synthesis. Ceramic synthesis routes often yield the thermally, *i.e.*, thermodynamically, stable products rather than metastable compounds. In this review we report about mechanochemical synthesis of nanocrystalline fluorine ion conductors that serve as model substances to understand the relationship between local structures and ion dynamics. While ion transport properties were complementarily probed via conductivity spectroscopy and nuclear magnetic relaxation, local structures of the phases prepared were investigated by high-resolution  $^{19}\text{F}$  NMR spectroscopy carried out at fast magic angle spinning. The combination of nuclear and non-nuclear techniques also helped us to shed light on the mechanisms controlling mechanochemical reactions in general.

## Introduction

A chemical reaction which is induced by the absorption of mechanical energy is called a *mechanochemical* reaction. It constitutes its own class of chemical synthesis routes. Chemical reactions are usually driven by other sources of energy such as heat, light or by the difference in electrochemical potentials of the materials involved, *i.e.*, through electric energy.

Mechanochemistry offers access to nanocrystalline compounds and metastable phases that are often characterized by non-equilibrium structures. In many cases these materials cannot be obtained through conventional approaches such as solid state synthesis which require high sintering temperatures, for example. Compared to other preparation routes, mechanosynthesis, *e.g.*, when carried out in high-energy planetary mills, represents a highly versatile way of synthesis that benefits from its facile realization and so-called one-pot conditions. This advantages as well as the possibility to prepare materials with yet inaccessible properties led to a rapid increase of applications of

mechanochemical techniques. In particular, this growing interest is highlighted by the increasing number of publications reporting on mechanochemical reactions as well as by several comprehensive reviews that appeared over the last couple of years.<sup>1-3</sup> While recent reviews focused on, *e.g.*, the synthesis of non-equilibrium oxides, the present one puts emphasis on the preparation of inorganic, nanocrystalline fluorides, *i.e.*, ternary and quaternary ionic conductors, in particular.

Besides the effect of nanostructuring, the impact of mechanical stress yields materials with a high concentration of defects and a large volume fraction of so-called interfacial regions anticipated to be structurally disordered. In the case of  $\text{Li}^+$  and  $\text{F}^-$  ionic conductors defects are necessary to facilitate both self-diffusion and long-range ion transport. From an application point of view, fast ion conductors are urgently needed to develop powerful electrochemical sensors or energy storage devices that may also take advantage of fluoride as the main ionic charge carrier. In this regard, mechanosynthesis has also been employed for the

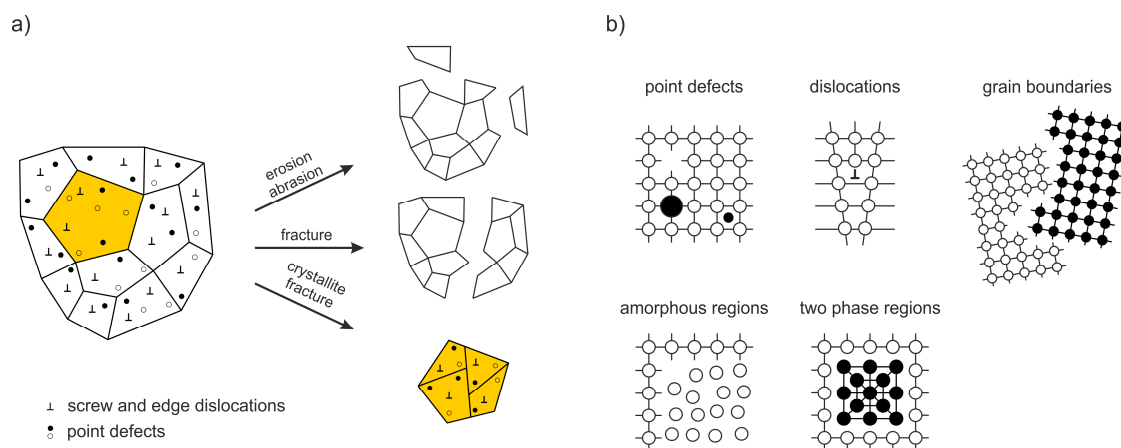


**Fig. 1:** a) What happens during mechanical treatment? An overview of the complex processes simultaneously taking place during high-energy ball milling. Most importantly, defects are introduced that will significantly govern the properties of the final nanocrystalline and structurally disordered product. b) Possible defect structures generated in crystalline solids treated mechanically.

direct synthesis of current electrode materials for lithium-ion batteries.<sup>4-7</sup>

For the characterization of materials synthesized via mechanochemical routes, nuclear magnetic resonance (NMR) techniques and impedance spectroscopy have proven as powerful tools to investigate both ion dynamics on short-range as well as long-range length scales. Considering local structures, high-resolution solid-state NMR under the condition of very fast magic angle spinning (MAS) can be used to follow possible microstructural changes taking place as a function of milling time.

### Mechanochemically Induced Changes: What Happens During High-Energy Ball milling?

First results on mechanochemically induced reactions were reported by Wilhelm Ostwald, Michael Faraday and Carey Lea.<sup>8,9</sup> Lea carried out systematic investigations on silver halides upon exposure to light or mechanical force, which finally led to the differentiation of mechanochemistry as a separate branch in chemical synthesis. Initially this phenomenon was discovered in the area of inorganic, solid state chemistry, but applications of this method spread on many other fields of applications including biomaterials, metal organic frameworks, catalysts, organics and pharmaceuticals, in particular.<sup>1, 8, 10</sup>

In terms of solid state chemistry, such as the synthesis of nanocrystalline fluoride ion conductors under dry conditions, the goings-on during mechanical treatment can affect the starting material

in two different ways: (i) altering the defect structure without any chemical reaction induced, *i.e.*, conserving the initial crystal structure and (ii) changing the crystal chemical structure by chemical reactions, *i.e.*, inducing a structural conversion by breaking and forming chemical bonds.

Figure 1 provides an overview of the possible macroscopic and microscopic structural changes taking place during severe high-energy ball milling.<sup>11</sup> Shear, friction and impact forces lead to abrasion and fracture of the solid particles into smaller ones. This drastic reduction in crystallite size — usually the mean crystallite size reached after some hours of milling is in the order of 20 nm — results in a high ratio between the remaining bulk material and the structurally disordered surface-near regions.<sup>12</sup> The bulk regions of a mechanothesized phase, however, are also expected to differ from those of the starting material since mechanical impact does not only introduce structural disorder in the boundary layers but also generates defects and dislocations in the interior of the small crystallites.

From the point of view of ion dynamics those ions which are located in or near these interfacial regions often move much faster than those in the bulk material. In favourable cases the quickly jumping ions can be revealed by NMR line shape studies (Figure 2).<sup>13</sup> In particular, this has been demonstrated for single-phase nanocrystalline  $\text{Li}_2\text{O}$  and the two-phase composites  $\text{Li}_2\text{O}:\text{X}_2\text{O}_3$  with  $x = \text{Al}, \text{B}$ .<sup>14-16</sup> In the latter, the compaction of two nanocrystalline materials, an ion conductor and an ionic insulator, lead to an interfacial network of homo-contacts ( $\text{Li}_2\text{O}:\text{Li}_2\text{O}$ ) and hetero-contacts

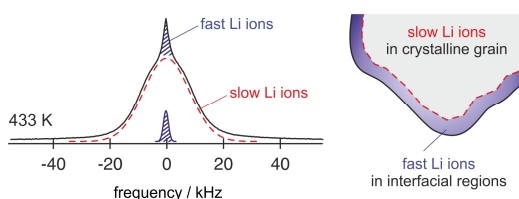


**Fig. 2:**  ${}^7\text{Li}$  NMR spectrum of nanocrystalline  $\text{Li}_2\text{O}$  prepared by high-energy ball milling. The line is composed of two contributions reflecting the slow and the fast ions in either the bulk or in/near the interfacial regions. Figure taken from Ref. 13.

( $\text{Li}_2\text{O}:\text{X}_2\text{O}_3$ ), see Figure 3 for comparison. Compared to the situation in the bulk regions of nano- $\text{Li}_2\text{O}$  the two-component interfacial regions provide fast diffusion pathways in their vicinity.<sup>14</sup> The same is anticipated in other dispersed ion conductors such as  $\text{LiI}-\text{Al}_2\text{O}_3$  which was the first example of its class.<sup>17</sup> Other nanostructured ion conductors<sup>18, 19</sup> also benefit from so-called non-trivial size effects that are based on the formation of space charge zones<sup>20</sup> which in some cases influence the dynamic properties of the whole nanocrystallite, *i.e.*, its interior regions. Maier introduced the term artificial ion conductor to describe the electrochemical situation created in nano-ionics.<sup>21, 22</sup>

Apart from ion dynamics, the element distribution in grain boundary regions might be different from that in the bulk state. In particular, this holds for non-equilibrium compounds as described by Šepelák et al.<sup>2</sup> the inhomogeneous distribution of cations in the grain boundaries is referred to mechanical treatment. The authors presented detailed analysis techniques for such non-equilibrium phenomena in oxides.

The second aspect of mechanochemistry is the direct conversion of the reagents into the desired product without the need of any further processing or purification steps. As mentioned above, it is feasible to prepare materials which are not accessible through conventional synthesis techniques such as thermochemistry, precipitation techniques or sol-gel methods. Worth mentioning, such metastable phases allow to overcome miscibility gaps giving rise to solid-solutions being characterized by an enhanced concentration of vacancies, interstitials or other defects that are necessary to enable high ionic conductivities.<sup>23</sup>

The underlying reaction mechanism of a mechanochemical synthesis is still under discussion. Besides the various microstructural changes taking

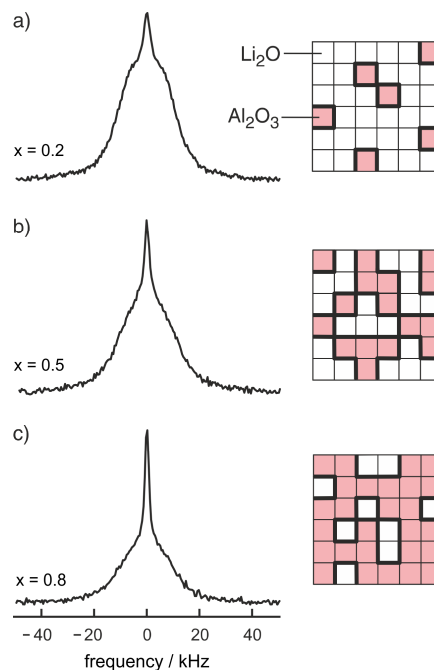


**Fig. 3:**  ${}^7\text{Li}$  NMR spectra of the nanocrystalline composite  $x\text{Li}_2\text{O}:(1-x)\text{Al}_2\text{O}_3$ , a)  $x = 0.2$ , b)  $x = 0.5$ , and c)  $x = 0.8$ . The more hetero-contacts per formula unit of  $\text{Li}_2\text{O}$  are formed, the larger the fraction of the motionally narrowed NMR line superimposing the broad main signal. Fig. adapted from Ref. 13.

place, localized reactions induced by heat and pressure are anticipated to lead to the final conversion of the starting material. In contrast to any high temperature solid state reaction, where the entire material is heated to a certain temperature, a mechanochemical reaction is thought to occur at localized spots where the material is stressed by the milling tools. Boden, Tabor and Yoffe proposed a 'hot-spot theory' that suggests temperatures as high as 1000 K for a time period of  $10^{-4}$  to  $10^{-3}$  s due to friction at surfaces of about  $1 \mu\text{m}^2$ .<sup>24-26</sup> The magma-plasma model predicts even higher temperatures of up to  $10^4$  K and a molten-like state of the reactants in the impact zone of the particles.<sup>27</sup>

The common finding in both theories is a localized development of thermal energy that promotes the solid state reactions. As the reactants are thoroughly mixed on the nm-scale, the diffusion pathways between the reactants are some orders of magnitude smaller compared to  $\mu\text{m}$ -sized grains. For such a localized reaction, the energy delivered by mechanical treatment might be sufficient to completely convert the starting materials into a new product. As an example, for the synthesis of  $\text{BaMgF}_4$ , as is presented below, a quantitative reaction in a planetary ball mill required extremely high

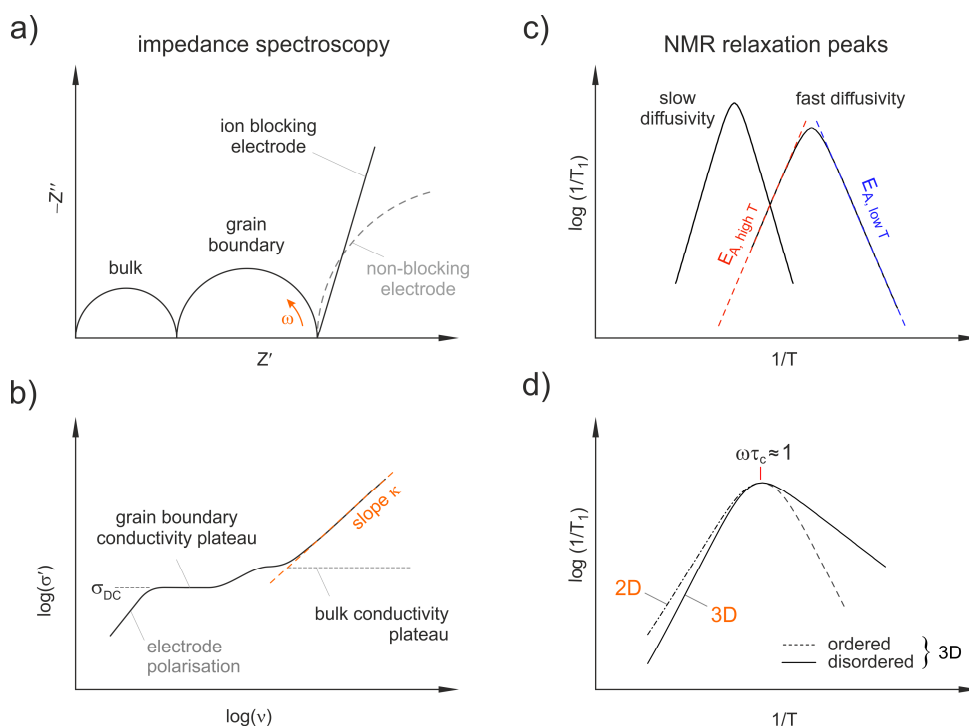


**Fig. 4:** Overview of important representations of impedance spectroscopy and solid state NMR data. a) Nyquist plot of the real part vs the imaginary part of the complex impedance. In the ideal case electrical responses of bulk and grain boundary regions can be distinguished; electrode effects are expected to show up at low frequencies. A spike at low frequencies results from the piling up of ions at the blocking electrode interface; conducting electrodes usually appear as large semicircles. b) The conductivity isotherm reveal the same features: at the highest frequencies a disperse regime shows up that includes forward-backward jumps. Each plateau reflects an individual transport process. c) Arrhenius plot of the NMR spin-lattice relaxation rate  $1/T_1$ : the higher the diffusivity the more the peak is sifted towards lower  $T$ . The flanks yield activation energies reflecting local ( $E_{A, low}$ ) and long-range ion dynamics ( $E_{A, high}$ ). d) Structural disorder results in asymmetric rate peaks with a lower slope in the low- $T$  regime. Dimensionality effects influence the NMR rates at higher temperatures only.

rotational speeds.<sup>28</sup> The fact that the overall temperature inside the milling beaker is much lower compared to high temperature solid state methods represents a clear advantage. At low temperatures the transformation of the products into thermodynamically stable phases is suppressed; for example, this concerns phase separations of usually immiscible solids. Hence, mechanochemistry enables indeed a powerful method to prepare highly metastable, *i.e.*, non-equilibrium compounds.

#### Characterization Techniques: X-Rays, Spins, Charge Carriers

For the characterization of (nano-)crystalline materials, diffraction techniques such as X-ray powder diffraction (XRPD) are commonly employed to determine the crystal structures. Mechanochemically synthesized materials, however, often show patterns that deviate from single crystalline or coarse grained materials. Broadening of the reflections due to extremely small mean crystallite sizes

leads to overlapping of the reflections or hides impurities and secondary phases. In addition, the signals can be shifted because of variations of the mean lattice parameters. Moreover, they can show different intensities which complicates a certain determination of the product. The milling process may also yield amorphous fractions lacking in periodicity in order that they cannot be identified by X-ray diffraction methods.

To overcome the drawbacks of X-ray diffraction, solid state NMR is the method of choice to uncover amorphous components and to collect information on local magnetic and electric fields at the nuclear sites. In particular, NMR is able to determine polyhedra distortions being a result of mechanical impact. In general, local distortions as well as outspread structural disorder can also be regarded as a metastable state of the product obtained. <sup>19</sup>F NMR benefits from the excellent receptivity of the fluorine nuclei. The good sensitivity as well as fast spin-lattice relaxation of the <sup>19</sup>F nuclei due to relatively strong dipole-dipole interactions results in

short acquisition times further underlining the advantages of the  $^{19}\text{F}$  NMR spectroscopy. In order to achieve high resolution in the solid state magic angle spinning (MAS) is applied. With current NMR probes spinning speeds as high as 100 kHz are available. Since NMR spectroscopy senses the magnetic environment of each nucleus it is also applicable to amorphous compounds (see below). Thus, it is a valuable tool to help identify by-products or impurities that remain unresolved or as such invisible by XRPD. Fortunately, MAS NMR does not require special sample preparation methods; air sensitive materials can be filled into the desired rotors using a drybox with inert atmosphere. Fluorine NMR, in particular, benefits from a very broad chemical shift range with the result that the individual signals can be well distinguished and, later, assigned to the crystallographic positions.

Besides structural characterisation via XRPD and NMR on both the macroscopic length scale and the angstrom lengths scale, ion transport properties of mechanosynthesized compounds are of particular interest since they may be largely different from those of their coarse-grained counterparts. Taken together, broadband impedance spectroscopy and solid-state time-domain NMR techniques are powerful tools that enable a complementary characterization of ion dynamics by sensing the hopping processes on different time scales. In terms of jump rates the accessible dynamic window ranges from the Hz to the GHz regime

Complex conductivities and dielectric permittivities, if measured over a wide frequency range, contain valuable information on ion hopping dynamics taking place on different length scales. In general, average hopping barriers are available from variable-temperature experiments when analysing the results in the frame of the law of Arrhenius, *i.e.*, by plotting, *e.g.*,  $\log(\sigma' T)$  vs the inverse temperature  $1/T$ ;  $\sigma'$  denotes the real part of the complex conductivity. Nyquist diagrams, which are obtained when the real part ( $Z'$ ) of the complex impedance is plotted vs the imaginary part ( $Z''$ ), and the analysis of modulus peaks  $M''$  are helpful to distinguish bulk from grain boundary contributions to the total conductivity. Of course from the various representations of impedance data (see Figure 4) electrical relaxation rates can be deduced that can be used to compare with results from other micro- and macroscopic techniques.

In many cases NMR relaxometry and NMR exchange spectroscopy are able to complement broadband impedance studies. For example, time-

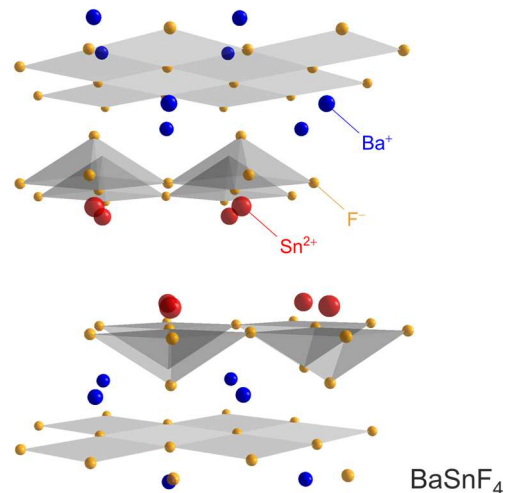
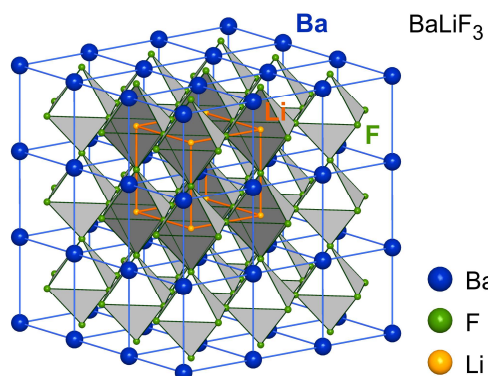


Fig. 5: Crystal structure of layer-structured  $\text{BaSnF}_4$  which belongs to the fastest F anion conductors known.

domain NMR spin-lattice relaxation measurements,<sup>29, 30</sup> if performed in the so-called low- $T$  range of NMR relaxometry, are sensitive to short-range ion dynamics that are usually accessed by AC impedance spectroscopy carried out at sufficiently high frequencies. This regime in NMR relaxometry is characterized by jump rates  $1/\tau$  that are much lower than the Larmor frequency applied to carry out the experiment. If we assume an irregularly formed potential landscape the jumping ion is exposed to, the method senses local jumps of the ions between neighbouring sites in the crystal lattice connected by low energy barriers. In this regime the relaxation rate is also sensitive to correlation effects such as structural disorder and Coulomb interactions of the hopping ions.<sup>29, 31</sup>

At higher temperatures, this is the regime where the mean jump rates exceeds the angular Larmor frequency  $\omega_0$ , the spin-lattice relaxation rate is sensitive to long-range ion dynamics. This is because during the time interval  $1/\omega_0$  the ions perform many jumps that can be sampled. These hops may also include jump processes where the ions have surmount higher energy barriers. Provided all diffusion processes present contribute to the spin-lattice relaxation rate, the activation energy deduced from measurements in this  $T$ -range is comparable with that of DC conductivity measurements. In the case of low-dimensional diffusion, the NMR rates are expected to depend on the Larmor frequency applied. Moreover, the slope of the respective flank is lower than in the case of 3D motion



**Fig. 6:** Crystal structure of the inverse perovskite  $\text{BaLiF}_3$ , the smaller Sr atoms in  $(\text{Ba,Sr})\text{LiF}_3$  occupy the same sites as Ba. This leads to lattice contraction and local distortions affecting fluorine ion dynamics. Fig. adapted from Ref. 54.

for which no frequency dependence should be observed.<sup>29, 32</sup>

If dynamically distinct processes are stepwise activated with increasing temperature, NMR is able to identify these: if widely separated on the dynamic time window they should show up as multiple relaxation rate peaks in an Arrhenius diagram.<sup>33</sup> The maxima allow an almost model-independent estimation of mean jump rates by means of the maximum condition linking  $\omega_0$  and  $1/\tau$ :  $\omega_0\tau \approx 1$ .<sup>29</sup> A thorough analysis, however, would require a specific relaxation model to interpret the data further, *e.g.*, in terms of diffusion pathways the ions chose. As mentioned above, if the number density of spins in the interfacial regions is large enough, as it is the case for nanocrystalline ceramics, NMR is able to separately probe ion dynamics of the ions residing in or near these zones.

### Applications in Electrochemical Energy Storage

The aforementioned aspects of mechanochemistry makes it a highly promising method to prepare materials useful in electrochemical energy storage, in particular. Besides electrochemical stability, ionic conductivity belongs to the key parameters of a good solid electrolyte. The electrolyte is the region that should guarantee extremely fast ion exchange between the two electrodes of a battery.

The same applies to electrode materials as well, both fast ion dynamics and fast insertion kinetics crucially determine the performance of a battery, *i.e.*, to accept (ultra-)high charging rates being necessary for today's portable electronics or electric

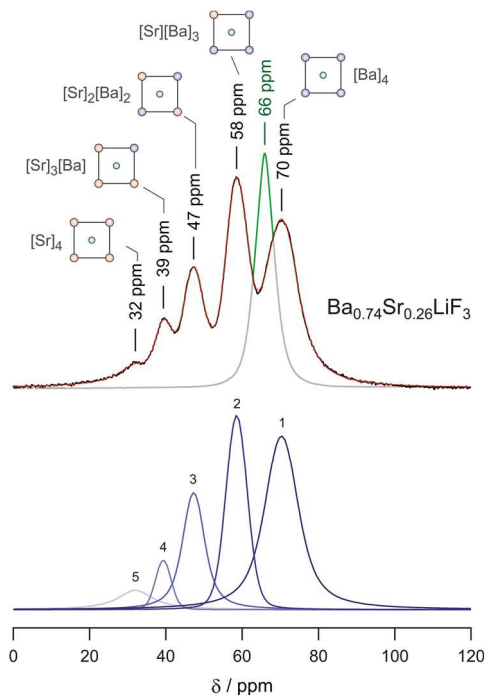


**Fig. 7:**  $^{19}\text{F}$  MAS NMR spectrum of  $\text{Ba}_{0.74}\text{Sr}_{0.26}\text{LiF}_3$  revealing the individual NMR signals of the different environments of the F ions. Since in  $\text{BaLiF}_3$  the F sites are magnetically equivalent only a single signal shows. Depending on the number of Sr atoms in the direct vicinity of the  $^{19}\text{F}$  nucleus the chemical shift ranges from 70 to 32 ppm. Reprinted from Ref. 51.

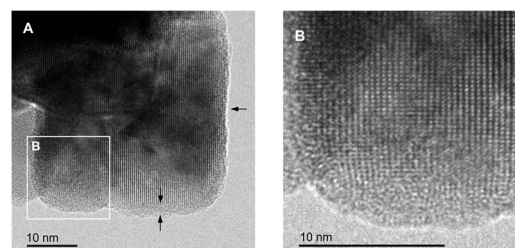


**Fig. 8:** High-resolution TEM image of nanocrystalline  $(\text{Ba,Sr})\text{LiF}_3$  directly obtained by high-energy ball milling. The enlargement (B) reveal structurally disordered regions at the grain boundaries. Reprinted Ref. 51.

vehicles, for example. At last, facile and environmentally friendly preparation methods are needed abandoning hazardous chemicals.

As an example, electrode materials for rechargeable Li-ion batteries with aprotic liquid electrolytes were prepared by mechanochemical synthesis by Liao *et al.*, who tested  $\text{LiFe}_2\text{F}_6$  as an intercalation compound.<sup>5</sup> A similar approach to use  $\text{Na}_3\text{FeF}_6$  as cathode material in Na-ion batteries was reported by Shakoor and co-workers.<sup>4</sup> In terms of solid state batteries, the fast  $\text{Li}^+$  conducting electrolyte  $\text{Li}_7\text{P}_3\text{S}_{11}$  can be obtained through ball milling of

$\text{Li}_2\text{S}$  and  $\text{P}_2\text{S}_5$  followed by a soft annealing step to yield a crystalline product.<sup>6,7</sup>

Research on anion conduction in solids has a long tradition; it was initiated by an experiment of Michael Faraday in 1834. In his experiments Faraday observed electrical conductivity of lead fluoride ( $\text{PbF}_2$ ) at high temperatures. Around 1975 Schoonman, Kennedy, Hunter and others<sup>34</sup> report on first results to prepare solid-state electrochemical cells based on F ion chemistry. The large change in free enthalpy in reactions of fluorine with metals and the potentially high voltage in a battery encouraged researchers to prepare a rechargeable cell based on F ion chemistry in 2011.<sup>35</sup> One significant drawback of the system, however, was the low mobility of F ions at ambient temperature which triggered research to develop fast solid fluorine ion conductors.

### Case studies: Ion diffusion in mechano-synthesized complex fluorides

The small size and the single negative charge enable F anions to quickly move in solids. To date,  $\text{MF}_2\text{-SnF}_2$  ( $\text{M} = \text{Pb}, \text{Ba}$ ) systems are considered as the fastest  $\text{F}^-$  conductors.<sup>36, 37</sup> This is attributed to their layered structure which is the consequence of ordering effects of the cations, see Figure 5. Cation ordering is caused by the steric demand of the unpaired electrons of the Sn atoms.<sup>38, 39</sup>  $\text{PbSnF}_4$  and

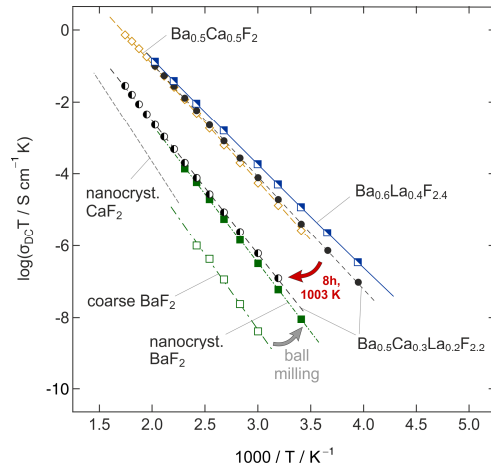


**Fig. 9:** Overview of the ionic conductivities of several  $\text{BaF}_2$ -derived compounds. Ball milling of coarse-grained  $\text{BaF}_2$  yields a nanocrystalline sample which shows a conductivity that is almost two orders of magnitudes higher compared to the non-milled material. Ion conductivity can be further improved by mixing  $\text{BaF}_2$  and  $\text{CaF}_2$  yielding a non-equilibrium phase taking advantage of local disorder and strain introduced when missing cations of different sizes. The highest values are found for  $\text{Ba}_{0.6}\text{La}_{0.4}\text{F}_{2.4}$ , which was studied by NMR relaxometry in detail, see Fig. 6.

$\text{BaSnF}_4$  can be prepared by means of solid state synthesis at high temperatures;<sup>40-42</sup> alternatively, the ternary fluorides can be synthesized by mechanochemical means as well.<sup>42-45</sup> In the case of  $\text{BaSnF}_4$ , the highest conductivity was reached if a mechanochemical milling route was chosen.<sup>42, 45</sup> The same holds for  $\text{SnF}_2$ : if treated in a high-energy ball its

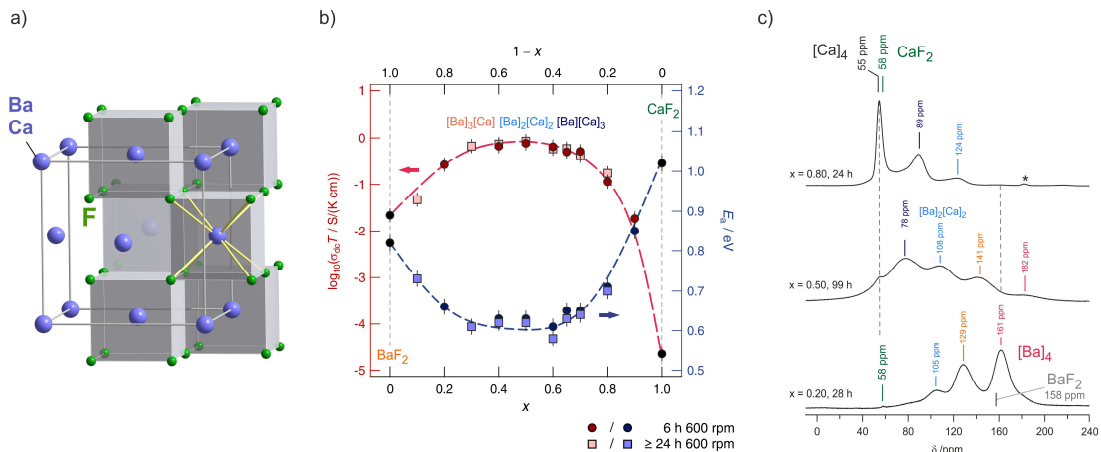


**Fig. 10:** a) Cubic crystal structure of  $(\text{Ba},\text{Ca})\text{F}_2$ . b) Variation of conductivity and activation energies for  $\text{Ba}_x\text{Ca}_{1-x}\text{F}_2$  samples mechanically prepared by milling the starting materials for 6 h and  $> 24$  h in a planetary mill. c)  $^{19}\text{F}$  MAS spectra revealing the local magnetic environments sensed by the F anions. The maximum in structural disorder is reached if  $x = 0.5$ . b,c) reprinted from Ref. 52.

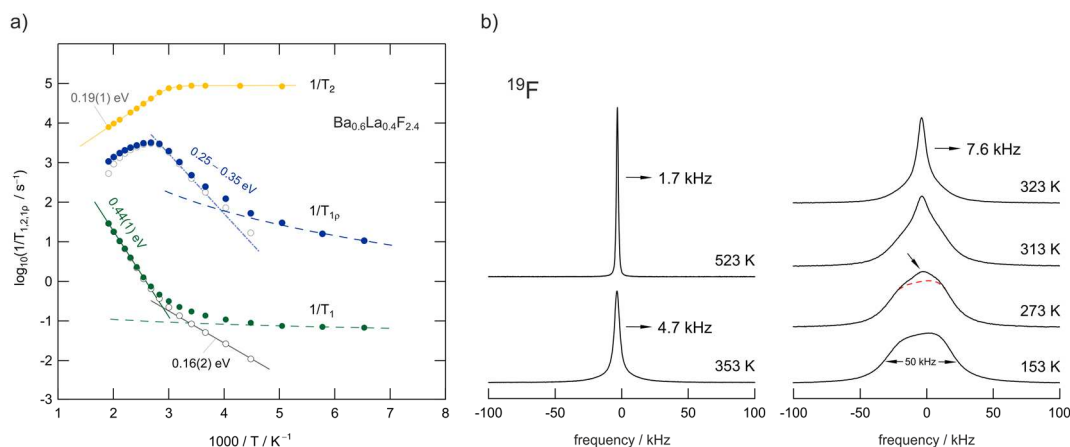


**Fig. 11:** a) F anion dynamics in  $\text{Ba}_{0.6}\text{La}_{0.4}\text{F}_{2.4}$  as seen via NMR relaxometry. The rates  $1/T_1$  and  $1/T_{1p}$  are sensitive to different ionic motions. The same holds for  $T_2$  which refers to the transversal decay of magnetization. Most importantly, the  $1/T_{1p}(1/T)$  peak can be understood as a superposition of a range of sub-peaks that reflect dynamically distinct diffusion processes occurring in the same temperature range. Presumably, the distribution of activation energies found, *i.e.*, the heterogeneous dynamics seen, results from local structural disorder introduced by mixing the  $\text{Ba}^{2+}$  and  $\text{La}^{3+}$  cations that differ in size and charge. b)  $^{19}\text{F}$  NMR lines of for  $\text{Ba}_{0.6}\text{La}_{0.4}\text{F}_{2.4}$ . At low temperatures, the exchange between the individual F ion positions in the crystal is ‘frozen’ in so that the different environments appear as a superposition of several processes comparable to the relaxation data in Fig. 6. Figure taken from Ref. 49.

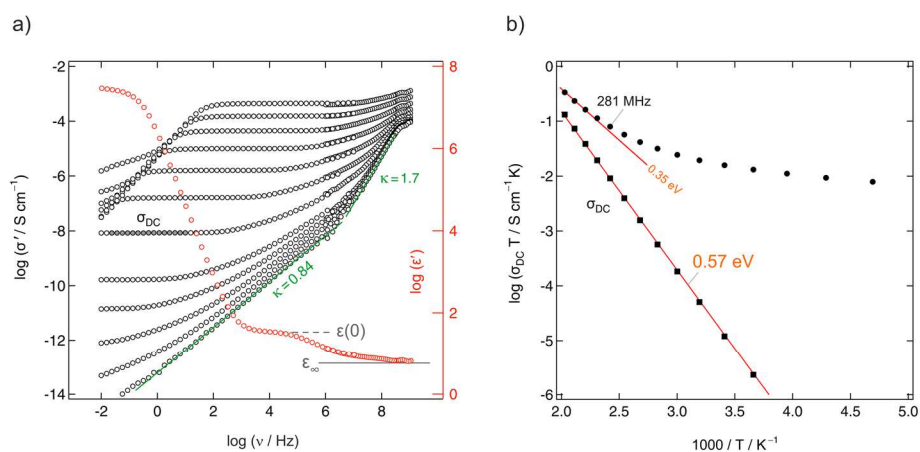


**Fig. 12:** a) Conductivity isotherms of  $\text{Ba}_{0.6}\text{La}_{0.4}\text{F}_{2.4}$  measured at frequencies ranging from 10 mHz up to 3 GHz. At frequencies above 100 MHz the individual isotherms collapse on a high frequency-plateau that show localized motions of the mobile charge carriers. The ions perform forward-backward jumps due to the short time scale at such frequencies. The chemical environment cannot adjust as fast and the process is almost independent of temperature. b) Arrhenius diagram highlighting DC and AC conductivities determined from data of the real part of the conductivity ( $\sigma'$ ) in the DC regime and at 281 MHz. The latter frequency is similar to the NMR Larmor frequency used to acquire the relaxation rates. Figure taken from Ref. 49.

conductivity can be increased by almost two orders of magnitude.<sup>46</sup>

Unfortunately,  $\text{SnF}_2$ -based fluorides are highly reactive, *i.e.*, unstable under electrochemical conditions complicating practical applications. Metals from the early groups of the periodic table are considered as more stable and usually possess only one oxidation/reduction state. Usually, the conductivity

of these metal fluorides in the form of single crystals or polycrystalline materials is relatively low. It can be enhanced, however, by changing the morphology of the materials, *e.g.*, via nanostructuring including both bottom-up and top-down approaches such as milling.<sup>47</sup>

In order to increase the number of defects aliovalent doping can be used to facilitate ion dynamics. As an example, mixtures of  $\text{BaF}_2$  and  $\text{LaF}_3$  have

been extensively studied over the past years.<sup>23, 35, 48, 49</sup> SrF<sub>2</sub> represents another substituent to manipulate ion transport in LaF<sub>3</sub><sup>50</sup>; to the best of our knowledge, such samples have, however, not been prepared mechanochemically as yet. In the following we will present case studies<sup>47, 49, 51-53</sup> including iso- and aliovalent ion-mixed compounds such as Ba<sub>1-x</sub>Sr<sub>x</sub>LiF<sub>3</sub>, Ba<sub>1-x</sub>Ca<sub>x</sub>F<sub>2</sub> and Ba<sub>1-x</sub>La<sub>x</sub>F<sub>2+x</sub>. Special emphasis will be put on the interplay of (local) structural effects with hopping ion dynamics. Whenever possible comparisons between mechano-synthesized and conventionally prepared materials are drawn.

### The Inverse Perovskite (Ba,Sr)LiF<sub>3</sub>

Joint milling of cubic BaF<sub>2</sub> and LiF results in phase BaLiF<sub>3</sub> crystallizing with the inverse perovskite structure (Figure 6). If BaF<sub>2</sub> is partially replaced by SrF<sub>2</sub> a mixed compound is formed, Ba<sub>1-x</sub>Sr<sub>x</sub>LiF<sub>3</sub>, (*x* can reach values of up to 0.3) that decomposes at elevated temperatures (393 K). Thus, it cannot be prepared by thermochemical routes. Above *x* > 0.32, X-ray reflections of pure BaF<sub>2</sub> and SrF<sub>2</sub> appear in the X-ray pattern indicating the upper limit of miscibility. Interestingly, a comparative XRPD and <sup>19</sup>F NMR study showed that the mechanochemical reaction proceeds stepwise, starting with the formation of BaLiF<sub>3</sub> with subsequent incorporation of Sr<sup>2+</sup> into the ternary fluoride.<sup>51</sup> <sup>19</sup>F MAS NMR turned out to be extremely helpful to reveal the local chemical environments of the F nuclei and to unravel the formation mechanism of the quaternary compound.

As an example, in Figure 7 the <sup>19</sup>F MAS NMR spectrum of mechano-synthesized Ba<sub>0.74</sub>Sr<sub>0.26</sub>LiF<sub>3</sub> is shown. Whereas Sr-free BaLiF<sub>3</sub> is characterized by a single NMR line,<sup>54</sup> that of earth-alkaline mixed Ba<sub>0.74</sub>Sr<sub>0.26</sub>LiF<sub>3</sub> is composed of 5 signals representing the different [Sr]<sub>*a*</sub>[Ba]<sub>*b*</sub> configurations formed (*a*+*b* = 4, *a*,*b* ∈ ℕ ∪ [0]). Note that in the inverse perovskite structure Ba- and Sr-ions occupy the corner-positions of the cubic unit cells. The face centred fluorine ions span octahedra that host the lithium ions. The more Sr ions reside in the direct vicinity of <sup>19</sup>F the more the isotropic NMR chemical shift value δ<sub>iso</sub> is shifted towards positive ppm values as is illustrated in Figure 7. As an example, for the [Sr]<sub>4</sub> environments in Ba<sub>0.74</sub>Sr<sub>0.26</sub>LiF<sub>3</sub> δ<sub>iso</sub> = 32 ppm is obtained. The areas under the NMR lines, which can be well resolved at spinning speeds as high as 60

kHz, reveal the cation distribution in Ba<sub>0.74</sub>Sr<sub>0.26</sub>LiF<sub>3</sub>.<sup>51</sup>

Since Sr<sup>2+</sup> is smaller than Ba<sup>2+</sup> its incorporation into the BaLiF<sub>3</sub> lattice leads to a reduction of the lattice constant with increasing Sr content. Hence, the formation of Ba<sub>1-x</sub>Sr<sub>x</sub>LiF<sub>3</sub> can be followed by the shift of the XRPD reflections of BaLiF<sub>3</sub> towards larger diffraction angles. The variations in chemical environments for each fluorine site results in an irregular potential landscape with a distribution of local energy barriers. Obviously, such a distribution facilitates F anion hopping since higher conductivities are reported for the mixed compounds as compared to Sr-free BaLiF<sub>3</sub>.<sup>51</sup> In addition to local strain throughout the bulk structure, disordered regions may be found near the interfacial regions in nanocrystalline Ba<sub>1-x</sub>Sr<sub>x</sub>LiF<sub>3</sub>. While the interior of the nanocrystallites reveal an ordered structure, the surface regions are affected by dislocations, as it is shown by the TEM images in Figure 8.<sup>51</sup>

### Fluorides Crystallizing with Cubic Symmetry: (Ba,Ca)F<sub>2</sub>

BaF<sub>2</sub> and CaF<sub>2</sub> do not form a solid solution by high temperature synthesis routes. This observation is due to the large difference in ionic radii of Ba<sup>2+</sup> (1.42 Å) and Ca<sup>2+</sup> (1.12 Å). The formation of Ba<sub>*x*</sub>Ca<sub>1-x</sub>F<sub>2</sub>, however, can be forced by treating the fluorides in a high-energy planetary ball mill (see Figure 9).<sup>47, 53</sup> Isovalent mixing yields a metastable ternary fluoride with cubic symmetry (Figure 10 a)) whose ionic conductivity is by about two orders of magnitude higher than that of nanocrystalline, pure BaF<sub>2</sub>.<sup>52</sup> Ion conductivity values derived from impedance spectroscopy are in the order of 1.16 × 10<sup>5</sup> S/cm at 413 K, see also Figure 10 that shows the variation of conductivity with *x*.

If a mixture of BaF<sub>2</sub> and CaF<sub>2</sub> is milled sufficiently long in high-energy ball mills, the XRPD unequivocally reveals the formation of a (Ba,Ca)F<sub>2</sub> solid solution.<sup>52</sup> This results in complex <sup>19</sup>F MAS NMR spectra being composed of several NMR lines associated with the [Ba]<sub>*a*</sub>[Ca]<sub>*b*</sub> environments formed (see Figure 10 c)). Differential scanning calorimetry measurements showed that the compound prepared is stable up to ca. 680 K.<sup>53</sup> In contrast, lanthanum fluoride forms a stable solution with BaF<sub>2</sub>. As an example, ionic conductivity in Ba<sub>0.5</sub>Ca<sub>0.3</sub>La<sub>0.2</sub>F<sub>2.2</sub>, which was prepared under almost the same turns out to be very similar compared to Ba<sub>0.5</sub>Ca<sub>0.5</sub>F<sub>2</sub>. In both cases CaF<sub>2</sub> starts to segregate at high temper-

atures causing the conductivity to drop off. Interestingly, XRPD gave no indications for any  $\text{LaF}_3$  that was precipitated at higher  $T$ . Thus, the lower conductivity is attributed to crystallite growth, structural relaxation processes including the ‘healing’ of defects.

#### Fluorides with Tysonite Structure: $\text{Ba}_{1-x}\text{La}_x\text{F}_{2+x}$

$\text{BaF}_2$  and  $\text{LaF}_3$  are miscible in almost any molar ratio and form stable solutions up to high temperatures which enables thermal as well as mechanochemical syntheses routes. The benefit of mechanochemistry, however, is the creation of defects necessary to yield higher conductivities compared to the highly ordered, crystalline counterparts.  $\text{Ba}_{0.6}\text{La}_{0.4}\text{F}_{2.4}$ , which shows the highest conductivity among the  $\text{Ba}_{1-x}\text{La}_x\text{F}_{2+x}$  solid solutions,<sup>23</sup> was chosen as a model substance to study ion dynamics by both NMR (see Figure 11) and impedance spectroscopy (Figure 12).<sup>49</sup>

Mechanosynthesized  $\text{Ba}_{0.6}\text{La}_{0.4}\text{F}_{2.4}$  is characterized by broad XRPD reflections pointing to structural disorder and strain introduced during its preparation.<sup>23, 49</sup> Static  $^{19}\text{F}$  NMR line shapes support this finding; besides dipolar broadening the lines recorded can be understood as a superposition of many lines representing the variety of magnetically distinct F environments. Variable-temperature NMR measurements, including line shape studies and relaxation measurements, as well as conductivity measurements reveal complex ion dynamics. Depending on the time scale the NMR method applied is sensitive to, activation energies obtained

range from 0.16 eV to 0.44 eV. In particular, the presence of several hopping processes is highlighted in the Arrhenius diagram of Figure 11 that summarizes NMR relaxometry data on mechano-synthesized  $\text{Ba}_{0.6}\text{La}_{0.4}\text{F}_{2.4}$ . While with  $T_1$  NMR measurements only the low- $T$  flank of the diffusion-induced rate peak is accessible, the analogous rate  $1/T_{1\rho}$  passes through a maximum; the corresponding peak is, however, unusually broad on the  $1/T$  axis. It directly reflects a wide distribution of ion jump processes occurring on a very similar time-scale. Compared to DC conductivity measurements, NMR relaxometry is a probe to uncover local jump processes, *i.e.*, it is possible to reveal the low energy barriers of an irregularly shaped potential landscape the ions have to surmount.

For comparison, conductivity spectroscopy, if DC plateau values were considered, points to a mean activation energy of 0.57 eV (Figure 12) being a typical value found for migration processes that are mainly driven by anion vacancies.<sup>55</sup> On the other hand, analysing AC conductivities recorded at frequencies similar to the NMR Larmor frequency yield activation energies being in agreement with those extracted from NMR (Figure 12 b)). At high frequencies  $\sigma'$  is sensitive to local (forward-backward) jumps, *i.e.*, both methods are able to access dynamic parameters on the same time scale. This similarity is also valid in the regime of very low  $T$ : the responses of the two spectroscopic techniques indicate the presence of strictly localized, within-site motions. The latter observation points

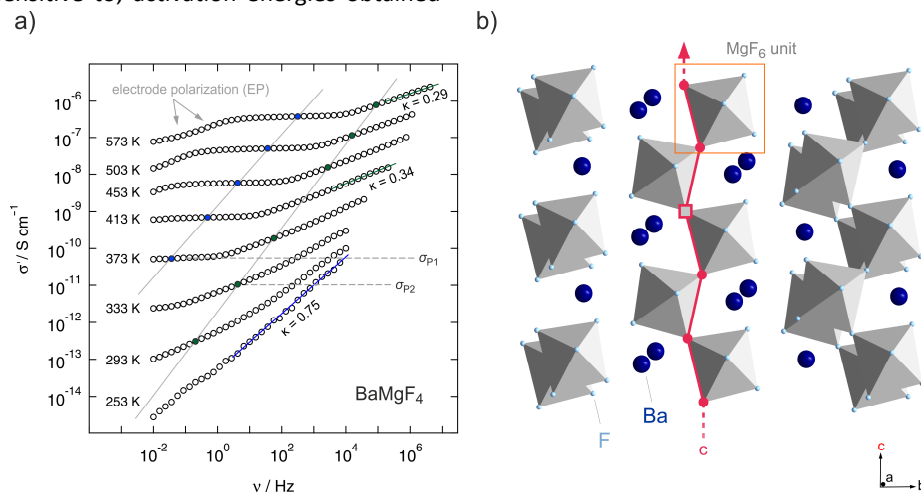


**Fig. 13:** a) Conductivity isotherms of mechano-synthesized  $\text{BaMgF}_4$  in a one-pot route. The slope of the isotherms at higher temperatures was close to 0.3 which is associated with low dimensional (1D) transport. b) Crystal structure of  $\text{BaMgF}_4$ : the corner sharing  $\text{MgF}_6$ -octahedra form a diffusion pathway along the  $c$ -axis. Kannan *et al.* investigated oriented single crystals and reported on the highest conductivity along the  $c$ -axis. Figures taken from Ref. 28.

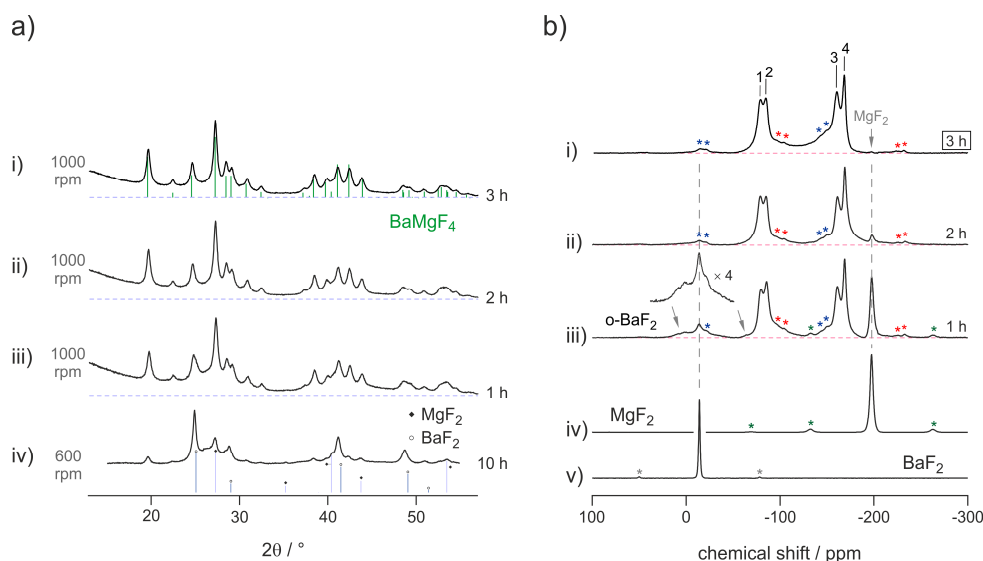


**Fig. 14:** Comparison of the information obtained from a) X-ray powder diffraction and b) <sup>19</sup>F solid state MAS NMR. The residual starting materials cannot be identified by XRPD (a) but were identified by MAS NMR. The latter one was used to follow the synthesis procedure, which was finished after three hours, as no noteworthy amounts of pure BaF<sub>2</sub> or MgF<sub>2</sub> could be identified any longer. Figures taken from Ref. 28.

to a highly irregular distribution of energy barriers in mechanosynthesized Ba<sub>0.6</sub>La<sub>0.4</sub>F<sub>2.4</sub>.<sup>49</sup>

#### Channel-Structured Fluorides: BaMgF<sub>4</sub>

Besides the formation of structurally disordered solid solutions taking advantage of aliovalent and isovalent ion mixing, mechanosynthesis can be used to prepare functional materials with remarkable purity. BaMgF<sub>4</sub>, which is a channel-structured ternary fluoride, is accessible via mechanical treatment under extremely harsh conditions, *i.e.*, at very high rotation speeds.<sup>28</sup> Ion transport is influenced by the spatial confined of the crystal structure. BaMgF<sub>4</sub> crystallizes in the orthorhombic *Cmc*2<sub>1</sub> structure and consists of strands of corner-sharing MgF<sub>6</sub>-octahedra that are separated by Ba-ions. These MgF<sub>6</sub>-octahedra run in parallel with the *c*-axis of the unit cell and provide a 1-dimensional pathway which is preferred for the conduction of F-ions (see Figure 13).<sup>56</sup>

The material, which usually requires high temperaturesto be synthesized from a mixture of BaF<sub>2</sub> and MgF<sub>2</sub>,<sup>56</sup> could be prepared in a planetary ball mill at rotation speeds as high as 1000 rpm.<sup>28</sup> At lower rotation speeds the synthesis remains unsuccessful. We attribute this finding to the strong heat development at the contact region of the milling media (balls/beaker walls) that induces the solid state reaction finally yielding BaMgF<sub>4</sub> as the only phase.

The synthesis was followed by XRPD and <sup>19</sup>F MAS NMR spectroscopy which is presented in Figure 14.<sup>28</sup> Switching off the mill after immediately interrupts the synthesis process; hence, the evolution of the product can directly be followed as a function of milling time. Interestingly, whereas the XRPD patterns recorded only show reflections of the product formed, <sup>19</sup>F MAS NMR reveals a high amount of the starting materials, MgF<sub>2</sub> and BaF<sub>2</sub>, still being present. Again, this demonstrates the benefits if both methods are used in combination. The increase of the signal intensity in the X-ray powder pattern at low diffraction angles points to amorphous material that could be attributed to MgF<sub>2</sub>. Indeed, non-reacted MgF<sub>2</sub> is clearly visible in the corresponding <sup>19</sup>F MAS NMR spectrum, but is missing or superimposed by the signals of the product in X-ray diffraction. The signal of BaF<sub>2</sub> is also likely to be hidden under the broad XRPD reflections of the product. After milling the mixture for three hours the <sup>19</sup>F MAS NMR lines attributed to the starting materials completely vanished; according to NMR, at this stage the reaction is completed.

As expected, the MAS NMR spectra show four different lines each representing one of the magnetically non-equivalent F sites in BaMgF<sub>4</sub>. The lines partly overlap as a result from local disorder introduced during milling. For comparison, thermochemical approaches or post annealing of the product yields well separated signals due to grain growth and healing of defects.<sup>57</sup>

Worth noting, conductivity spectroscopy indeed indicates a quasi-1-dimensional migration pathway the ions chose to jump over long distances.<sup>28</sup> In general, low-dimensional ion transport influences the power law exponent  $\kappa$  describing the dispersive region of the conductivity *isotherms* (see Figure 4). In the present case, the low  $\kappa$  values of approximately 0.3 (see the isotherms shown in Figure 13 a)) indeed point to F anion migration along the aligned corner-sharing  $\text{MgF}_6$  units. This finding is in agreement with the results of Kannan *et al.* who investigated  $\text{BaMgF}_4$  single crystals.<sup>56</sup>

### Two-Dimensional Ion Conduction: Layer-structured $\text{BaSnF}_4$

Besides using mechanochemistry to prepare defect-rich materials, it is also a valuable tool to mechanically activate the reactants: the final product is only obtained after a subsequent annealing step. If heat treatment is carried out in a moderate way, defects may be frozen, *i.e.*, partly preserved. The residual defects are anticipated to greatly govern ion transport even in the annealed samples characterized by larger grains. Tetragonal, layer-structured  $\text{BaSnF}_4$  represents such an example.

$\text{BaSnF}_4$  is one of the fastest F anion conducting materials known today.<sup>37</sup> Similar to  $\text{BaMgF}_4$ , it shows anisotropic conduction characteristics. This behaviour is related to the alternating double-layer structure of  $\text{BaSnF}_4$  yielding three different types of interlayers built up of either Ba-Ba, Ba-Sn, or Sn-Sn cations. The F anions are distributed between these cation layers with each showing different diffusion characteristics depending on the surrounding cations. Because of the highly ordered environment one can distinguish between fluorine ions located close to Sn-ions or close to Ba-ions. At room temperature, two spin reservoirs were found by  $^{19}\text{F}$  MAS NMR spectroscopy, see the work by Grey and co-workers.<sup>38</sup> The anions which are distributed in the more rigid Ba-Ba interlayer do not exchange very much with those in the neighbouring Ba-Sn layer; the ions residing in the Ba-Sn layer are the most mobile ones. As was shown for  $\text{PbSnF}_4$  compounds,<sup>58</sup> the occupation of fluorine ions in the Sn-Sn layer is rather low. This observation can be explained by the steric demand of the lone-pairs of the Sn ions.<sup>58</sup> Similar anisotropic properties, which will largely affect ion dynamics, are also expected for  $\text{BaSnF}_4$ .

Considering ionic conductivity, the values for mechanochemically synthesized  $\text{BaSnF}_4$  are the

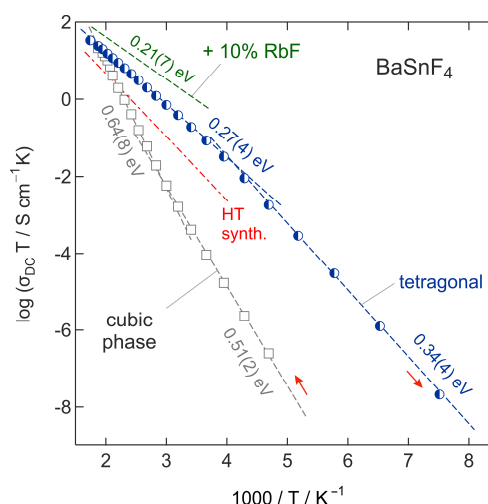


**Fig. 15:** Arrhenius diagram of the ionic conductivity of  $\text{BaSnF}_4$  samples. The mechanochemical synthesis yield a metastable, cubic modification that starts to transform into the highly conductive tetragonal form at 483 K which can be seen by the inflection of the data points (grey empty cubes). The nanocrystalline tetragonal modification shows the highest conductivity of  $\text{BaSnF}_4$ , reported in the literature so far. The red, dotted line corresponds to the same material synthesized by high temperature methods. The conductivity of the material can be further increased by

highest reported in the literature so far.<sup>45</sup> In contrast to other preparation methods reported, even after the annealing step at 573 K the average crystallite size of  $\text{BaSnF}_4$  remains small, namely  $< 25$  nm according to the equation introduced by Scherrer. This fact might explain the high conductivity found, most likely remaining defects and large interfacial areas substantially govern F ion dynamics.

To investigate possible effects of  $\text{Ba}^{2+}$ -substitution on the conduction behaviour, 10% of the  $\text{BaF}_2$  was replaced with  $\text{RbF}$ . The comparable ionic radius of  $\text{Rb}^+$  was expected to be rather compatible with the  $\text{Ba}^{2+}$ -environment than the smaller  $\text{Sn}^{2+}$ . The replacement of bivalent  $\text{Ba}^{2+}$  with monovalent  $\text{Rb}^+$  is expected to introduce vacancies and thus to enhance the dynamics of the rigid  $\text{BaF}_2$ -derived sub-layer. Indeed, the total conductivity could be increased by about 10% reaching 3 mS/cm at room temperature, as it is illustrated in Figure 15. This value is one of the highest ever reported for  $\text{BaSnF}_4$ .

### Summary

This review represents a brief overview about the local structures and ion dynamics in defect-rich fluorides recently prepared via mechanochemically routes. Without doubt mechanochemistry, in some cases combined with soft annealing steps, is as a

powerful synthesis method that enables a facile preparation of complex fluorides, as well as oxides and sulphides that could serve as fast ion conducting materials. In particular, it allows a direct preparation of nanocrystalline powders that can be processed in a straightforward way, *i.e.*, without the need of further purification steps. In many cases, due to structural disorder or non-equilibrium effects, the compounds synthesized benefit from improved ion transport properties if compared to conventionally prepared solids. Furthermore, as no high temperatures are needed, metastable compounds can be synthesized that are not accessible by other synthesis routes.

Considering fluorine-bearing compounds  $^{19}\text{F}$  solid-state MAS NMR, carried out at extremely fast spinning speeds, has been demonstrated as a versatile method to reveal local magnetic structures and hence to shed light on the evolution of the final compounds with increasing milling time.

In contrast to X-ray diffraction methods, MAS NMR is not only sensitive to crystalline materials, it is also possible to obtain information about amorphous fractions. In particular, due to the excellent receptivity of the  $^{19}\text{F}$  nucleus, fluorides represent highly suitable model compounds to study mechanochemical reactions.

The use of solid state NMR spectroscopy is, however, not limited to explore structural details of disordered solids, but also to investigate ion dynamics. In combination with impedance measurements and conductivity investigations the various spin-relaxation methods can be used to study short- as well as long range  $^{19}\text{F}$  ion transport. Via the application of both methods the information obtainable range from elementary jump processes to long-range (through-going) ion dynamics and contain activation energies, jump rates and diffusion coefficients, respectively. In addition, the data retrieved from NMR relaxometry can also provide information on possible spin reservoirs differing in ion dynamics. This means that in favourable cases a separation of dynamically distinct ions in the bulk and grain boundary regions is possible.

To conclude, a thorough understanding of formation mechanisms as well as properties of (nano-)crystalline compounds prepared via mechanochemical may open the field for future work including preparation of new fluorides as well as their application in modern energy storage systems, in particular.

## Acknowledgements

The present work is financially supported by the DFG within the framework of the Priority Program 'Crystalline Non-Equilibrium Phases' (SPP 1415).

## References

1. S. L. James, C. J. Adams, C. Bolm, D. Braga, P. Collier, T. Friscic, F. Grepioni, K. D. Harris, G. Hyett, W. Jones, A. Krebs, J. Mack, L. Maini, A. G. Orpen, I. P. Parkin, W. C. Shearouse, J. W. Steed and D. C. Waddell, *Chem. Soc. Rev.*, 2012, **41**, 413-447.
2. V. Šepelák, A. Düvel, M. Wilkening, K. D. Becker and P. Heitjans, *Chem. Soc. Rev.*, 2013, **42**, 7507-7520.
3. P. Balaz, M. Achimovicova, M. Balaz, P. Billik, Z. Cherkezova-Zheleva, J. M. Criado, F. Delogu, E. Dutkova, E. Gaffet, F. J. Gotor, R. Kumar, I. Mitov, T. Rojac, M. Senna, A. Streletskii and K. Wieczorek-Ciurawa, *Chem. Soc. Rev.*, 2013, **42**, 7571-7637.
4. R. A. Shakoob, S. Y. Lim, H. Kim, K.-W. Nam, J. K. Kang, K. Kang and J. W. Choi, *Solid State Ion.*, 2012, **218**, 35-40.
5. P. Liao, J. Li and J. R. Dahn, *J. Electrochem. Soc.*, 2010, **157**, A355-A361.
6. K. Minami, A. Hayashi and M. Tatsumisago, *J. Am. Ceram. Soc.*, 2011, **94**, 1779-1783.
7. D. Wohlmuth, V. Epp and M. Wilkening, *Chem. Phys. Chem.*, 2015, **16**, 2582-2593.
8. W. Jones and M. D. Eddleston, *Faraday Discuss.*, 2014, **170**, 9-34.
9. L. Takacs, *J. Mater. Sci.*, 2004, **39**, 4987-4993.
10. C. R. Hickenboth, J. S. Moore, S. R. White, N. R. Sottos, J. Baudry and S. R. Wilson, *Nature*, 2007, **446**, 423-427.
11. U. Hoffmann, C. Horst and U. Kunz, in *Integrated Chemical Processes*, eds. K. Sundmacher, A. Kienle and A. Seidel-Margenstern, Wiley, Weinheim, 2005, ch. 14, p. 409.
12. A. Chadwick and S. Savin, *Solid State Ion.*, 2006, **177**, 3001-3008.
13. P. Heitjans and M. Wilkening, *Mater. Res. Bull.*, 2009, **34**, 915-922.
14. P. Heitjans and S. Indris, *J. Phys.: Condens. Matter*, 2003, **15**, R1257-R1289.
15. S. Indris and P. Heitjans, *J. Non-Cryst. Solids*, 2002, **307**, 555-564.
16. M. Wilkening, S. Indris and P. Heitjans, *Phys. Chem. Chem. Phys.*, 2003, **5**, 2225-2231.
17. C. C. Liang, *J. Electrochem. Soc.*, 1973, **120**, 1289-1292.
18. N. Sata, K. Eberman, K. Eberl and J. Maier, *Nature*, 2000, **408**, 946-949.
19. J. Maier, *J. Phys. Chem. Solids*, 1985, **46**, 309-320.

20. J. Maier, *Prog. Solid State Chem.*, 1995, **23**, 171-263.
21. J. Maier, *Phys. Chem. Chem. Phys.*, 2009, **11**, 3011-3022.
22. J. Maier, *Nat. Mater.*, 2005, **4**, 805-815.
23. A. Düvel, J. Bednarcik, V. Šepelák and P. Heitjans, *J. Phys. Chem. C*, 2014, **118**, 7117-7129.
24. F. P. Bowden and D. Tabor, *The Friction and Lubrication of Solids*, Clarendon Press, Oxford, 1958.
25. F. P. Bowden and A. Yoffe, *Initiation and Growth of Explosion in Liquids and Solids*, Cambridge University Press, Cambridge, 1952.
26. F. P. Bowden and A. Yoffe, *Fast Reactions in Solids*, Butterworths, London, 1958.
27. P. A. Thiessen, M. K. and G. Heinicke, *Grundlagen der Tribochemie*, Akademie-Verlag Berlin, 1967.
28. F. Preishuber-Pflügl and M. Wilkening, *Dalton Trans.*, 2014, **43**, 9901-9908.
29. M. Wilkening and P. Heitjans, *Chem. Phys. Chem.*, 2012, **13**, 53-65.
30. A. Kuhn, M. Kunze, P. Sreeraj, H. D. Wiemhöfer, V. Thangadurai, M. Wilkening and P. Heitjans, *Solid State Nucl. Magn. Reson.*, 2012, **42**, 2-8.
31. A. Kuhn, S. Narayanan, L. Spencer, G. Goward, V. Thangadurai and M. Wilkening, *Phys. Rev. B*, 2011, **83**, 094302
32. V. Epp and M. Wilkening, *Phys. Rev. B*, 2010, **82**, 020301.
33. A. Kuhn, P. Sreeraj, R. Pöttgen, H. D. Wiemhöfer, M. Wilkening and P. Heitjans, *J. Am. Chem. Soc.*, 2011, **133**, 11018-11021.
34. J. Schoonman, *J. Electrochem. Soc.*, 1976, **123**, 1772-1775.
35. M. Anji Reddy and M. Fichtner, *J. Mater. Chem.*, 2011, **21**, 17059-17062.
36. A. V. Chadwick, E.-S. Hammam, D. van der Putten and J. H. Strange, *Cryst. Latt. Def. and Amorph. Mat.*, 1987, **15**, 303-308.
37. L. N. Patro and K. Hariharan, *Solid State Ion.*, 2013, **239**, 41-49.
38. S. Chaudhuri, F. Wang and C. P. Grey, *J. Am. Chem. Soc.*, 2002, **124**, 11746-11757.
39. G. Dénès, T. Tyliszczak and P. Hitchcock, *J. Solid State Chem.*, 1991, **91**, 1-15.
40. G. Dénès, T. Birchall, M. Sayer and M. F. Bell, *Solid State Ion.*, 1984, **13**, 213-219.
41. G. Dénès, J. Hantash, A. Muntasar, P. Oldfield and A. Bartlett, *Hyperfine Interact.*, 2007, **170**, 145-158.
42. L. N. Patro and K. Hariharan, *Mater. Res. Bull.*, 2011, **46**, 732-737.
43. M. M. Ahmad and K. Yamada, *Appl. Phys. Lett.*, 2007, **91**, 052912.
44. M. M. Ahmad, Y. Yamane and K. Yamada, *J. Appl. Phys.*, 2009, **106**, 074106.
45. F. Preishuber-Pflügl, V. Epp, S. Nakhal, M. Lerch and M. Wilkening, *Phys. Status Sol. C*, 2015, **12**, 10-14.
46. L. N. Patro and K. Hariharan, *Mater. Lett.*, 2012, **80**, 26-28.
47. B. Ruprecht, M. Wilkening, S. Steuernagel and P. Heitjans, *J. Mater. Chem.*, 2008, **18**, 5412-5416.
48. C. Rongeat, M. A. Reddy, R. Witter and M. Fichtner, *J. Phys. Chem. C*, 2013, **117**, 4943-4950.
49. F. Preishuber-Pflügl, P. Bottke, V. Pregartner, B. Bitschnau and M. Wilkening, *Phys. Chem. Chem. Phys.*, 2014, **16**, 9580-9590.
50. H. Geiger, G. Schon and H. Stork, *Solid State Ionics*, 1985, **15**, 155-158.
51. A. Düvel, S. Wegner, K. Efimov, A. Feldhoff, P. Heitjans and M. Wilkening, *J. Mater. Chem.*, 2011, **21**, 6238-6250.
52. A. Düvel, B. Ruprecht, P. Heitjans and M. Wilkening, *J. Phys. Chem. C*, 2011, **115**, 23784-23789.
53. B. Ruprecht, M. Wilkening, A. Feldhoff, S. Steuernagel and P. Heitjans, *Phys. Chem. Chem. Phys.*, 2009, **11**, 3071-3081.
54. A. Düvel, M. Wilkening, R. Uecker, S. Wegner, V. Šepelák and P. Heitjans, *Phys. Chem. Chem. Phys.*, 2010, **12**, 11251-11262.
55. D. R. Figueroa, A. V. Chadwick and J. H. Strange, *Journal of Physics C: Solid State Physics*, 1977, **11**, 55-73.
56. C. V. Kannan, K. Shimamura, H. R. Zeng, H. Kimura, E. G. Villora and K. Kitamura, *J. Appl. Phys.*, 2008, **104**, 114113.
57. G. Scholz, S. Breitfeld, T. Krahl, A. Duvel, P. Heitjans and E. Kemnitz, *Solid State Sci*, 2015, **50**, 32-41.
58. R. Kanno, K. Ohno, H. Izumi, Y. Kawamoto, T. Kamiyama, H. Asano and F. Izumi, *Solid State Ion.*, 1994, **70**, 253-258.

## 6. Conclusion and Outlook

Within the framework of this doctoral thesis, various solid-state F-ion conductors were prepared and thoroughly analyzed in terms of their diffusion parameters, respectively their ionic conductivity. The synthesis was carried out by mechanochemical pathways using high energy planetary ball mills. New preparation routes based on the chemical conversions triggered by mechanochemistry were demonstrated for BaMgF<sub>4</sub> as well as solid solutions of BaF<sub>2</sub> and LaF<sub>3</sub>. In addition, it was shown that this preparation method enables the improvement of the diffusivity via a size reduction or the formation of defects (*cp.* coarse grained *vs* nanocrystalline BaF<sub>2</sub>).

Diffusion parameters were studied in detail by solid state NMR relaxation and broadband impedance spectroscopy. The powerful combination of these techniques does not only provide access to a large dynamic window, but also allows the comparison of the data found for the individual methods. In particular, such comparative studies are necessary for the elaboration of diffusion mechanisms for distinct materials.

Tetragonal BaSnF<sub>4</sub> was the most intensively studied material in this work. It was prepared by mechanochemical milling of the binary fluorides followed by an annealing step at moderate temperatures (573 K). The conductivity values found for the tetragonal modification are among the highest values that were reported for this material yet.<sup>10,70,71,80,82</sup> It could be further increased by monovalent doping with RbF to about 2 mS/cm at room temperature. Conductivities in the range of a few mS/cm are considered as necessary for all solid state batteries, *e.g.*, based on a fluoride ion chemistry.<sup>4</sup> Tetragonal BaSnF<sub>4</sub> is characterized by a layered structure that results from the sterically demanding electron lone pair of the Sn<sup>2+</sup>-ions. <sup>19</sup>F MAS NMR studies and structural investigation have shown a temperature dependent occupation of the distinct sublayers, which has a significant influence on the conductivity characteristics. In this study, a change in the absolute values for the activation energy was found for temperatures of about 245 K, which can be interpreted as a confirmation of the above stated findings.

Cubic BaSnF<sub>4</sub> was obtained as an intermediate product after milling. X-ray diffraction studies have determined similar cell parameters to cubic BaF<sub>2</sub>. However, first <sup>19</sup>F MAS NMR investigations have shown two distinct F-signals in the spectra. The first one could be attributed to the fluorides in the local environment of the Ba<sup>2+</sup>-cations. The second spin reservoir shows a similar chemical shift as it is known from spectra of pure SnF<sub>2</sub>. As there is no evidence of a second, minor phase in the XRPD pattern, this could point to an amorphous fraction of SnF<sub>2</sub> that is formed during milling. In addition, the DSC measurements of the cubic BaSnF<sub>4</sub> also show a second exothermic transition below the conversion to the tetragonal modification, which might reflect the crystallization of this amorphous parts. In general, SnF<sub>2</sub> exhibits several transition temperatures below its melting point (490 K) which complicates a certain assignment of this process. The findings for the cubic

BaSnF<sub>4</sub> described above were not discussed in this thesis and require more intensive investigations. An X-ray diffraction study at different stages of the milling procedure was already carried out. Further investigations by <sup>19</sup>F MAS NMR similar to the study of BaMgF<sub>4</sub> are intended. In addition, the doped samples should be analyzed towards their local structure to explore the role of the dopant concerning the improvement of the conductivity.

The diffusion characteristics of Ba<sub>0.6</sub>La<sub>0.4</sub>F<sub>2.4</sub> solid solutions were analyzed by <sup>19</sup>F NMR relaxation studies in conjunction with high-frequency broadband impedance spectroscopy. The results from both methods are in good agreement with each other and provide insights into the diffusivity of the F-ions in such a disordered system.  $T_{1\rho}$  measurements in the rotating frame of reference enabled the determination of a rate maximum in the accessible temperature range. The unusual broad peak reflects a distribution of migration processes that proceed on a similar time scale. The low-temperature flank of the  $T_{1\rho}$ -maximum exhibits a small activation energy for the ion transport. This could originate from the migration in defect rich local environments that results from the structural disorder of the cation mixing (*cp.* Figure 24) and the synthesis conditions. An analysis of the high-frequency impedance data shows similar values for measurement frequencies in the region of several MHz up to some GHz, which corresponds to the time scales of the NMR experiment. The long-range transport is characterized by higher activation energies that are deduced from the dc-conductivities. Unfortunately, these values could not be compared to NMR relaxation data, as the high-temperature flank of the relaxation rates was not accessible with the available measurement setup.

An interesting alternative to Ba<sub>0.6</sub>La<sub>0.4</sub>F<sub>2.4</sub> would be provided by a SrF<sub>2</sub>/LaF<sub>3</sub>-system. Some authors report even higher conductivities for such a mixed conductor if only small amounts of LaF<sub>3</sub> are substituted by SrF<sub>2</sub>.<sup>95,96</sup> In general, these systems benefit from a higher stability in comparison to, *e.g.*, a BaSnF<sub>4</sub>-solid electrolyte. Thus, an application in energy storage systems is more likely for such compounds.

The synthesis and the characterization of BaMgF<sub>4</sub> was less spectacular in terms of the magnitude of the ionic conductivity, as it shows poor values, but has revealed important information about the mechanochemical synthesis procedure. In addition, the anisotropic diffusion characteristics that were found for single crystals could be confirmed for the nanocrystalline powder. The <sup>19</sup>F MAS NMR spectra gave insights to the proceeding reaction that could not be provided by X-ray spectroscopy. These findings can be applied to other mechanochemical reactions as mentioned above, such as the investigation of the structural transformations of the BaF<sub>2</sub>/SnF<sub>2</sub>-system during the milling procedure.

## A. Experimental

### General approach

Chemicals were purchased from standard suppliers and used as received without any further purification steps. It should be mentioned that each sample should be investigated by XRPD and optionally by MAS NMR to avoid the use of contaminated starting materials or compounds that are chemically completely different to what is indicated on the sample flask.

To avoid reactions with oxygen or moisture during the preparations or the measurements, starting materials and samples were dried *in vacuo* for 24 hours in a Büchi vacuum oven prior to use and subsequently transferred to an argon filled glovebox (MBraun). The synthesized powders and pressed pellets were kept in a separate container inside the glovebox to avoid cross contamination with other samples stored in the box.

Pellets for impedance spectroscopy were pressed in pressing tools of 5, 8 or 10 millimeters in diameter. For the 10 mm tool, a force of 10 kN was applied, which is equivalent to about 0.13 GPa. Higher pressures usually did not yield proper pellets, as the high amount of strain inside the pellet led to a burst during the removal from the pressing tool.

For the NMR relaxation measurements, powders were sealed under vacuum in small glass tubes of 5 mm in diameter and about 5 cm in length. This protects the samples from oxidation at high temperatures during the measurements.

### Mechanochemical preparation

Samples were prepared by mechanochemical milling in a Fritsch Pulverisette 7 premium line high energy ball mill. The milling tools, consisting of 50 mL beakers and 180 pieces of 5 mm balls per beaker, were made of stabilized zirconium dioxide. Usually, samples were prepared at a rotation speed of 600 rounds per (rpm) minute or higher, depending on the desired products. Special preparation techniques are described in the respective publications. After milling, the powders were removed from the beakers with ceramic tools to avoid a contamination with metals from spatulas, etc. The received coarse grained powders were crushed in an agate mortar to receive a fine powder for the preparation of the pellets. For cleaning of the milling equipment, the beakers were filled with 5 mg of quartz sand and 10 mL of water and treated in the mill for six cycles à 5 min in reverse mode at 600 rpm to remove the residual product from the balls and the beaker walls. The ceramic tools for the removal of the powder were immersed in HCl (1:1 with water) over night to dissolve the remaining product and subsequently heated to 1270 K to remove any residual contamination.

### **X-ray diffraction**

Powder diffraction patterns were recorded on a Bruker D8 Advance diffractometer with Bragg Brentano geometry using Cu K $\alpha$  radiation (10–100° 2 $\theta$ , step size 0.02° 2 $\theta$ , step time 1 s) at room temperature under air. Rietveld refinement was carried out with X-PertHighScorePlus (PANalytical).

### **Differential scanning calorimetry**

DSC measurements of the prepared powders were performed with a Netzsch STA 409 differential scanning calorimeter coupled with a QMS 403C mass spectrometer. The sample was heated under a constant helium gas flow in platinum crucibles at a rate of 10 K/min; starting from 293 K measurements were carried out up to 1000 K.

### **Impedance spectroscopy**

Broadband dielectric measurements were carried out on a Novocontrol Concept 80 Impedance Spectrometer. The setup consists of an Alpha-AN broadband analyzer that allows measurements from 10<sup>-4</sup> Hz to 10 MHz with an active ZGS-cell and an Agilent high frequency analyzer with a frequency range from 1 MHz up to 3 GHz including a special cell for high frequencies. Both cells are operated in a cryostat designed for temperatures ranging from 113 K to 673 K. The temperature is automatically controlled by Novocontrol's QUATRO cryosystem that evaporates liquid nitrogen which is heated in a gas jet that is located prior to the cryostat. High temperature measurements up to 1600 K are possible with a NorECs high temperature cell in a HT oven that is controlled by the Novotherm-HT System. The cell must be flushed with gas during the measurements that can either be nitrogen, argon, air or other, inflammable gases.

Before the start of a measurement, the samples can be flushed with dry nitrogen and optionally be heated, again to remove residual oxygen or moisture from the cell. Metastable compounds such as cubic BaSnF<sub>4</sub> were not heated in order to avoid initial structural changes. A usual measurement consisted of a heating run from 123 K to 573 K and back to 123 K in steps of 20 K using a frequency range from 10<sup>-2</sup> Hz to 10 MHz. Additional cycles can be carried out to investigate a change of the ionic conductivity upon heating, which is often observed for nanocrystalline materials.

### **NMR setup**

Nuclear Magnetic resonance experiments were carried out on Bruker Avance III spectrometers. For the relaxation measurements, an Avance III 300 spectrometer operating at 7 Tesla was employed. This field corresponds to a <sup>19</sup>F Larmor frequency of

---

$\omega_0/2\pi = 282$  MHz. The custom  $^{19}\text{F}$  Probe (NMR-Service, Germany) can record spectra under static conditions in a temperature range from 130 K up to 280 K. The temperature was controlled by a Eurotherm controller with a thermocouple of type T.

Spin-lattice relaxation (SLR) rates ( $1/T_1$ ) were acquired with the saturation recovery pulse sequence  $10 \times \pi/2 - t_d - \pi/2 - \text{acquisition (acq.)}$ . This sequence initially destroys any longitudinal magnetization  $M_z$  using ten  $\pi/2$  pulses separated by 40  $\mu\text{s}$  and subsequently measures its recovery as a function of the delay time  $t_d$ . Relaxation rates  $1/T_{1\rho}$  in the rotating frame of reference (SLR $_{\rho}$ ) were recorded with the spin-lock technique,  $\pi/2 - \text{p}(t_{\text{lock}}) - \text{acq.}$   $1/T_{1(2)}$  and  $1/T_{1\rho}$  rates were obtained by parameterizing the magnetic transients  $M_z(t_d)$  and  $M_{\rho}(t_{\text{lock}})$ , by stretched exponentials:  $M_z(t_d) \propto 1 - \exp(-(t/T_1)^{\gamma})$  and  $M_{\rho}(t_{\text{lock}}) \propto \exp(-(t_{\text{lock}}/T_{1\rho})^{\gamma_{\rho}})$ .

$^{19}\text{F}$  NMR spin-spin relaxation (SSR) rates  $1/T_2$  were recorded by a (two-pulse) solid-echo pulse sequence:  $\pi/2 - t_{\text{echo}} - \pi/2 - \text{acq.}$   $t_{\text{echo}}$  denotes the variable interpulse delay. The transients obtained were fitted with stretched exponentials. Static  $^{19}\text{F}$  NMR spectra were either obtained after Fourier transformation (FT) of the free induction decay, which were recorded by non-selective irradiation with a single  $\pi/2$  pulse, or by FT of the solid echo beginning from the top of the signal.

$^{19}\text{F}$  MAS NMR spectra were recorded on a Bruker Avance III 500 spectrometer at 11 Tesla, *i.e.*, a Larmor frequency of  $\omega_0/2\pi = 470.4$  MHz. Two different MAS probes (Bruker) are available; one for 2.5 mm rotors with a spinning speed up to 30 kHz and one for 1.4 mm rotors for a spinning speed up to 60 kHz. Solid, crystalline LiF was used as a secondary standard with a chemical shift of -204.3 ppm (primary reference  $\text{CFCl}_3$ , 0 ppm).



## B. Bibliography

- 1 A. V. Chadwick, *Phys. Status Solidi*, 2007, **204**, 631–641.
- 2 M. Faraday, *Experimental Researches in Electricity*, R. and J. E. Taylor, London, 1940.
- 3 M. Faraday, *Faraday's Diaries 1820-1862*, G. Bell, London, 2<sup>nd</sup> edn., 1939.
- 4 M. Anji Reddy and M. Fichtner, *J. Mater. Chem.*, 2011, **21**, 17059–17062.
- 5 J. H. Kennedy and J. C. Hunter, *J. Electrochem. Soc.*, 1976, **123**, 10–14.
- 6 J. Schoonman, *J. Electrochem. Soc.*, 1976, **123**, 1772–1775.
- 7 J. Chable, B. Dieudonné, M. Body, C. Legein, M.-P. Crosnier-Lopez, C. Galven, F. Mauvy, E. Durand, S. Fourcade, D. Sheptyakov, M. Leblanc, V. Maisonneuve and A. Demourgues, *Dalt. Trans.*, 2015, **44**, 19625–19635.
- 8 B. Dieudonné, J. Chable, F. Mauvy, S. Fourcade, E. Durand, E. Lebraud, M. Leblanc, C. Legein, M. Body, V. Maisonneuve and A. Demourgues, *J. Phys. Chem. C*, 2015, **119**, 25170–25179.
- 9 C. Rongeat, M. Anji Reddy, R. Witter and M. Fichtner, *ACS Appl. Mater. Interfaces*, 2014, **6**, 2103–2110.
- 10 L. N. Patro and K. Hariharan, *Solid State Ionics*, 2013, **239**, 41–49.
- 11 P. Atkins and J. de Paula, *Atkins' Physical Chemistry*, Oxford University Press, 10<sup>th</sup> edn., 2014.
- 12 H. Mehrer, *Diffusion in Solids*, Springer Berlin Heidelberg, Berlin, Heidelberg, 2007, vol. 155.
- 13 G. E. Murch, *Diffusion Kinetics in Solids*, Wiley-VCH, 2001.
- 14 P. Heitjans and J. Kärger, *Diffusion in condensed matter*, 2005.
- 15 W. Kleber, H.-J. Bautsch, J. Bohm and D. Klimm, *Einführung in die Kristallographie*, Oldenburg Wissenschaftsverlag, München, 19<sup>th</sup> edn., 2010.
- 16 P. Heitjans and S. Indris, *J. Phys. Condens. Matter*, 2003, **15**, R1257–R1289.
- 17 V. F. Lvovich, *Impedance Spectroscopy*, John Wiley & Sons, Inc., Hoboken, NJ, USA, 2012.
- 18 F. Kremer and A. Schönhal, Eds., *Broadband Dielectric Spectroscopy*, Springer Berlin Heidelberg, Berlin, Heidelberg, 2003.
- 19 E. Barsoukov and J. R. Macdonald, Eds., *Impedance Spectroscopy: Theory, Experiment, and Applications*, John Wiley & Sons, Hoboken, NJ, USA, 2<sup>nd</sup> edn., 2005.

- 20 D. Sidebottom, *Rev. Mod. Phys.*, 2009, **81**, 999–1014.
- 21 P. Macedo, C. Moynihan and R. Bose, *Phys. Chem. Glas.*, 1972, **13**, 171–179.
- 22 A. K. Jonscher, *Nature*, 1977, **267**, 673–679.
- 23 C. Cramer, K. Funke, T. Saatkamp, D. Wilmer and M. D. Ingram, *Zeitschrift für Naturforsch. A*, 1995, **50**, 1–5.
- 24 J. T. S. Irvine, D. C. Sinclair and A. R. West, *Adv. Mater.*, 1990, **2**, 132–138.
- 25 J. Maier, *Festkörper – Fehler und Funktion*, Vieweg+Teubner Verlag, Wiesbaden, 2000.
- 26 M. H. Levitt, *Spin Dynamics: Basics of Nuclear Magnetic Resonance*, John Wiley & Sons, Inc., Hoboken, NJ, USA, 2nd edn., 2008.
- 27 J. Keeler, *Understanding NMR Spectroscopy*, John Wiley & Sons, Inc., Chichester, UK, 2<sup>nd</sup> edn., 2010.
- 28 F. Bloch, *Phys. Rev.*, 1946, **70**, 460–474.
- 29 F. Bloch, W. W. Hansen and M. Packard, *Phys. Rev.*, 1946, **70**, 474–485.
- 30 N. Bloembergen, E. M. Purcell and R. V. Pound, *Phys. Rev.*, 1948, **73**, 679–712.
- 31 E. Tobschall, doctoral thesis, University of Hannover, 1999.
- 32 M. Wilkening, diploma thesis, University of Hannover, 2001.
- 33 A. Abragam, *The Principles of Nuclear Magnetism*, Oxford University Press, Oxford, 1962.
- 34 V. Epp, doctoral thesis, Graz University of Technology, 2015.
- 35 P. M. Richards, *Solid State Commun.*, 1978, **25**, 1019–1021.
- 36 M. Meyer, P. Maass and A. Bunde, *Phys. Rev. Lett.*, 1993, **71**, 573–576.
- 37 M. J. Duer, *Introduction to Solid-State NMR Spectroscopy*, Blackwell Science Ltd., Malden, 2004.
- 38 P. Bottke, doctoral thesis, Graz University of Technology, 2015.
- 39 E. Riedel and H.-J. Meyer, *Allgemeine und Anorganische Chemie*, De Gruyter, 11<sup>th</sup> edn., 2013.
- 40 S. L. James, C. J. Adams, C. Bolm, D. Braga, P. Collier, T. Frišćić, F. Grepioni, K. D. M. Harris, G. Hyett, W. Jones, A. Krebs, J. Mack, L. Maini, a. G. Orpen, I. P. Parkin, W. C. Shearouse, J. W. Steed and D. C. Waddell, *Chem. Soc. Rev.*, 2012, **41**, 413–447.

- 
- 41 P. Baláž, M. Achimovičová, M. Baláž, P. Billik, Z. Cherkezova-Zheleva, J. M. Criado, F. Delogu, E. Dutková, E. Gaffet, F. J. Gotor, R. Kumar, I. Mitov, T. Rojac, M. Senna, A. Streletskii and K. Wieczorek-Ciurowa, *Chem. Soc. Rev.*, 2013, **42**, 7571–637.
- 42 V. Šepelák, A. Düvel, M. Wilkening, K.-D. Becker and P. Heitjans, *Chem. Soc. Rev.*, 2013, **42**, 7507–20.
- 43 U. Hoffmann, C. Horst and U. Kunz, in *Integrated Chemical Processes*, Wiley-VCH Verlag GmbH & Co. KGaA, Weinheim, FRG, 2005, 407–436.
- 44 C. Suryanarayana, *Prog. Mater. Sci.*, 2001, **46**, 1–184.
- 45 F. P. Bowden and D. Tabor, *The Friction and Lubrication of Solids*, Clarendon Press, Oxford, 1958.
- 46 F. P. Bowden and A. Yoffe, *Fast Reactions in Solids*, Butterworths, London, 1958.
- 47 F. P. Bowden and A. Yoffe, *Initiation and Growth of Explosion in Liquids and Solids*, Cambridge University Press, Cambridge, 1952.
- 48 P. A. Thiessen, K. Meyer and G. Heinicke, *Grundlagen der Tribochemie*, Akademie-Verlag, Berlin, 1967.
- 49 P. Baláž, *Mechanochemistry in Nanoscience and Minerals Engineering*, Springer Berlin Heidelberg, Berlin, Heidelberg, 2008.
- 50 H. Brandstätter, D. Wohlmuth, P. Bottke, V. Pregartner and M. Wilkening, *Z. Phys. Chem.*, 2015, **229**, 1–12.
- 51 D. Wohlmuth, V. Epp, P. Bottke, I. Hanzu, B. Bitschnau, I. Letofsky-Papst, M. Kriechbaum, H. Amenitsch, F. Hofer and M. Wilkening, *J. Mater. Chem. A*, 2014, **2**, 20295–20306.
- 52 A. V. Chadwick, A. Düvel, P. Heitjans, D. M. Pickup, S. Ramos, D. C. Sayle and T. X. T. Sayle, *IOP Conf. Ser. Mater. Sci. Eng.*, 2015, **80**, 012005.
- 53 F. Preishuber-Pflügl, V. Epp, S. Nakhal, M. Lerch and M. Wilkening, *Phys. Status Solidi C*, 2015, **12**, 10–14.
- 54 Y. Yamane, K. Yamada and K. Inoue, *Solid State Ionics*, 2008, **179**, 605–610.
- 55 A. Düvel, S. Wegner, K. Efimov, A. Feldhoff, P. Heitjans and M. Wilkening, *J. Mater. Chem.*, 2011, **21**, 6238–6250.
- 56 A. V. Chadwick and S. L. P. Savin, *Solid State Ionics*, 2006, **177**, 3001–3008.
- 57 J. Jamnik and J. Maier, *Phys. Chem. Chem. Phys.*, 2003, **5**, 5215–5220.
- 58 Y.-G. Guo, J.-S. Hu and L.-J. Wan, *Adv. Mater.*, 2008, **20**, 2878–2887.
- 59 R. Malik, D. Burch, M. Bazant and G. Ceder, *Nano Lett.*, 2010, **10**, 4123–4127.

- 60 L. Ji, Z. Lin, M. Alcoutlabi and X. Zhang, *Energy Environ. Sci.*, 2011, **4**, 2682–2699.
- 61 C. Liu, F. Li, L.-P. Ma and H.-M. Cheng, *Adv. Mater.*, 2010, **22**, E28–E62.
- 62 K. Peng, J. Jie, W. Zhang and S.-T. Lee, *Appl. Phys. Lett.*, 2008, **93**, 033105.
- 63 U. Kasavajjula, C. Wang and a. J. Appleby, *J. Power Sources*, 2007, **163**, 1003–1039.
- 64 M. Holzapfel, H. Buqa, L. J. Hardwick, M. Hahn, A. Würsig, W. Scheifele, P. Novák, R. Kötz, C. Veit and F.-M. Petrat, *Electrochim. Acta*, 2006, **52**, 973–978.
- 65 W. Puin, S. Rodewald, R. Ramlau, P. Heitjans and J. Maier, 2000, **131**, 159–164.
- 66 B. Ruprecht, M. Wilkening, S. Steuernagel and P. Heitjans, *J. Mater. Chem.*, 2008, **18**, 5412–5416.
- 67 X. X. Guo, N. Sata and J. Maier, *Electrochim. Acta*, 2004, **49**, 1091–1096.
- 68 N. Sata, N. Y. Jin-Phillipp, K. Eberl and J. Maier, *Solid State Ionics*, 2002, **155**, 497–502.
- 69 F. Preishuber-Pflügl and M. Wilkening, *Dalt. Trans.*, 2014, **43**, 9901–9908.
- 70 L. N. Patro and K. Hariharan, *Mater. Res. Bull.*, 2011, **46**, 732–737.
- 71 M. M. Ahmad, Y. Yamane and K. Yamada, *J. Appl. Phys.*, 2009, **106**, 074106.
- 72 L. N. Patro and K. Hariharan, *Mater. Lett.*, 2012, **80**, 26–28.
- 73 A. Düvel, M. Wilkening, R. Uecker, S. Wegner, V. Šepelák and P. Heitjans, *Phys. Chem. Chem. Phys.*, 2010, **12**, 11251–11262.
- 74 A. Düvel, J. Bednarcik, V. Šepelák and P. Heitjans, *J. Phys. Chem. C*, 2014, **118**, 7117–7129.
- 75 L. Zhang, M. Anji Reddy and M. Fichtner, *Solid State Ionics*, 2015, **272**, 39–44.
- 76 C. Rongeat, M. Anji Reddy, R. Witter and M. Fichtner, *ACS Appl. Mater. Interfaces*, 2014, **6**, 2103–2110.
- 77 M. M. Ahmad, Y. Yamane and K. Yamada, *Mater. Sci. Eng. B*, 2013, **178**, 965–970.
- 78 S. Chaudhuri, F. Wang and C. P. Grey, *J. Am. Chem. Soc.*, 2002, **124**, 11746–57.
- 79 G. Denes, Y. H. Yu, T. Tyliszczak and A. P. Hitchcock, *J. Solid State Chem.*, 1991, **91**, 1–15.
- 80 G. Dénès, T. Birchall, M. Sayer and M. Bell, *Solid State Ionics*, 1984, **13**, 213–219.
- 81 G. Dénès, J. Hantash, A. Muntasar, P. Oldfield and A. Bartlett, *Hyperfine Interact.*, 2007, **170**, 145–158.

- 
- 82 A. V Chadwick, E. S. Hammam, D. Van der Putten and S. J. H,  
*Cryst. Latt. Def. Amorph. Mat.*, 1987, **15**, 303–308.
- 83 A. Collin, G. Dénès, D. Le Roux, M. C. Madamba, J. M. Parris and A. Salaün,  
*Int. J. Inorg. Mater.*, 1999, **1**, 289–301.
- 84 J. H. Figueroa, D R, Chadwick, A V, Strange, 1978, **11**, 55–73.
- 85 D. R. Figueroa, J. J. Fontanella, M. C. Wintersgill, A. V Chadwick and C. G.  
Andeen, *J. Phys. C Solid State Phys.*, 1984, **17**, 4399–4411.
- 86 S. Hull, *Reports Prog. Phys.*, 2004, **67**, 1233–1314.
- 87 C. Rongeat, M. A. Reddy, R. Witter and M. Fichtner,  
*J. Phys. Chem. C*, 2013, **117**, 4943–4950.
- 88 Y. Ma, J. Chen, Y. Zheng and X. Chen, *Appl. Opt.*, 2012, **51**, 5432–5437.
- 89 E. G. Villora, P. Molina, S. Álvarez, J. V. García-Santizo, M. O. Ramírez,  
K. Shimamura and L. E. Bausá, *J. Appl. Phys.*, 2010, **107**, 033106.
- 90 E. G. Villora, K. Shimamura, K. Sumiya and H. Ishibashi,  
*Opt. Express*, 2009, **17**, 12362–12378.
- 91 K. Shimamura, E. G. Villora, H. Zeng, M. Nakamura, S. Takekawa  
and K. Kitamura, *Appl. Phys. Lett.*, 2006, **89**, 232911.
- 92 C. V. Kannan, K. Shimamura, H. R. Zeng, H. Kimura, E. G. Villora  
and K. Kitamura, *J. Appl. Phys.*, 2008, **104**, 114113.
- 93 D. L. Sidebottom, *Phys. Rev. Lett.*, 1999, **83**, 983–986.
- 94 G. Scholz, S. Breinfeld, T. Krahl, A. Düvel, P. Heitjans and E. Kemnitz,  
*Solid State Sci.*, 2015, **50**, 32–41.
- 95 P. Fedorov, T. Turkina, B. Sobolev, E. Mariani and M. Svantner,  
*Solid State Ionics*, 1982, **6**, 331–335.
- 96 H. Geiger, G. Schon and H. Stork, *Solid State Ionics*, 1985, **15**, 155–158.



## C. Publications

### C. 1. Publications in peer reviewed journals

#### **Separating bulk from grain boundary Li ion conductivity in the sol – gel prepared solid electrolyte $\text{Li}_{1.5}\text{Al}_{0.5}\text{Ti}_{1.5}(\text{PO}_4)_3$**

S. Breuer, D. Prutsch, Q. Ma, V. Epp, F. Preishuber-Pflügl, F. Tietz and M. Wilkening,  
*J. Mater. Chem. A*, 2015, **3**, 21343.  
doi: 10.1039/c5ta06379e

#### **Covalent incorporation of the surfactant into high internal phase emulsion templated polymeric foams**

S. Kovacic, F. Preishuber-Pflügl, D. Pahovnik, E. Žagar and C. Slugovc,  
*Chem. Commun.*, 2015, **51**, 7225.  
doi: 10.1039/C4CC09199J

#### **Defect-enhanced F ion conductivity in layer-structured nanocrystalline $\text{BaSnF}_4$ prepared by high-energy ball milling combined with soft annealing**

F. Preishuber-Pflügl, V. Epp, S. Nakhal, M. Lerch, and M. Wilkening,  
*Phys. Status Solidi C*, 2015, **12**, 10.  
doi: 10.1002/pssc.201400193

#### **Evidence of low dimensional ion transport in mechanosynthesized nanocrystalline $\text{BaMgF}_4$**

F. Preishuber-Pflügl and M. Wilkening,  
*Dalton Trans.*, 2014, **43**, 9901.  
doi: 10.1039/C4DT00904E

#### **Correlated fluorine diffusion and ionic conduction in the nanocrystalline $\text{F}^-$ solid electrolyte $\text{Ba}_{0.6}\text{La}_{0.4}\text{F}_{2.4}$ – $^{19}\text{F}$ $T_{1(\rho)}$ NMR relaxation vs. conductivity measurements**

F. Preishuber-Pflügl, P. Bottke, V. Pregartner, B. Bitschnau, and M. Wilkening,  
*Phys. Chem. Chem. Phys.*, 2014, **16**, 9580.  
doi: 10.1039/C4CP00422A

#### **Macroporous Polyolefin Membranes from Dicyclopentadiene High Internal Phase Emulsions: Preparation and Morphology Tuning**

S. Kovacic, F. Preishuber-Pflügl, C. Slugovc,  
*Macromol. Mater. Eng.*, 2014, **299**, 843.  
doi: 10.1002/mame.201300400

## C. 2. Oral Presentations

### **Low-dimensional Ion Transport in Mechanosynthesized, Nanocrystalline BaMgF<sub>4</sub>**

F. Preishuber-Pflügl and M. Wilkening, *VIII International Conference on Mechanochemistry and Mechanical Alloying*, 2014/06/22, Kraków (Poland).

## C. 3. Posters

### **Mechanochemistry of Fluorine Ion Conductors: Insights into Synthesis and Characterization by Impedance Spectroscopy and Solid State NMR Methods**

F. Preishuber-Pflügl and M. Wilkening, *European Conference on Solid State Chemistry (ECSSC)*, 2015/08/23, Vienna (Austria).

### **Solid Electrolytes Based on Fast Fluorine Ion Motions – <sup>19</sup>F T<sub>1ρ</sub> NMR Relaxation vs Conductivity Measurements of Mechanosynthesized Nanocrystalline Ba<sub>0.6</sub>La<sub>0.4</sub>F<sub>2.4</sub>**

F. Preishuber-Pflügl, P. Bottke, V. Pregartner, B. Bitschnau, and M. Wilkening, *226<sup>th</sup> Meeting of the Electrochemical Society*, 2014/10/05, Cancun (Mexico).

### **Defect-enhanced F ion conductivity in layer-structured BaSnF<sub>4</sub> prepared by high-energy ball milling combined with soft annealing**

F. Preishuber-Pflügl and M. Wilkening, *EMRS Spring Meeting*, 2014/05/25, Lille (France).

### **Conductivity of Mechanosynthesized Phase-Pure Cubic and Tetragonal BaSnF<sub>4</sub>**

F. Preishuber-Pflügl and M. Wilkening, *International Battery Association Meeting*, 2014/03/10, Barcelona (Spain).

### **Ion Conductivity of BaSnF<sub>4</sub> Studied by Broadband Impedance Spectroscopy**

Preishuber-Pflügl, F.; Düvel, A.; Epp, V.; Wilkening, M., *ZFM Summer School 'Functional Solids*, 2012/07/22, Celle (Germany).

## D. Acknowledgment

The biggest thank you goes to Prof. Dr. Martin Wilkening for his great encouragement in the last four years. He was not only a great teacher in scientific questions but also a permanent supporter for all kinds of things. I would especially like to acknowledge for the scope for development and the support that I got to develop aside from scientific topics. I also highly appreciate that it was always possible to present my work on international conferences.

I am also grateful for the positive working atmosphere on the institute and especially in the AGW, our research group. Many thanks go to Dr. Viktor Epp for his instructions and the essential help with the impedance spectrometer and to Dr. Patrick Bottke for the introduction to the NMR spectrometer and the many fruitful discussions. I would also like to thank Liane Hochgatterer for her assistance and the rest of the group for the good time that we had together.

The collaboration with Dr. Brigitte Bitschnau and Prof. Dr. Franz Mautner regarding the X-ray diffraction measurements is also highly appreciated. I am also thankful for the DSC measurements that were carried out by Prof. Dr. Otto Fruhwirth and Dr. Theresa Kainz.

I also would like to thank all my friends for supporting me and for the fun and the relaxed time that I had if I was not just analyzing and interpreting data.

Most of all, I am indebted to my family for constantly supporting me ever since. I am most grateful to have such great parents and my sisters Julia and Verena that are always there for me. And at last, but certainly not least, I would like to thank you Nicole, for all your help, your patience, and your love to me.